LBL--29718

DE91 007741

Relativistic Heavy Ion Fragmentation at HISS

By

CRAIG EMERSON TULL
B.A. (Ohio Wesleyan University) 1981
M.A. (University of California, Davis) 1983

DISSERTATION

Submitted in partial satisfaction of the requirements for the degree of

DOCTOR OF PHILOSOPHY

in

Physics

in the

GRADUATE DIVISION

of the

UNIVERSITY OF CALIFORNIA

DAVIS

This work was supported by the Director, Office of Energy Research, Division of Nuclear Physics of the Office of High Energy and Nuclear Physics of the U.S. Department of Energy under Contract DE-AC03-76SF00098

I dedicate this thesis to my wife, Barbara, and to my parents and family.

Acknowledgements

I would like to thank the many people who helped with the preparation, execution, and analysis of this experiment.

Thanks to G. Peaslee and D. Morrissey for collaboration on the theoretical calculations, to the support and operations staff at the Bevatron for beam, to F. Bieser and I. Flores for technical help, to M. Bronson, C. McParland, and R. Wright for computer support, and to the Associated Western Universities for financial support.

I gratefully acknowledge assistance from and discussion with T. Kobayashi, M. Baumgartner, H. Crawford, W. Christie, P. Lindstrom, D. Olson, W. Müller, J. Romero, H. Wieman, and J. Young. Finally, I especially thank F.P. Brady and T.J.M Symons for their guidance and support.

Craig Emerson Tull
December 1989
Physics

Relativistic Heavy Ion Fragmentation at HISS

Abstract

An experiment was conducted at the Lawrence Berkeley Laboratory to measure projectile fragmentation of relativistic heavy ions.

Charge identification was obtained by the use of a Cerenkov Hodoscope operating above the threshold for total internal reflection, while velocity measurement was performed by use of a second set of Cerenkov radiators operating at the threshold for total internal reflection. Charge and mass resolution for the system was $\sigma_Z = 0.2$ e and $\sigma_A = 0.2$ u.

Measurements of the elemental and isotopic production cross sections for the fragmentation of ^{40}Ar at 1.65·A GeV have been compared with an Abrasion-Ablation Model based on the evaporation computer code GEMINI. The model proves to be an accurate predictor of the cross sections for fragments between Chlorine and Boron. The measured cross section were reproduced using simple geometry with charge dispersions induced by zero-point vibrations of the giant dipole resonance for the prompt abrasion stage, and injecting an excitation energy spectrum based on a final state interaction with scaling factor $E_{fsi} = 38.8$ MeV/c.

Measurement of the longitudinal momentum distribution widths for projectile fragments are consistent with previous experiment and can be interpreted as reflecting the Fermi momentum distribution in the initial projectile nucleus. Measurement of the transverse momentum indicate an additional, unexplained dependence of the reduced momentum widths on fragment mass. This dependence has the same sign and similar slope to previously measured fragments of ^{139}La, and to predictions based on phase-space constraints on the final state of the system.

1. Introduction

Experiment E772H is an inclusive measurement of projectile fragmentation using medium-heavy beams at the Heavy Ion Spectrometer System (HISS) at Lawrence Berkeley Laboratory's Bevalac. The experiment involved several beams (^{40}Ar, ^{56}Fe, and ^{91}Nb) at a lab energy of 1.65·A GeV and used for the first time new detector technology to allow measurements in this energy and mass region. Our experiment investigates two collision systems for each beam. One collision system for each beam was beam on carbon (A + C), while the second collision system was symmetric (A + A).

In this thesis, results are presented for the fragmentation of ^{40}Ar on targets of Carbon (C) and Potassium Cloride (KCl) at 1.65·A GeV in the lab and a method of measuring the velocity of relativistic heavy ions using the total internal reflection of Cerenkov radiation is described.

1.1. Accelerator

The Bevalac is located at the Lawrence Berkeley Laboratory (LBL) in Berkeley, California. The Bevalac is a combination of two separate particle accelerators at LBL; the Heavy Ion Linear ACcelerator (HILAC) and the Bevatron.

The Bevatron was built in 1952 as a proton synchrotron and was designed to accelerate protons of momentum up to 6.3 GeV/c (approximately the threshold necessary to create a proton-antiproton pair). In 1955, the antiproton was observed in an experiment by Chamberlain, Segre, Wiegand, and Ypsilantis[55Ch] at LBL, and the Bevatron went on to make many important contributions to the field of particle physics. In the early 1970's the Bevatron was upgraded to accelerate ions much heavier than the protons for which it was originally built with the intention of creating and observing nuclei at unusually high temperatures and densities.

The HILAC is a linear particle accelerator built to study heavy ion reactions at energies of up to ≈ 8·A MeV. The combination of the HILAC (as the source of heavy ions)

and the Bevatron (as the principle accelerator) gives experimenters at LBL access to ions up to Uranium (A = 238) at energies as high as 0.960·A GeV, and ions as heavy as Calcium (A = 40) up to energies as high as 2.1·A GeV.

1.2. Facility

The experimental facility we used at LBL is the Heavy Ion Spectrometer System (HISS). HISS was conceived as a workbench type facility[89En]. Instead of a fixed configuration of detectors designed for a single experiment, HISS consists of a number of moveable detectors, and a rotatable superconducting dipole magnet. This allows experimenters to configure a large range of different detector setups for a wide variety of experiments.

The heart of the HISS facility is a wide aperture (1 meter vertical gap) superconducting dipole magnet, capable of a maximum bending power of 7 Tesla-meters.

The detectors used in the experiment are discussed in detail in Chapter 2 but included upstream beam definition scintillators, upstream beam vectoring multi-wire proportional counters, an array of scintillators for measuring midrapidity multiplicity, a 30 × 40 cm drift chamber (a prototype of the current 1.5 × 2.0 m HISS drift chamber), and a two wall Cerenkov hodoscope for measuring fragment velocity and charge.

1.3. Background

Heavy ions (A ≥ 10) at relativistic energies (K ≥ 100·A MeV) were first observed in 1948 with nuclear emulsions and cloud chambers during balloon borne experiments studying cosmic rays in the earth's upper atmosphere[48Fr1]. Subsequent cosmic ray experiments used the mean free path of relativistic heavy ions to measure the interaction cross sections of these nuclei[48Fr2-54Ei] and interpreted these cross sections as geometric cross sections.

The experimental observation that the maximum nuclear density of normal nuclei is approximately a constant independent of A implies that the nucleus can be pictured as a spherical collection of nucleons with a radius given by:

$$R_A = R_0 \cdot A^{1/3} \qquad \textbf{Equ. 1.3.1}$$

(were R_0 is some empirically measured constant dependent on the nuclear density). The strong nuclear force is known to be short range. Therefore, two nuclei of mass numbers A_1 and A_2 will interact strongly only if there is overlap of the nucleons in the respective nuclei. This gives rise to the geometric calculation of the total interaction cross section (σ_I) for two nuclei:

$$\sigma_I(A_1, A_2) = \pi \cdot \left(R_0 \cdot \left(A_1^{1/3} + A_2^{1/3} \right) - b_0 \right)^2 \qquad \textbf{Equ. 1.3.2}$$

(were b_0 is an empirically determined overlap distance). For cosmic rays incident on Pb, Y.Eisenberg used this model (with $b_0 = 0.00$) to calculate a value of $R_0 = 1.2 \times 10^{-13}$ cm[54Ei]($R_0 = 1.25 \times 10^{-13}$ cm if the concept of transparency of nuclear matter at high energy is invoked).

Because the flux of cosmic heavy ions is so low and because scanning techniques for nuclear emulsions and cloud chambers are so man-hour intensive, heavy cosmic rays do not lend themselves to the detailed study of relativistic heavy ion reactions.

Until 1971, the highest energy available in the laboratory for ions heavier than helium was on the order of 10·A MeV. In 1971, the Princeton Particle Accelerator and the Lawrence Berkeley Bevalac ushered in the era of relativistic heavy ion experimentation in the laboratory with relativistic Nitrogen beams[71Wh,71Lo]. Soon afterwards, a wealth of experimental data and theoretical models became available in the field of relativistic heavy ion reactions. From this explosion of information and ideas a number of important fundamental concepts were distilled.

1.4. Physics Motivation

The motivation for studying projectile fragmentation with relativistic heavy ions is essentially two-fold. 1) We wish to investigate, quantify, and understand the fragmentation mechanism. And 2) we want to augment the current base of data on fragmentation cross sections and momentum distributions.

Test of Theory

Beyond the practical uses for such relativistic fragmentation data, we wish to use such data to address the issue of the fragmentation mechanism. Is fragmentation an excitation and decay process where the important parameter in describing the collision is the injected energy spectrum? Or is it more accurately described by an Abrasion-Ablation model where the important issue is the geometry of the colliding nuclei?

Relativistic heavy ions have been available at the Bevalac for more than 15 years. However, very little work has been done with nuclei larger than A = 16 at energies above E = 1.0·A GeV. Because the assumptions underling models like Abrasion-Ablation are poorly suited to small numbers of nucleons and to low velocities, we wanted to extend the study of projectile fragmentation to larger nuclei and higher energies were the assumptions made in the analysis mentioned above might be more valid.

It has been suggested that because fragmentation theories tend to predict very similar inclusive spectra, such inclusive measurements are not sufficient to distinguish between them[88BD]. However, it is quite clear that inclusive measurements *can* be used to reject theories incompatible with experimental observation. That is to say, any theory must first be able to accurately reproduce the simple inclusive spectra measured by experiment before one can expect to use more complex exclusive experiments to distinguish between theoretical models in the future.

Fragmentation Models

When studying relativistic heavy ion collisions, two classifications of events are immediately suggested by the event topography (see Figure 1-1). Events where the incident projectile nucleus reacts with a target nucleus and completely disintegrates into a large number of fragments with low charge are interpreted as having a small impact parameter (i.e. a head-on collision) and are classified as central collisions (Figure 1-1b). Events which

result in at least one relatively large fragment from the projectile nucleus continuing forward at relativistic velocity are classified as peripheral collisions (Figure 1-1a).

a)Peripheral Collision

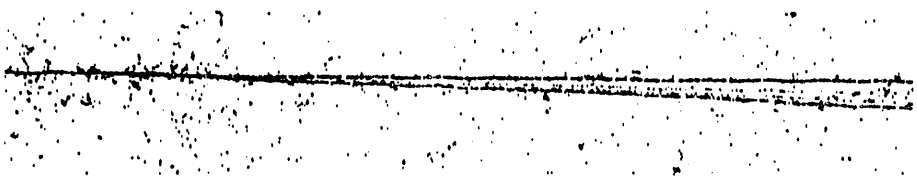

b)Central Collision

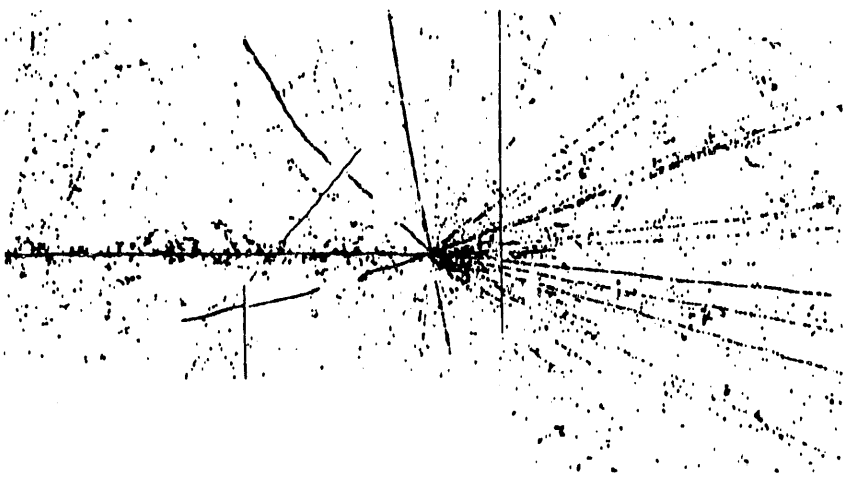

Figure 1-1 : *Tuttle et al (76Tu)*
a)Projectile fragmentation in a peripheral collision of Argon with a nucleus in emulsion resulting in two large fragments of $Z \approx 8$.
b)A central collision (Ar + Emulsion) resulting in approximately 63 fragment tracks.

Experiments with ^{14}N, ^{12}C, ^{16}O, and ^{40}Ar clearly show that the large fragment in a peripheral collision continues with a velocity only slightly less than the initial velocity of the incident projectile(72He,75Gr,79Vi,79Sy). This fact implies that the large projectile fragment has undergone little or no interaction in the collision.

Excitation & Decay Model

Two general pictures have emerged to explain peripheral collisions between relativistic heavy ions. These two pictures differ mainly in the relative importance they assign to 1) the excitation spectrum of the projectile (or target) and 2) the collision geometry of the two nuclei.

Let us suppose that the two nuclei undergo a grazing collision without interpenetration of nucleons from one nucleus into the other. In this grazing collision, the projectile (or target) nucleus is excited by the Coulomb and nuclear fields of the other nucleus and then undergoes statistical decay. This statistical decay can be calculated by the use of standard evaporation codes such as EVE, ALICE, PACE, or GEMINI.

V.K.Lukyanov and A.I.Titov used such an Excitation and Decay Model to successfully explain the general shape of the Q dependence of isotope yields from the fragmentation of 2.1·A GeV ^{14}N(75LT).

D.E.Greiner et al used similar models based on the quantum-mechanical sudden approximation(75LR) or the sudden emission of virtual clusters(73FH) to explain the widths of momentum distributions from the fragmentation of ^{16}O and ^{12}C(75Gr).

However, Y.P.Viyogi et al found that projectile excitation followed by equilibration and decay failed to account for Isotopic Production Cross Sections (IPCS) from the fragmentation of ^{40}Ar at 213·A MeV(79Vi). Instead, Viyogi et al used an Abrasion-Ablation calculation by L.F.Oliveira et al(78Ol,79Ol) to predict the shapes of their IPCS distributions.

Spectator / Participant Model

In peripheral collisions, the observation of persistence of velocity for the main projectile fragment leads naturally to the concept of spectator vs. participant matter in the collision.

To illustrate the principle of spectator and participant matter in relativistic heavy ion collisions, let us return to the picture implicit in Equation 1.3.1. That is, the picture of two spherical nuclei colliding with some impact parameter b (see Figure 1-2).

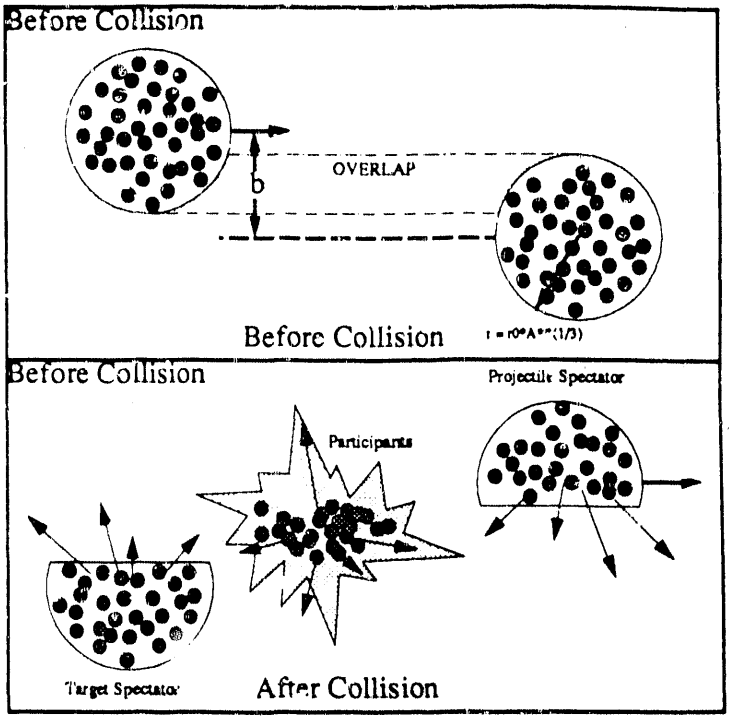

Figure 1-2
Illustration of the principle of the Spectator-Participant matter. a) Before the collision two nuclei approach one another with impact parameter b. b) After the collision, the participant nucleons form a hot, dense region. While the spectator nucleons continue with their initial velocities.

If the two nuclei, A_1 and A_2, approach one another with an impact parameter (b) such that:

$$0 < b \leq b_{max} \equiv R_0 \left(\sqrt[3]{A_1} + \sqrt[3]{A_2} \right) \qquad \text{Equ. 1.4.1}$$

, then some of the nucleons in each nucleus will interact with nucleons in the other during the collision. These nucleons in the overlap region of each nucleus participate in the collision and are consequently called the participant matter.

If the CM velocity of the two nuclei is sufficiently high (i.e. much greater than the Fermi velocity, β_F, within each nucleus) then the overlapping (participant) matter in the two nuclei will be sheared off, unable to interact or communicate with the non-overlapping matter. This spectator matter does not participate in the actual collision, and in fact, does not really "know about" the collision directly at all.

The spectator matter from both the projectile and the target will continue in the CM frame with essentially undiminished velocity. However, since these pre-fragments are greatly distorted from their most energetically favored shape (spherical), they will be highly excited. Thus, each nucleus will de-excite by the emission of neutrons and protons (and perhaps larger clusters) until they reach stability.

This two step process: 1) the prompt shearing off of the participant matter in the collision and 2) the subsequent sequential decay of the pre-fragment to reach nuclear stability, describes the basis of several theoretical calculations including the Abrasion-Ablation Model.

In the Abrasion-Ablation Model, one determines the mass of the pre-fragment by the geometric overlap of the two collision partners. The charge of the pre-fragment is determined by assumptions made in the analysis. In his Ph.D. thesis[78Ol], L.F.Oliveira discusses a number of methods for calculating the charge dispersion of the abraded pre-fragment: 1)projectile A/Z ratio, 2)hypergeometric A/Z dispersion, or 3)correlations between protons and neutrons due to zero-point vibrations of the Giant Dipole Resonance (GDR). He also discusses two ways of determining the excitation energy of the pre-fragment: 1) a calculation based on the excess surface area of the pre-fragment and 2) the same surface area calculation with the addition of a Final State Interaction (FSI) excitation energy. Comparing the isotopic production cross sections calculated by these different methods with the data of Viyogi et al resulted in the conclusion that the best fit was obtained by using the GDR correlation and injecting some additional FSI excitation energy[79Vi,78Ol].

Ideally, we would like to have a theory that takes into account the quantum-mechanical nature of the nucleons involved in the collision, treats the two nuclei relativistically, adheres to the known properties (i.e. energy levels, resonances, etc) of the target, projectile, and fragment nuclei, and results in analytic formulae for the isotopic production cross sections and fragment momentum distributions as a function of ${}^{A}Z_{p}$, ${}^{A}Z_{t}$, ${}^{A}Z_{f}$, and E_{p}.

Such an ideal theory does not exist for RHI collisions so we are forced to make approximations in how the physics is treated, or we can use Monte-Carlo techniques to try to calculate the outcome of experiment.

Monte-Carlo calculations are a well known tool in experimental physics, and are used widely. However, a full Monte-Carlo calculation is not a trivial undertaking. In order to make realistic theoretical predictions of the results of RHI experiments, we would like to have a completely detailed, microscopic Monte-Carlo of many simulated events. (Many events meaning that the statistics of the Monte-Carlo are the same order of magnitude as the statistics of the experiment.)

Such an idealized calculation would, event by event, generate two nuclei (target and projectile) at some time t_0 (when the nuclei are far enough away that they are not interacting) with random impact parameter (obeying the appropriate probability distribution) whose nucleon three-dimensional positions and momenta are specified by random numbers constrained by the known physical properties of the two nuclei. Such physical properties would include the neutron and proton density distributions, the Fermi momentum distributions, all nucleon correlations and anti-correlations in the nucleus, and of course, the laws of conservation of momentum and energy.

The calculation would then follow each nucleon in small time steps as the two nuclei approach one another (in the CM frame) calculating the trajectories of individual nucleons, the forces on each nucleon due to all other nucleons in the system, and the subsequent change in each nucleon's trajectory because of those forces.

During the actual collision, interactions between nucleons would (once again ideally) be calculated using the full nuclear potential, and take into account nuclear shell effects, Pauli blocking, and all other salient physical effects.

After the collision, the formation of clusters, and the breakup and/or evaporation of excited fragments would be calculated with the same detail.

With sufficiently fine granularity in time steps, this kind of calculation would eventually yield a complete description of the final state of the reaction and, run many times in succession, would provide inclusive and exclusive cross sections, momentum distributions, and associated multiplicities with which to compare experiment.

Clearly, such a calculation for collisions between heavy nuclei (where the total number of nucleons in the system can reach 200 or more) would be extraordinarily complex. Although calculations exist for low energy central collisions[88BD] that approach this ideal, no such calculations exist at this time for energies in the 1-2·A GeV energy range. Even if such an idealized calculation existed, it might prove so computer time intensive as to make its practical use impossible.

However, if the number of nucleons in the nucleus is high enough, we might expect that a more macroscopic calculation would yield useful results. If, in fact, we could treat one portion of the reaction in a macroscopic manner (say before and during the collision), and another part in a more microscopic way (after the collision), we could reasonably expect even more realistic results. This is, in effect, the philosophy behind the Abrasion-Ablation Model.

In the Abrasion-Ablation Model as described in References 78Mo, 78Ol, 79Mo, and 79Ol, the target and projectile nuclei are pictured as spheres of nucleons following straight-line trajectories before the collision. The impact parameter of the collision is generated randomly (with a triangular probability distribution), and the volume of nuclear matter removed from nucleon A_1 (for $A_1 > A_2$) is calculated analytically by the equations:

$$F_I = \left(1 - (1 - \mu^2)^{3/2}\right) \cdot \left(1 - (\beta/v)^2\right)^{1/2} \qquad \textbf{Equ. 1.4.2}$$

and

$$F_{II} = \frac{3}{4}\cdot(1 - \nu)^{1/2}\left(\frac{1 - \beta}{\nu}\right)^2 \qquad \textbf{Equ. 1.4.3*}$$

$$-\frac{1}{8}\left(\frac{3\cdot(1 - \nu)^{1/2}}{\mu} - \frac{\left(1 - (1 - \mu^2)^{3/2}\right)\cdot\left(1 - (1 - \mu)^2\right)^{1/2}}{\mu^3}\right)\left(\frac{1 - \beta}{\nu}\right)^3$$

where $\nu = \frac{R_1}{R_1 + R_2}$, $\beta = \frac{b}{R_1 + R_2}$, and $\mu = \frac{1}{\nu} - 1$. The function F_I is used for $0 \le b < R_1 - R_2$, while the F_{II} function is used for $R_1 - R_2 \le b \le R_1 + R_2$.

The distribution of primary fragment masses (Figure 1-3) falls sharply from $A_{pf} = 39$ to a minimum at $A_{pf} = 19$. The minimum value of $A_{pf} = 16$ for the primary fragment reflects the maximum volume of overlap between a ^{12}C nucleus and an ^{40}Ar nucleus.

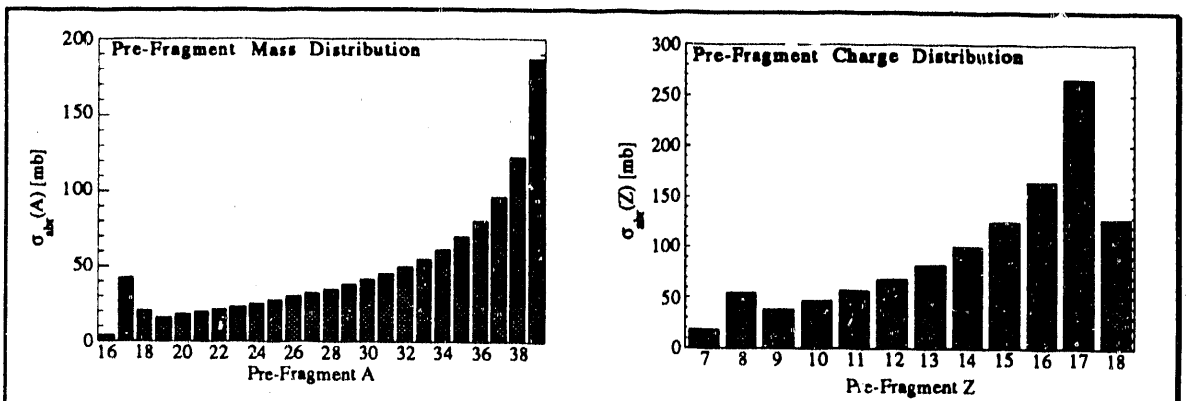

Figure 1-3
Calculated abrasion pre-fragment mass (a) and charge distributions (b) for the reaction $^{40}Ar + ^{12}C$ at 1.65·A GeV under the GDR charge dispersion assumption.

Using Equation 1.3.1 with $R_0 = 1.18$ fm and calculating the average impact parameter for each primary isobar gives the graph in Figure 1-4. For reference, the radii of the two collision partners is shown on the vertical (*b*) axis. The impact parameter marked with the notation *Punch Through* denotes the point below which the ^{12}C nucleus is completely obscured by the ^{40}Ar nucleus.

---

* NB. In Reference 78Mo there is an error in the equation for the analytic formula for $F(\nu,\beta)$. The equation for F_{II} contains a term $\frac{3\cdot(1 - \beta)^{1/2}}{\nu}$, instead of the correct term $\frac{3\cdot(1 - \nu)^{1/2}}{\mu}$.

It is at this point that the intuitive picture of the abrasion stage clearly breaks down. If the impact parameter is equal to or smaller than this Punch Through point ($b \leq 1.34$ fm) the abrasion stage of the model results in the unphysical picture of the ^{12}C nucleus punching a hole through the ^{40}Ar nucleus, producing a donut-shaped primary fragment. Although it seems that such an unphysical result would invalidate the theory, we can still use the calculation for peripheral collisions with relative confidence.

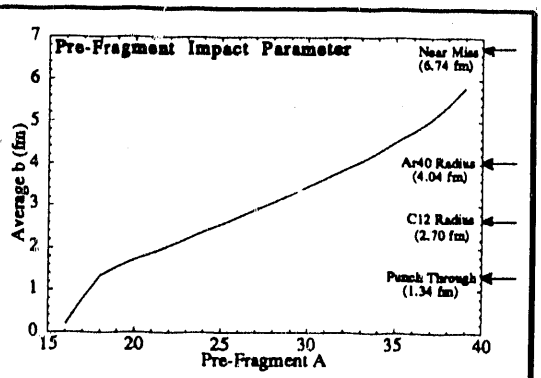

Figure 1-4
The impact parameter for the abrasion stage of an Abrasion-Ablation calculation ranges from a minimum of $b_{min} = 0$ to a maximum of $b_{max} = R_1 + R_2$.

Once the mass of the pre-fragment has been calculated, its charge must be determined before the ablation part of the calculation is made. The two most extreme assumptions about the Z/A ratio of the pre-fragment one can make are 1) Total correlation between protons and neutrons in the projectile, and 2) No correlation between protons and neutrons in the projectile.

If we assume total correlation between the protons and neutrons, the charge of the pre-fragment (Z_{pf}) would be determined by the charge to mass ratio of the original projectile.

$$Z_{pf} = \frac{Z_p \cdot A_{pf}}{A_p} \qquad \textbf{Equ. 1.4.4}$$

(i.e. The pre-fragment and the initial projectile have the same Z/A ratio.)

If we assume that there is no correlation between protons and neutrons in the projectile nucleus (i.e. the probability that a nucleon knocked out of the projectile by the interaction is a proton is given by P(p) = Z/A), then the pre-fragment charge dispersion is given by the hypergeometric function(77Ra):

$$\sigma(Z, A) = \left(\frac{\binom{Z_p}{z}\binom{N_p}{n}}{\binom{A_p}{a}} \right) \sigma(A) \qquad \textbf{Equ. 1.4.5}$$

Where $A = A_p - a$ and $Z = Z_p - z$ are the mass number and atomic number of the pre-fragment; Z_p, N_p, and A_p are the number of protons, neutrons, and nucleons in the projectile, and z, n, and a are the number of protons, neutrons, and nucleons removed from the projectile by the abrasion process.

Rather than choose one of these limiting cases, an intermediate assumption has been suggested that takes into account the fluctuation of proton and neutron densities due to the zero-point vibrations of the Giant Dipole Resonance (GDR). The giant dipole resonance is a collective oscillation of the neutrons against the protons. If the neutrons and protons are visualized as two spherical collections of particles, the vibration of these two spheres about some center will cause a dispersion in charge for a single value of mass loss (ie. for a specific range of impact parameter).

Regardless of the prescription used to determine the pre-fragment's charge, the next step in the calculation is the same. At this stage, we have an intermediate pre-fragment nucleus with mass, charge, and excitation energy A_{pf}, Z_{pf}, and E_{pf}^*, respectively. Using these parameters we can run an ablation code to calculate the de-excitation of the pre-fragment.

In the four References 78Mo, 78Ol, 79Mo, and 79Ol, the code used for this stage of the analysis was OVERLAID-ALICE which allows de-excitation by fission and emission of neutrons, protons, and α-particles. The pre-fragments were assumed to have negligible angular momentum ($\leq 10\hbar$) for the calculation.

In comparison with data[78Ol,79Vi], it was found that the experimental element yields could be well fit (within an overall normalization factor) by both the assumption of no correlation (NC) and by the assumption of proton-neutron correlation due to the GDR. However, it was concluded that the shape of the isotopic production cross sections was not well produced by the NC assumption. The GDR assumption for the pre-fragment charge

dispersion *did* however, reproduce the shapes of the IPCSs. Figure 1-5 shows the IPCSs of nine elements as measured by Viyogi et al, and as calculated using the Abrasion-Ablation Model under the above two assumptions. The AA curves are normalized to reproduce the maximum experimental isotope cross section for each element.

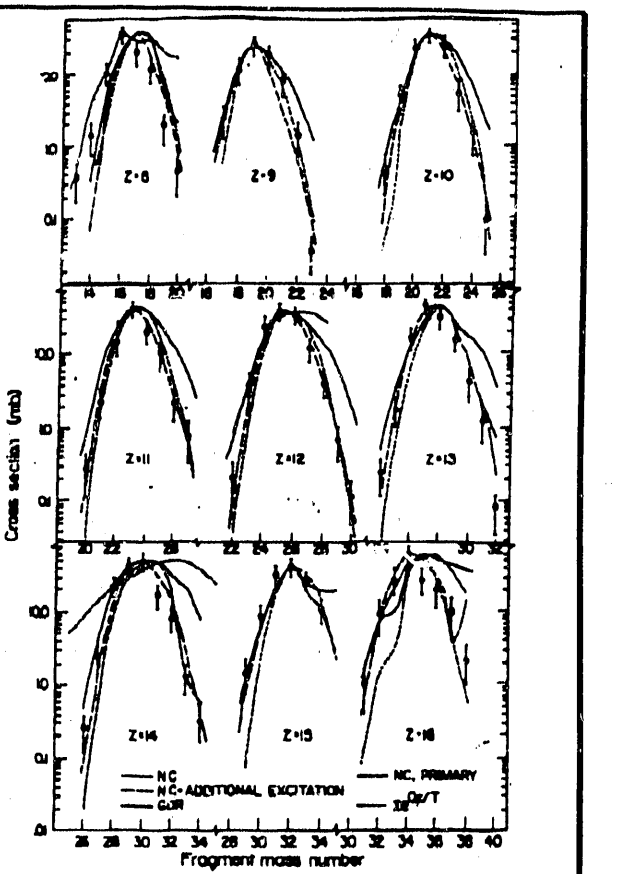

Figure 1-5: *Viyogi et al (79Vi)*
Comparison of experimental isotope production cross sections for Ar+C with model predictions as described in text. The calculated curves have been normalized to reproduce the maximum experimental isotope cross section in each case. The normalization factors varied between 1 and 2.

It was found that the shapes of the IPCS curves could be reproduced by the NC or GDR assumption provided that an additional exci. tion energy term was added. This excitation term has been called the Frictional Spectator Interaction, or the Final State Interaction (FSI in either case) term This term arises from the recognition that at high energy ($E \geq 1.0$ GeV), the nucleon-nucleon elastic scattering cross section is highly forward peaked in the lab.

Hence, the collision between target and projectile nucleons can be visualized as resulting in the projectile nucleon proceeding in a forward direction (beam direction) and the target nucleon moving perpendicular to the beam direction. Since the momentum transfered to the struck target nucleon is in the impact-parameter plane, a struck nucleon is either knocked away from, or towards the spectator region. If the struck nucleon scatters into the spectator, it will deposit additional excitation energy of some average value $\langle E_{fsi} \rangle$.

Oliveira[7801] justified the use of $\langle E_{fsi} \rangle = 40$ MeV for comparison with Viyogi et al's 213*A MeV ^{40}Ar + C data. Further, Oliveira argues that each nucleon has a 50% chance of undergoing an FSI and, therefore, each pre-fragment with mass number $A_i = A_p - a$ can have an additional excitation energy within the range $E_{fsi} = [0, a \cdot \langle E_{fsi} \rangle]$ corresponding to the range of possible number of final state interactions ($m_{fsi} = [0, a]$). The probability of m_{fsi} final state interactions follows the binomial distribution (Figure 1-7):

$$\text{Prob}(m_{fsi}) = \frac{\binom{a}{m_{fsi}}}{2^a} \qquad \textbf{Equ. 1.4.6}$$

whereas the surface energy increases monotonically for increasing participant region volume (Figure 1-6).

In Figure 1-5, the curves labeled *NC+ADDITIONAL EXCITATION* are the results of Oliveira's Abrasion-Ablation calculation using the hypergeometric charge dispersion and FSI excitation energy parameter $\langle E_{fsi} \rangle = 40$ MeV.

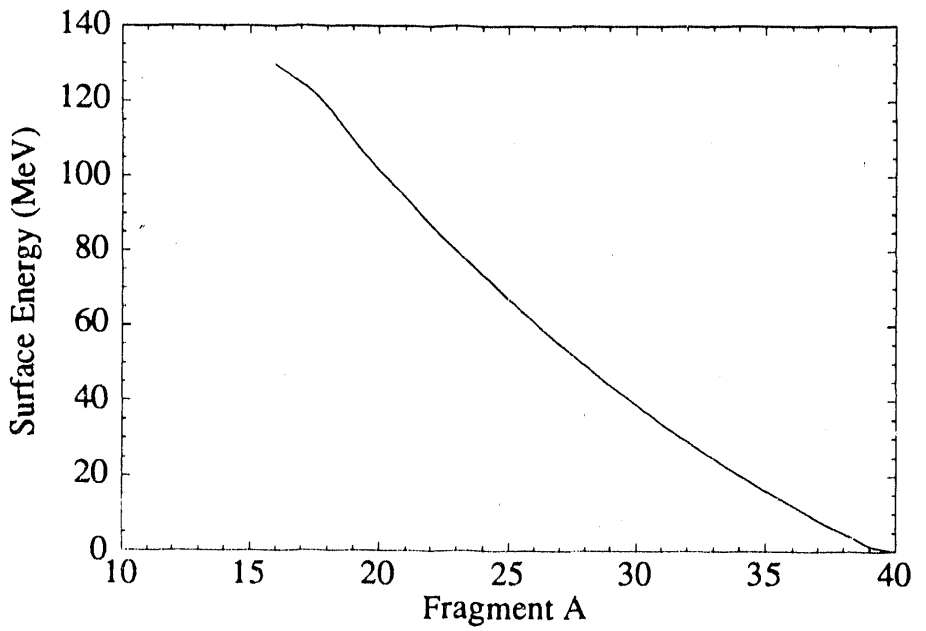

Figure 1-6
The surface energy of the abrasion stage is 0.95·S, where S is the excess surface energy of the abraded nucleus compared to a spherical nucleus of the same volume.

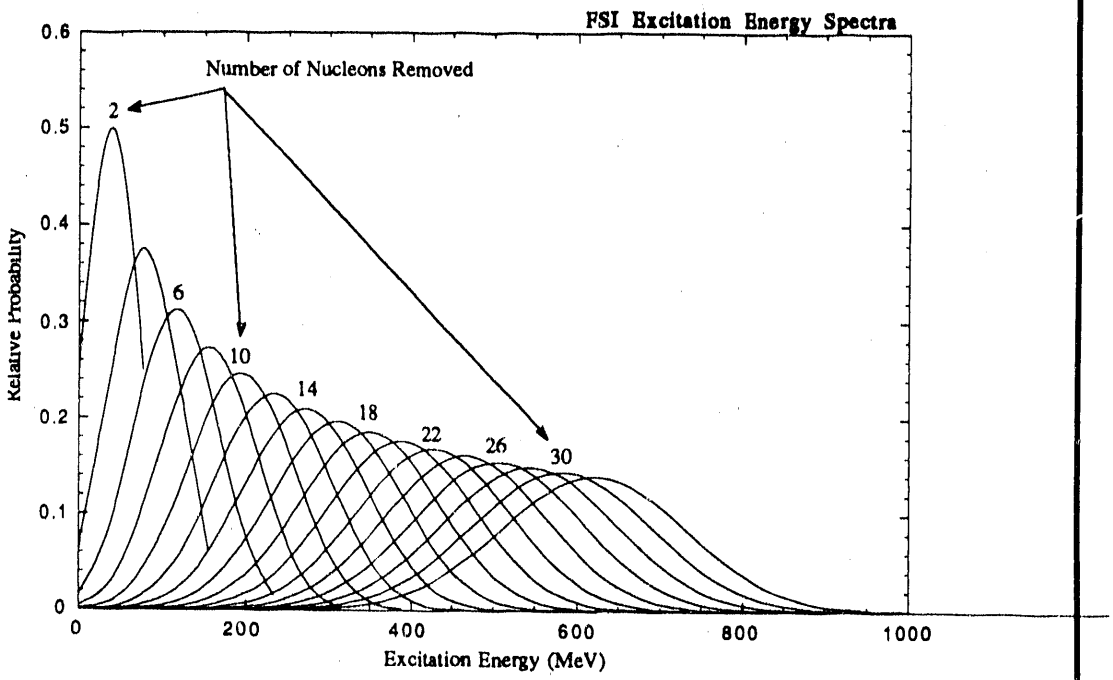

Figure 1-7
The shapes of the FSI excitation energy spectra for even mass number loss from ^{40}Ar are binomial with peaks at $40 \cdot \Delta A/2$ MeV.

Momentum Distributions

When heavy ions were first accelerated to relativistic energies, one of the first results to emerge from experiment was the persistence of the mean velocity of projectile fragments and the gaussian shape of fragment momentum distributions (72He). The widths of these gaussian momentum distributions were independent of the target and described by the equation:

$$f(p) \approx \exp\left(\frac{-p^2}{2\cdot(m_\pi\cdot c)^2}\right) \approx \exp\left(\frac{-2\cdot p^2}{p_F{}^2}\right) \qquad \textbf{Equ. 1.4.7}$$

where p is the fragment longitudinal momentum, m_π is the pion mass, and $p_F \approx 2\cdot m_\pi\cdot c$ is the Fermi momentum of the incident projectile.

The first attempts to understand the gaussian shapes of the fragment momentum distributions used the quantum mechanical sudden approximation(74LR) with shell-model

nuclear wave functions based on harmonic oscillator potentials for the nuclei, or an incoherent droplet model[73FH] assuming sudden emission of virtual clusters.

The sudden approximation model employed by Lepore and Riddell assumed that the nuclear wave functions for the colliding nuclei do not change during the interaction. This results in the probability of a final state being given by the overlap integral between the initial and final states. Although they are able to calculate only relative cross sections with this model, this allows the determination of the probability distribution for a final state fragment's momentum. This distribution is given by:

$$C \cdot \exp\left(\frac{-p^2}{2 \cdot \sigma^2}\right) \qquad \textbf{Equ. 1.4.8}$$

where the standard deviation of the Gaussian is given by:

$$\sigma = \left(\frac{A_f \cdot (A_p - A_f)}{4 \cdot \alpha_p \cdot A_p}\right)^{1/2} \qquad \textbf{Equ. 1.4.9}$$

where A_f, and A_p are the mass numbers of the fragment and projectile, and α_p is related to the harmonic oscillator force constant.

The statistical fragmentation model of Feshback and Huang predicts inclusive momentum distributions that are Gaussians with widths given by:

$$\Delta p_{hw} = \langle p^2 \rangle \cdot \left(\frac{A_f}{3 \cdot n}\right) \qquad \textbf{Equ. 1.4.10}$$

where Δp_{hw} is the half-width of the Gaussian, A_f is the mass of the projectile, and n is the total number of fragments resulting from the collision. Feshback and Huang compared this form with the empirical result of Equation 1.4.7 and concluded that $\langle n \rangle \approx 7$.

Subsequent experimental data refined the relationship in Equation 1.4.7, showing that the longitudinal momentum distribution widths for projectile fragments from relativistic ^{12}C and ^{16}O obey the functional form[75Gr]:

$$\sigma_p^2 = 4 \cdot \sigma_g^2 \cdot \left(\frac{A_f \cdot (A_p - A_f)}{A_p^2}\right) \qquad \textbf{Equ. 1.4.11}$$

where σ_g is a fitted parameter. Greiner et al compared their data to the theories of L&R and F&H by defining the constant σ_g as:

$$\sigma_g = \frac{m_p}{8} \cdot (A_p)^{1/3} \cdot (45 \cdot (A_p)^{1/3} - 20) \text{ MeV/c}^2 \qquad \textbf{Equ. 1.4.12}$$

for the quantum mechanical model of Lepore and Riddell (where m_p is the proton mass), and as:

$$\sigma_g = \frac{p_F}{20} \cdot \frac{A_p^2}{(A_p - 1)} \qquad \textbf{Equ. 1.4.13}$$

for the statistical fragmentation model of Feshbach and Huang (where p_F is, once again, the Fermi momentum of the projectile nucleus). Greiner et al also observed that the experimental momentum distributions were centered at slightly negative values of p_L indicating a loss of kinetic energy from the projectile.

A.S. Goldhaber showed that the experimentally measured parabolic dependence of the momentum width (σ) on the fragment mass (A_f) can be predicted explicitly from two very different models of the fragmentation process[74Go]. Under minimal assumptions (ie. that the original projectile nucleus is a Fermi gas of uncorrelated nucleons, and that momentum is conserved in the reaction) Goldhaber's models predict Gaussian momentum widths in all three coordinates with variance:

$$\sigma^2 = \sigma_0^2 \cdot \left(\frac{A_f \cdot (A_p - A_f)}{(A_f - 1)} \right) \qquad \textbf{Equ. 1.4.14}$$

where A_f and A_p are defined as in Equation 1.4.9, and σ_0 is a constant different from σ_g. Further, Goldhaber relates the constant σ_0 to physical quantities of the fragmenting system for both of his approaches.

Goldhaber's first approach was to assume that the fragmentation mechanism is a fast process and that, hence, fragmentation statistically samples the momentum distribution of nucleons within the projectile nucleus. Under this assumption, the momentum distribution of a projectile fragment should reflect the vector sum (constrained by momentum conservation) of the individual momenta of the nucleons that constitute that fragment. Goldhaber showed that the width of the momentum sum of a random sampling of nucleons with a Fermi distribution is given by Equation 1.4.14. Under this model of the fragmenta-

tion process the reduced momentum width (σ_0) is related to the Fermi momentum of the incident projectile (p_F) by:

$$\sigma_0^2 = \frac{p_F^2}{5} \qquad \textbf{Equ. 1.4.15}$$

The Fermi momentum of a particular nucleus can be measured by such techniques as electron scattering, and the subsequent value of σ_0 compared with that obtained by RHI experiment.

Goldhaber's second model views fragmentation not as a prompt mechanism, but as a relatively slow process. Let us assume that the projectile nucleus is excited in the collision, equilibrates at some temperature T, and then de-excites by particle emission (a relatively slow process). Goldhaber found that the momentum distributions are once again Gaussian with widths described by Equation 1.4.14. However, σ_0 is now related to the equilibrium temperature T by:

$$\sigma_0^2 = \frac{m_n \cdot kT \cdot (B-1)}{B} \qquad \textbf{Equ. 1.4.16}$$

where m_n is the nucleon mass and $k = 8.6 \times 10^{-5}$ eV·K^{-1} is Boltzmann's constant.

Although the three theoretical papers above approach the calculation of momentum distribution shapes in different ways, all three make similar basic assumptions. The initial vector sum of the nucleon momenta in the projectile nucleus is zero and momentum is conserved in the reaction. The theories of Goldhaber and of Feshbach and Huang make the additional assumption that correlations between the nucleon momenta in the initial projectile can be neglected.

Viyogi et al also observed gaussian momentum distributions in the longitudinal direction and evaluated the widths in terms of Goldhaber's reduced momentum width σ_0. Figure 1-8 shows the value of σ_0 plotted vs fragment mass number. The average value of σ_0=94 ± 5 MeV/c yields values of p_F = 209±11 MeV/c and kT = 9.6±1.1 MeV/nucleon. These values are lower than expected from Fermi momentum (p_F = 251±5 MeV/c from

electron scattering off ^{40}Ca), but are within uncertainty of the binding energy per nucleon of ^{40}Ar (E_{bind} = 8.6 MeV/nucleon).

Recently, the relatively simple theory that Goldhaber put forth has been extended by the addition of Pauli momentum anticorrelations between projectile nucleons(81Be), and by consideration of phase-space constraints on the final state of the system(84Mu).

Bertsch has pointed out that the description of the projectile nucleus as a Fermi gas of A_p uncorrelated nucleons neglects the important contribution to the momentum widths due to the effects of Pauli correlations. Rather than a collection of totally uncorrelated nucleons as postulated by Goldhaber, one expects that identical nucleons spatially close to one another will have a strong anticorrelation in momentum because of the Pauli Principle. The Spectator-Participant Model explicitly removes nucleons that are spatially correlated, and hence implies the removal of nucleons whose momenta are anticorrelated. Referencing an earlier calculation with J. Borysowicz(79BB), Bertsch calculates a reduction in fragment momentum widths for ^{40}Ar of 36.6% relative to the independent particle model of Goldhaber.

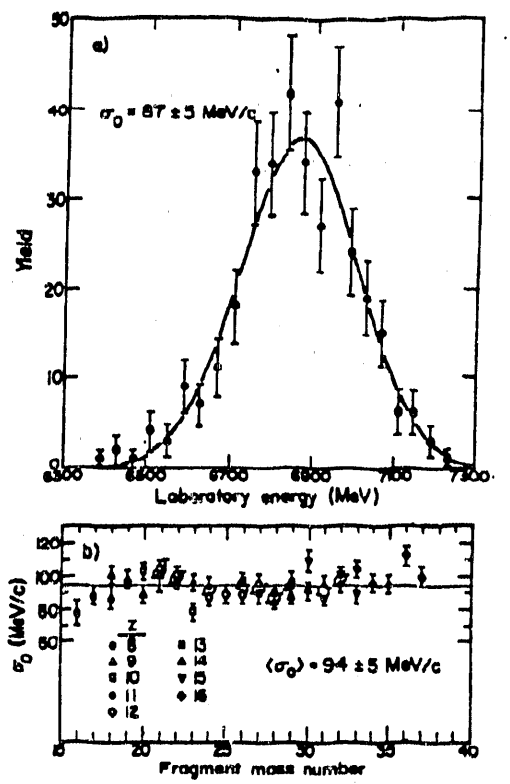

Figure 1-8: *Viyogi et al (79Vi)*
(a)Measured energy spectrum of ^{34}S at 1.5° from fragmentation of 213 MeV/nucleon ^{40}Ar on a carbon target. The solid line corresponds to a fitted Gaussian momentum distribution.
(b)Values of σ_0 for the fragments in the mass range 16 to 37. (For each fragment, the weighted mean of σ_0 obtained from the energy spectra at many angles is shown.)

It should be noted that the discussion and calculation in Reference 81Be pertains to the longitudinal momentum dispersion of fragments produced by removal of matter delineated in the transverse direction. (Bertsch does his calculation employing the single particle operator $O = p_z \cdot f(x,y)$, where f = 0 or 1 in the regions of the projectile nucleus that are removed or remain in the fragment.). Bertsch postulates that since fragmentation produces a spatial correlation in the transverse direction, the momentum anticorrelations should be enhanced transversely.

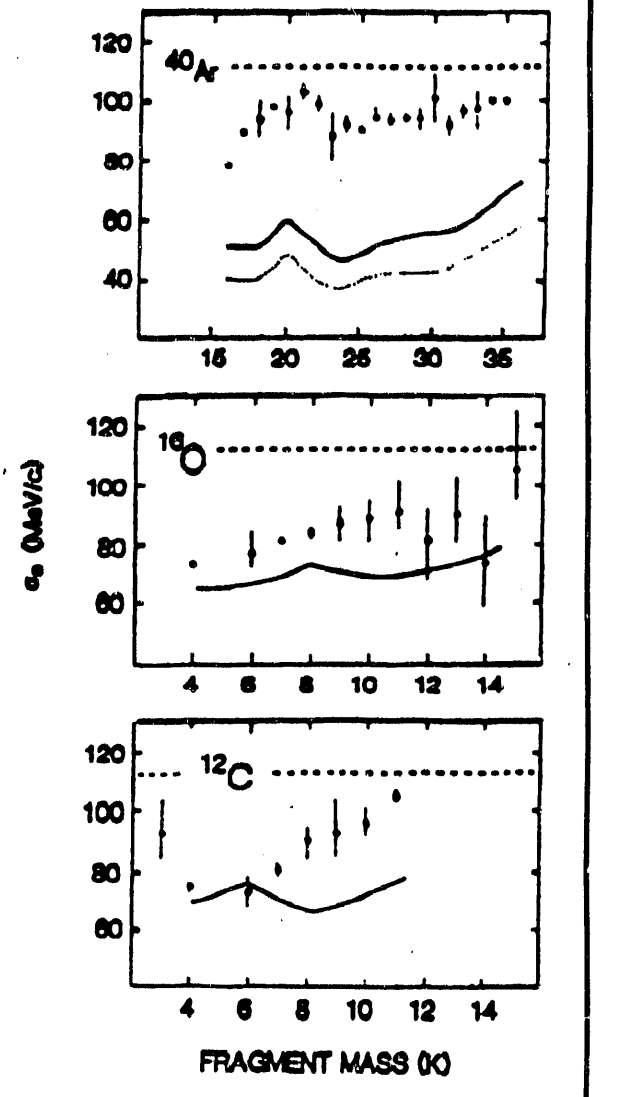

Figure 1-9 *Murphy (84Mu)*
Suppressing the reduced momentum widths (σ_0) of Goldhaber's prediction (Horizontal dashed line) by inclusion of phase-space effects gives the solid line. The dotted line for ^{40}Ar includes additional suppression due to the Pauli Principle.

Another effect that narrows the fragment momentum distributions has been put forth by Murphy(84Mu). Murphy points out that under the minimal assumptions of Goldhaber's treatment, many unphysical final state nuclei are permitted. To be more realistic, the projectile fragments should be required to be Fermi gases. This assures that no final states exist consisting of unbound nuclei, or for which the momentum distribution is unrealistically skewed. Murphy calculated reduced momentum widths (σ_0) for fragments from ^{40}Ar, ^{16}O, and ^{12}C, and compared these values with the data of References 79Vi and 75Gr. Although his calculated values of σ_0 show dependence on A_f

similar to that seen in the data, the absolute magnitude of the calculated widths are too narrow (see Figure 1-9).

One notable lack in the experimental record is the measurement of transverse momentum distributions. Although Greiner et al and Viyogi et al both observed that the transverse momentum distribution widths are equal to the longitudinal widths (within ≈ 10%), neither experiment measured the p_T distributions with enough accuracy to draw quantitative results.

One experiment where transverse momentum distributions widths are quoted was performed at HISS using the MUltiple Sampling Ionization Chamber (MUSIC)(88Br). This experiment measured the charge and opening angle in one plane for projectile fragments from 1.2·A GeV ^{139}La. It was found that under two assumptions on the charge to mass ratio of the fragments, the momentum distributions were much wider than expected by the predictions of Goldhaber, or Lepore and Riddell. Although the two assumptions made about the charge to mass ratio are not in agreement with direct measurements of final fragments(89Mo1,89Bi), the Goldhaber model of Fermi distribution sampling should be compared with the pre-fragment for which the assumptions are valid.

Other concepts important to the field of relativistic heavy ion fragmentation should be mentioned here. Concepts like factorization and limiting fragmentation have played important roles in the interpretation of experimental data(79We,83Ol) while empirical models for calculation of isotopic production cross sections have provided a valuable tool for practical calculations, both in relativistic heavy ion experiments and in such fields as cosmic ray astrophysics(73ST1,73ST2).

Improvement of Data Base

Another motivation for experimental measurements of this nature arises from the use of interaction cross sections, elemental and isotopic production cross sections, momen-

tum distribution widths, and momentum down-shifts to make practical predictions for and interpretations of experimental data in relativistic heavy ion physics and astrophysics.

Of the results obtained in this experiment, the most obviously useful are the inclusive isotopic production cross sections (IPCSs) we have measured. One area in which the relevance of these measured IPCSs is immediately apparent is the study of galactic cosmic rays detected in the Earth's upper atmosphere. Cosmic rays detected at Earth have passed through grams of interstellar material during their travels across the galaxy. If one wants to know the composition of these cosmic rays at their source, accurate values for production cross sections at cosmic ray energies must be known.

In practice, it is not practical to measure all the isotopic production cross sections for all possible projectile-target combinations and for all energies of interest. Therefore, the normal procedure is to use some method of extrapolation from known (measured) cross sections to unknown cross sections.

One such method is detailed by Silberberg & Tsao in References 73ST1 and 73ST2. Silberberg & Tsao's semi-empirical formula takes experimentally measured cross sections, fits a set of parameters to the measured data, and uses these parameters to calculate production cross sections (given the target and projectile species, and the projectile energy) for unmeasured fragments of interest. This type of semi-empirical formula depends heavily on the amount and accuracy of the empirical data on which it is based. Outside of the energy and/or mass limits of the underlying data, there is no guarantee that the formula will be applicable.

Hence, there is always interest in measuring cross sections that have previously been unmeasured. The paucity of projectile fragmentation data above 1.0 GeV and A=16 is clear motivation to make measurements in this region.

Although the practical considerations above are important when considering the results of our experiment, they do not give us any insight into the nuclear processes involved

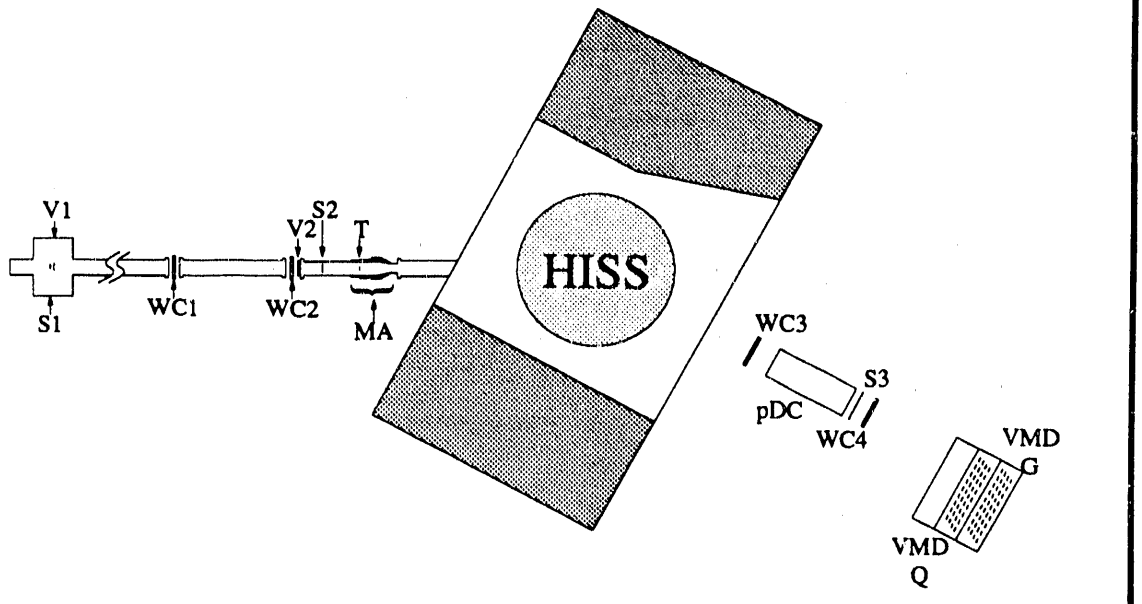

Figure 2-1
A top view of the experimental setup for E772H.

in the collision. Our main motivation is to gain insight concerning the fragmentation mechanism.

2. Experimental Setup

A top view of the detector setup used in our experiment is shown in Figure 2-1. In the figure, the beam comes from the left, down the beam line from the Bevatron. The beam passes through two beam definition scintillators (S1 and V1) and then through three focusing magnets just downstream. After the focusing magnets, the beam passes through two wire chambers (WC1 and WC2), through another pair of trigger scintillators (V2 and S2) and finally strikes the target located within the multiplicity array (MA).

After hitting the target, the beam and projectile rapidity fragments continue downstream through the HISS dipole magnet. For our experiment the magnet was set at a field of 16 kGauss (1225 Amps of current). At this field setting, the beam rigidity fragments are deflected by approximately 18° into the downstream detectors.

Downstream of the magnet, the beam and fragments pass through one wire chamber (WC3), the prototype drift chamber (pDC), a beam veto scintillator, and another wire chamber (WC4). Finally, the beam and fragments continue through the glass and quartz walls of the Velocity Measuring Device (VMD) and out of the detector system into a beam dump.

2.1. Trigger Scintillators

The S1-V1 pair is located within an aluminum prep box (at vacuum) located at beam focus F5 (approximately 13.5 m upstream of the center of the HISS dipole). Centered in the beam line, S1 is 4 cm wide × 4 cm high × 20 mil-thick and is viewed by one photomultiplier tube. Just downstream of S1, and also centered with the beam line, V1 acts as an active beam collimator. V1 consists of a 4" wide × 4" high × 0.25" thick scintillator with an 1" hole in its center (the center of the beam line) viewed by one photomultiplier tube.

The discriminator thresholds for both S1 and V1 were set as low as possible without triggering on noise. This is necessitated by the occurrence of particles in the beam line of charge lower that the beam. The threshold for V1 was set low to veto events with any particle outside the beam envelope (i.e. beam, or fragments from S1 or other upstream targets). The threshold for S1 was set low to trigger the UDOS circuit (see Section 2.2) on all preceding particles in the beam line within 375 nsec before the trigger particle.

The S2-V2 scintillator pair are located at beam focus F6 (approximately 3.5 m upstream of the center of the HISS dipole) and are very similar in general purpose to the detectors at F5. However, the discriminator thresholds on S2 and V2 are set higher than the S1 and V1 thresholds. V2 is an active collimator 8" wide × 8" high × 0.25" thick with an 1" hole in its center and is centered on the beam line just upstream of the entrance window of the multiplicity array to eliminate beam halo. Unlike V1, the discriminator threshold on the single PMT of V2 was set just below the threshold for beam charged particles. This

prevented back-scattered protons from the target from vetoing an event. Because there is more material directly upstream of V2, V2 was larger than V1.

The beam scintillator S2, is 2" wide × 2" high × 20 mil thick and viewed by one PMT. S2 was centered on the beam line and placed inside the vacuum pipe forming the inner wall of the Multiplicity Array. This means that the 20 mils of scintillator of S2 is the very last material the beam passes through upstream of the target. Hence the discriminator threshold on the S2 PMT was set to fire only on charges of $Z > 17$. This provides a last check that the beam has not fragmented upstream of the target.

The final trigger scintillator in our system is S3. S3 is a scintillator 40 cm wide × 30 cm high × 0.25" thick viewed by two PMTs and located just downstream of the prototype drift chamber. The intention for S3 was to set the discriminator thresholds on S3 to fire only on $Z > 17$. Thus, requiring that S3 not fire for an event where S2 did fire is equivalent to requiring that the beam nucleus in that event does not undergo a charge-loss reaction between the two scintillators. As mentioned above, the S3 discriminator levels were too low and hence, the trigger efficiency for $Z_f \geq 16$ was reduced.

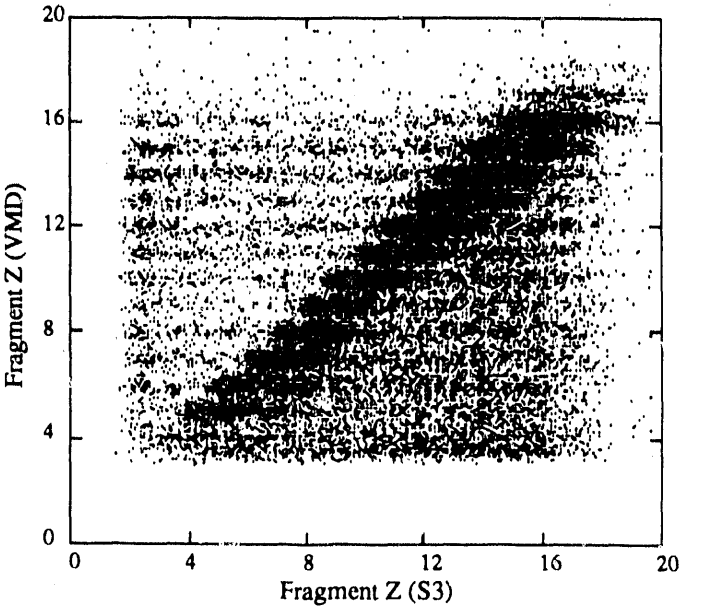

Figure 2-2
Scatter plot of fragment charge measured in the VMD vs. charge in the S3 beam veto scintillator. Points below the 45° correlation result from charge changing reactions between the two detectors.

The trigger scintillator S3 was also used in off-line analysis for measuring the fragment charge (see Section 3.3). Although the charge resolution was not good enough to

separate individual charges (see Figure 2-2), it was sufficient to provide a consistency check of the fragment charge measured in the VMD.

2.2. Triggers

Two triggers conditions were used in our experiment. 1) The interaction trigger (INT) was used to take fragmentation data, while 2) the beam trigger (BEAM) was used for calibration and normalization purposes.

The logic of the trigger can be briefly outlined as below:

Name	Logical Condition Met	Comment
F5	$S1 \cdot \overline{V1}$	Particle within beam envelope at F5
F6	$S2 \cdot \overline{V2}$	Beam particle within beam envelope at F6
WC	$WC1_x \cdot WC1_y \cdot WC2_s \cdot WC2_t \cdot WC2_u$	All 5 planes of the USWCs Fired
BOT	$F5 \cdot F6 \cdot \overline{WC}$	Beam On Target
BEAM	$BOT \cdot \overline{UDOS}$	Beam without pile up
S3	$S3_{east} \cdot S3_{west}$	Coincidence between the two S3 PMTs
INT	$BEAM \cdot \overline{S3}$	Interaction

Table I: Trigger logic levels.

All of these trigger levels are scaled and recorded in the data stream at the end of each Bevatron beam spill (approximately every 200-300 events).

The scintillators S1 and S2 fire when a particle is present in the beam line. The active collimators, V1 and V2, fire if that particle (or some other) is detected outside of the expected beam phase space envelope. Requiring that all five planes of the UpStream Wire Chambers (USWCs) fire reduces the trigger rate, but ensures that the momentum of the detected particle can be reconstructed. The UpDating One Shot (UDOS) is a NIM module built in-house by I.Flores for use in experiments at HISS and Beam 40. The UDOS circuit is triggered by S1, generating an output with a width of 375 nsec (this width is adjustable). If a second particle fires S1 at some time t_{pu} within that 375 nsec window, the UDOS clock resets (while the output remains TRUE), causing the UDOS output to remain logically TRUE for a length of time $t_{udos} = t_{pu} + 375$ nsec. The UDOS clock can be reset any num-

ber of times, resulting in the UDOS output remaining true until a period of 375 nsec has elapsed without the S1 discriminator firing. Vetoing on the delayed UDOS output eliminates events preceded by another particle other than the original trigger particle within the time window of sensitivity of the detector system. This time window is determined by the detector with the longest collection time. In our case this was the prototype drift chamber ($t_{drift} \leq 211$ nsec).

The discriminator level on S3 was set to fire on beam particles. The $\overline{S3}$ requirement for the INT trigger insured that the beam underwent a charge changing reaction before reaching S3. In practice, the threshold for S3 was set too low during our experiment ($Z_{disc} \approx 16$ rather than 18). This eliminated some fragments of interest and necessitated the application of a trigger efficiency correction for the isotope populations near the beam (see Section 3.4).

2.3. Upstream Wire Chambers

The upstream vectoring was done by a pair of MultiWire Proportional Counters (MWPCs). The first wire chamber (WC1) consisted of 2 planes of wires; one plane ($WC1_x$) measuring the horizontal position of a beam particle; the other plane ($WC1_y$) measuring the vertical position. The second wire chamber (WC2) consisted of 3 planes of wires. The three planes ($WC2_s$, $WC2_t$, and $WC2_u$) contained wires oriented at 0°, +30°, and -30° from the vertical. The first plane ($WC2_s$) measures horizontal position, while the combination of the other two planes ($WC2_t$ and $WC2_u$) provided a vertical position measurement.

Each of the five wire planes in the upstream wire chambers contained approximately 150 wires at a 1 mm pitch. Using the number of wires that fire in a cluster (either even or odd), provides a position resolution of 0.5 mm per plane.

Due the beam optics, upstream beam tracks show a strong position-angle correlation in both the horizontal and vertical directions (The wire chambers are not located at a beam focus.). If we know the correlations in each coordinate, we can calculate the beam track position at the target from a single upstream (x, y) position measurement. Using the two UpStream Wire Chambers (USWCs), we measured the beam focus correlations for a large number of events for a particular focus (see Figure 3-1). We then used these measured correlations and the two wire chamber (x, y) positions to project two (x_t, y_t) positions at the target on an event-by-event basis. Averaging these two positions, we obtain the beam spot profile at the target shown in Figure 2-3. The 2" circular hole in V2 can be seen as the outermost limit of points on the scatter plot. The shape and position of the beam envelope (a vertically oriented ellipse in the center of the V2 hole) can be seen by the cluster of dense points in the plot. And the fact that WC1 is missing one horizontal wire and WC2 is missing one diagonal wire is reflected by the bands of missing points across the plot.

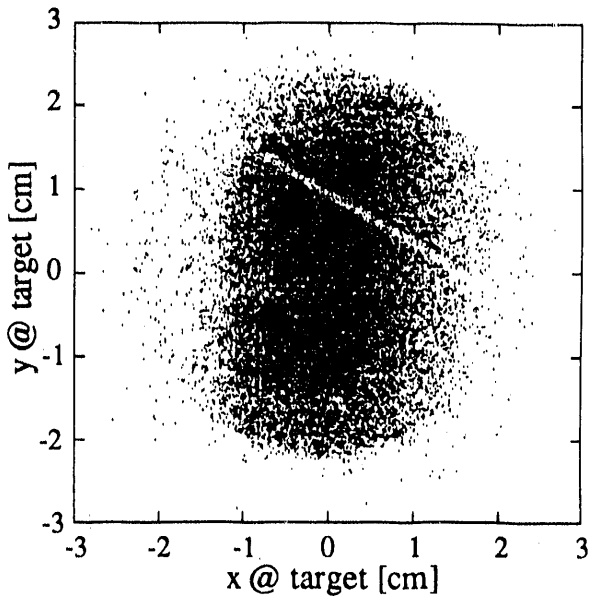

Figure 2-3
Beam spot at the target as measured by the upstream wire chambers (WC1 & WC2).

2.4. Multiplicity Array

The multiplicity array is an 120 element scintillator hodoscope designed to measure the multiplicity of charged particles (mostly protons) in the mid-rapidity region. It was initially built by the Schroeder-Nagamiya group for use in the Beam 30 line. The only signifi-

cant modification made to its design for use in our experiment was the enclosure of the array in a box of 1" thick soft iron for magnetic shielding purposes.

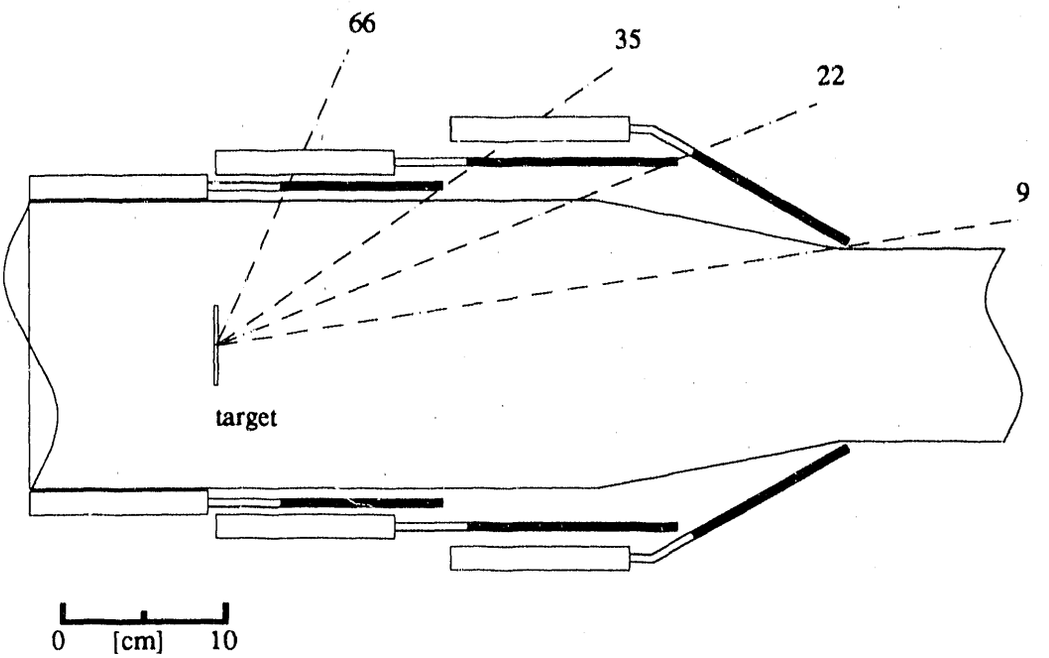

Figure 2-4
The multiplicity array consists of 3 co-axial conic sections of 40 PMT's each and detects charged particles between 9° - 66° in the lab.

The 120 (0.5 × 1 × 10 cm) scintillators are distributed among three co-axial rings of 40 scintillators each (see Figure 2-4). With the target configuration used in our experiment, these rings cover azimuthal angles from 9°-66° in the lab.

The scintillators were automatically gain-calibrated using a ^{207}Bi source located on each scintillator end providing a reference signal[89Ko]. To eliminate random coincidences, 1-nsec TDCs were recorded for each MA element. Figure 2-5 shows the TDCs for approximately 50K events. The horizontal stripe at $TDC_0 = 406.5 \pm 1.3$ are the valid TDC values. Random coincidences form a uniform background of $\leq 0.5\%$. We can see from Figure 2-5 that there appear to be no hot tubes (i.e. from light leaks or faulty bases). However, we also see that 11 of the 120 channels show no valid signals at all. These channels correspond to PMTs physically missing from the array.

To insure that an event has the appropriate multiplicity associated with it, only TDCs in the range TDC = (390,420) are counted for each event. Shown in Figure 2-6 is the resultant multiplicity distribution for the C target, INT trigger under this cut.

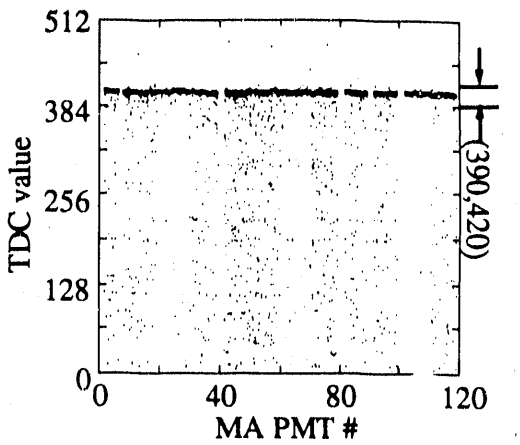

Figure 2-5
Scatter plot of TDC channel vs. phototube number for the multiplicity array.

The difference between the Target-Out and Target-In multiplicity distributions (see Figure 2-6) is indicative of interactions occurring in the target rather than the background matter. The target in distribution shows a sharper peak at low multiplicity, a signature of no reaction in the target. The target out run shows a longer tail at high multiplicity, indicating a higher percentage of events with a reaction in the target.

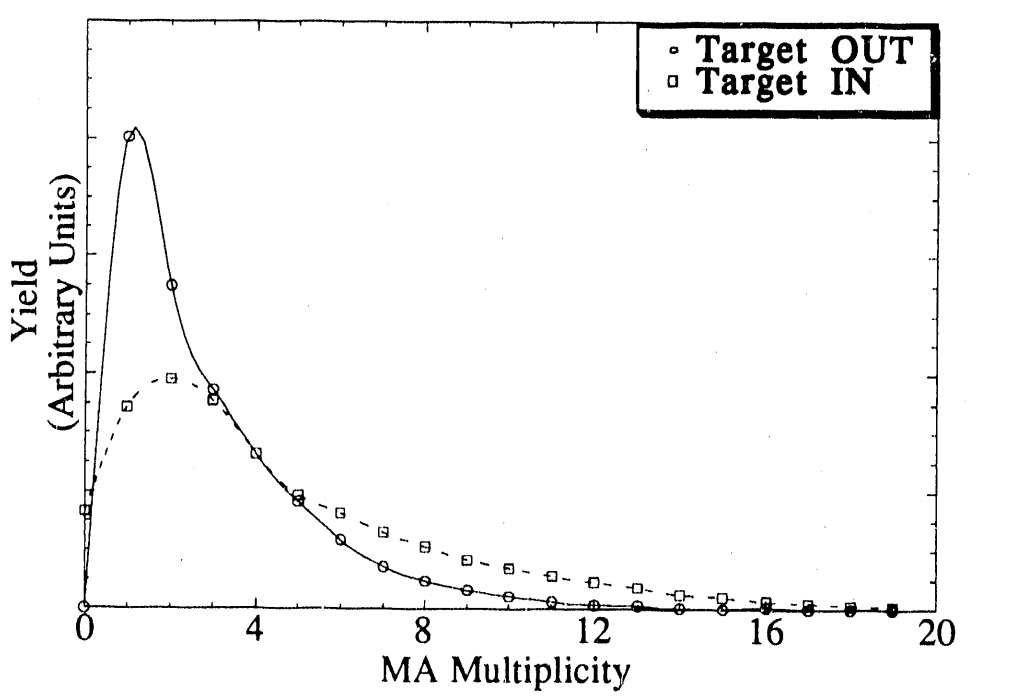

Figure 2-6
Multiplicity distributions for target out and target in data runs.

2.5. Prototype Drift Chamber

The drift chamber used in this experiment was developed and built by Kobayashi, Bieser, Symons, and Greiner[87Ko] as a prototype for the large (1.5 m × 2.0 m) drift chambers now used at HISS. A comprehensive discussion of the prototype drift chamber and it's operation can be found in Reference 87Ko. However, a brief description is presented here for completeness.

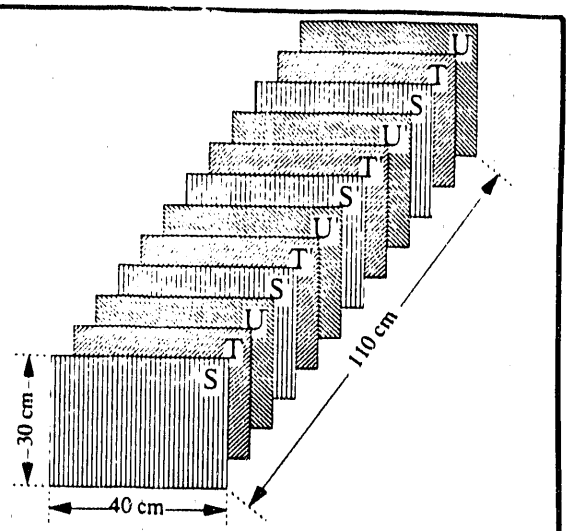

Figure 2-7
The pDC consists of twelve distributed planes of sense wires. The three orientations of wires are (S:0°, T:+60°, U:-60°). The primed planes are offset by 1 cm perpendicular to the wires.

The prototype drift chamber consists of 12 planes of wires. The planes are separated by 10 cm along the beam direction and are 40 cm wide by 30 cm high. Each plane has one of three wire orientations (0°, +60°, and -60° from vertical), and one of two wire offsets (0 cm, and +1 cm). The plane configuration of the detector is shown in Figure 2-7.

The sense wires are gold-coated tungsten 20 μm in diameter, and are separated within the plane by 2 cm. Each sense wire is surrounded by 75 μm Cu-Be field shaping wires as shown in Figure 2-8.

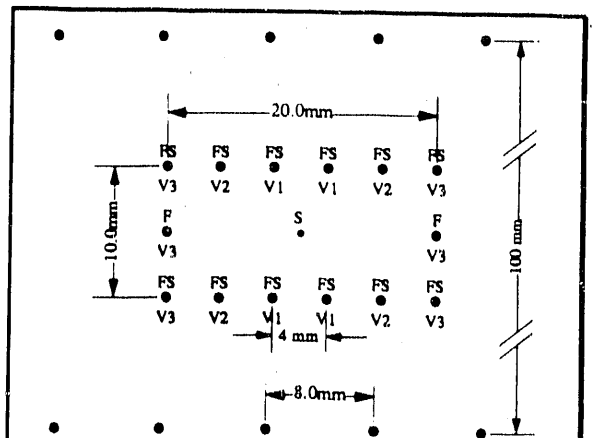

Figure 2-8
Wire positions of a single sense cell in the prototype drift chamber

Drift chambers are fairly common detectors in high-energy, elementary-particle physics experiments. Many references can be found on the subject . However, the signifi-

cantly larger charge of the fragments in RHI collisions requires some modification to conventional drift chamber design.

The most important additional consideration for the operation of drift chambers in RHI experiments is the high frequency of of δ-ray production by heavy-ions. When a RHI transverses the detector gas, it will often strike electrons in the medium with very small impact parameter producing energetic, knock-on electrons (called δ-rays) that have an appreciable range in the gas of a drift chamber causing spurious signals (and in some cases spurious tracks)(77Sa).

The maximum energy that a RHI (assumed as a point charge) of velocity β_i can impart to an electron knocked out of the detector gas is :

$$T_{max} = \frac{2 \cdot m_e \cdot \beta_i^2 \cdot \gamma_i^2 \cdot c^2}{1 + 2 \cdot \gamma_i \cdot \left(\frac{m_e}{M_i}\right) + \left(\frac{m_e}{M_i}\right)^2} \qquad \textbf{Equ. 2.5.1}$$

where m_e is the mass of the electron and M_i is the mass of the ion. The number of knock-on electrons of kinetic energy T produced per unit length x is:

$$\frac{d^2N}{dTdx} = \frac{1}{2} \cdot D \cdot \left(\frac{Z_m}{A_m}\right) \left(\frac{Z_i}{\beta_i}\right)^2 \cdot \rho_m \cdot \frac{F}{T^2} \qquad \textbf{Equ. 2.5.2}$$

where $D = 4\pi N_A r_e^2 m_e c^2 = 0.3070$ MeV·cm^2/g is a constant, Z_m and A_m are the charge and mass numbers of the detector medium, ρ_m is the detector medium density, and Z_i and β_i are the charge and velocity of the ion. F is a spin dependent factor which we can approximate by 1.0. Using Equations 2.5.1 and 2.5.2 we find that for a 1.65·A GeV ^{40}Ar, the number of δ-rays produced in 1 cm of Ar gas at STP with kinetic energy greater than T is:

$$N_\delta = 0.3995 \cdot \int_T^{T_{max}} (T^{-2}) dT = \left(\frac{0.3995}{T}\right) - 0.058 \qquad \textbf{Equ. 2.5.3}$$

where $T_{max} = 6.838$ MeV. Electrons with kinetic energy T = 114 keV have a range of 10 cm in Ar at STP. Thus, ≈ 35 δ-rays with range ≥10 cm (the distance between planes) are produced in every 10 cm of the drift chamber.

To address this problem, the drift chamber was constructed with the 12 planes distributed evenly along the depth of the detector, and the electronics for each wire contained ADC readout circuitry as well as the usual TDC electronics.

Reading out ADC information for each wire allowed us to more accurately determine the spatial position at a plane as measured by the TDC (see below on the ADC-TDC slew and space-time corrections). Also, using the ADC value as a first selection criteria helped simplify particle tracking through the drift chamber (see Section 3.1 on the tracking software).

Calibration

ADC-TDC Slew

The first calibration applied to the raw data from the drift chamber is what we have called the ADC-TDC Slew. The physical principle behind the need for this calibration arises from our use of constant-fraction discriminators (CFD) for the TDCs of the chamber. When a pulse reaches the drift chamber front end electronics, the constant fraction discriminator fires the TDC on 80% of the largest pulse height within the drift time window (see Figure 2-9). Since the rise time of the leading edge of the pulse depends on the amplitude of the signal, the drift time between the peak of the pulse (analogous to the real position of the particle track) and the leading edge of the pulse varies with ADC value.

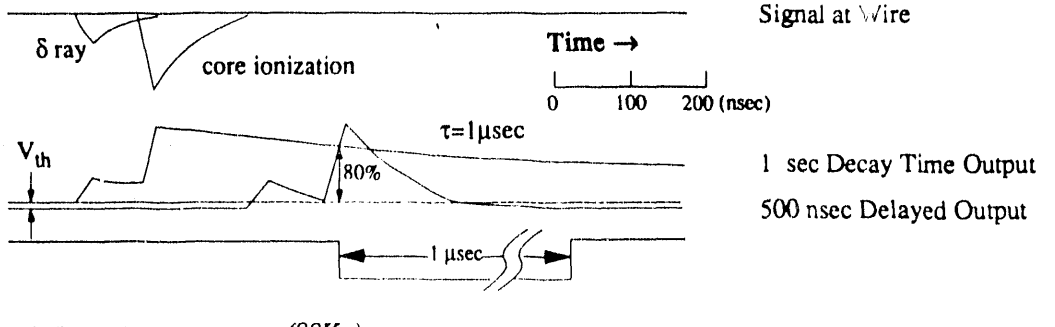

Figure 2-9 *Kobayashi et al (88Ko)*
Pulse shapes in drift chamber front end electronics.

Hence, larger pulses from tracks at a specified distance from a sense wire will trigger the CFD earlier. To correct for this slewing, we subtract the curve shown in Figure 2-10 from the raw drift chamber TDC channel. This correction gives us a TDC value (t') which reflects the position of the peak of the pulse rather than the position of the 80% leading edge (t' = t - SLEW(P); where P is the pulse height of the wire hit).

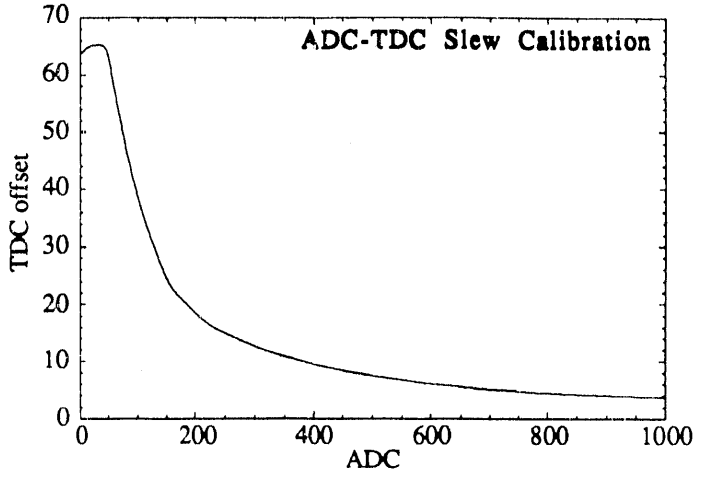

Figure 2-10
The ADC-TDC Slew correction for data from the pDC is subtracted from the TDC of each wire hit.

Space-Time Calibration

Once we have this slew corrected t', we need to convert this time measurement to a drift distance (l_d) from the sense wire, and then an absolute position within the chamber itself. If the average drift velocity in the detector gas is a constant regardless of the position within a drift cell of the particle track, then the conversion of t' to l_d would be a simple linear function. However, non-linear effects near both ends of the drift cell due to inhomogeneities in the drift field, cause some variation in the drift speed as a function of position within the cell.

To parameterize these variations, we use the 2 mm pitch MWPCs on either side of the pDC to reconstruct the particle track (with 1 mm resolution), and then use the projected intersection of that track with one s-plane to get a horizontal position (x_{wc}). When this x is plotted vs. the TDCs for that same s-plane, we see a saw-toothed pattern with maxima near sense wires and minima near field wires (Figure 2-11).

Fitting the mid-point of this correlation as a function of TDC, we can construct a Space-Time Curve (STC) for the chamber. This STC is then accessed in table format to calculate the drift distance for each wire hit recorded within the drift chamber. Though not expected beforehand, it was discovered empirically that the STC depends on the amplitude of the pulse (P). Hence the STC that is used for each hit depends on the ADC value of the hit (see Figure 2-12).

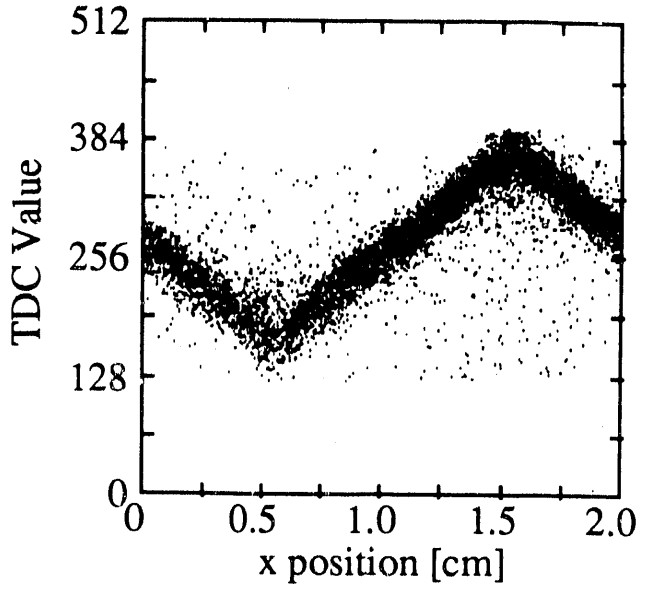

Figure 2-11
Plotting TDC value vs measured horizontal position for plane #5 in the pDC shows the shape of the relation between drift distance and drift time.

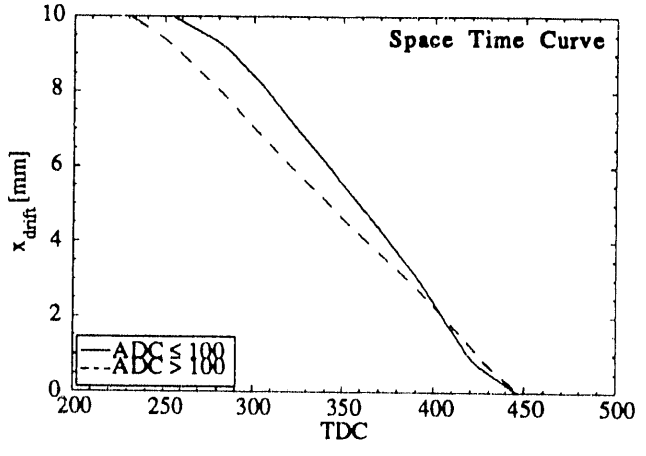

Figure 2-12
The Space-Time Curve (STC) for the pDC. The solid line is applied to hits with $ADC_{dc} \leq 100$, while the dashed line is applied for $ADC_{dc} > 100$.

2.6. Cerenkov Hodoscope

The least conventional detector in our system is the Velocity Measuring Device (VMD). Its design and construction were motivated by the inability of more conventional detectors to measure velocity with the resolution necessary for isotope identification of heavy ions in the 1-2·A GeV energy region. In fact, no other detector system in RHI experimentation has reached the velocity resolution in this mass and energy region that we have achieved in this experiment.

To identify isotopes in a mass spectrometer like HISS, requires measuring the charge (Z), the rigidity ($R \equiv p/Z$), and the velocity (β) of the particle and using the relation:

$$A = \frac{R \cdot Z}{\gamma \cdot \beta \cdot u} \qquad \textbf{Equ. 2.6.1}$$

where u = 931.5 MeV/c^2. The mass resolution for this measurement is given by:

$$\frac{\Delta A}{A} = \sqrt{\left(\frac{\Delta R}{R}\right)^2 + \left(\frac{\Delta Z}{Z}\right)^2 + \left(\gamma^2 \cdot \frac{\Delta \beta}{\beta}\right)^2} \qquad \textbf{Equ. 2.6.2}$$

For an Fe nucleus of energy E = 1.65·A GeV ($\gamma = 2.76$, $\beta = 0.932$), given a rigidity resolution of $\Delta R_{fwhm} = 0.5\%$; we would need a velocity resolution of $\Delta\beta_{fwhm} \leq 7 \times 10^{-4}$ to obtain a mass resolution of $\Delta A_{fwhm} \leq 0.3$ u.

Conventional Time Of Flight (TOF) methods involve measuring the time lag (Δt) between signals from two scintillators separated by linear distance Δl. The velocity is given by:

$$\beta = \frac{1}{c} \cdot \frac{\Delta l}{\Delta t} \qquad \textbf{Equ. 2.6.3}$$

Over a flight path of 8 meters, the timing resolution necessary for the above velocity resolution would be $\Delta t_{fwhm} < 20$ psec. The current TOF system at HISS has a resolution of $\Delta t_{fwhm} \approx 180$ psec. Even newer TOF technology such as planar spark counters do not provide high enough timing resolution[85Fu].

Other methods have been used to measure the velocity of relativistic charged particles including Cerenkov detectors operated at the velocity threshold for Cerenkov radiation production[88Ki,89Sh]. However, to operate such a detector at energies E ≥ 1.0·A GeV ($\gamma = 2.07$, $\beta = 0.876$) requires the use of material of refractive index $n \leq 1.14$. Such specialized materials (for example silica aerogel) have notoriously poor mechanical properties and are often plagued by density and refractive index inhomogeneities. Even if the mechanical problems surrounding such detectors at this energy are overcome, the resolution and dynamic range typically obtainable by such detectors is insufficient for clear isotope separation at our energies.

A technique which holds the promise of very good velocity resolution is Cerenkov Ring Imaging (CRI)(77SY). This method involves directly measuring the angle of emission of Cerenkov radiation by imaging the ring formed by the radiation on a position sensitive detector (such as a wire or drift chamber) as a charged particle passes through a Cerenkov radiator. Although the theoretical velocity resolution is more than sufficient for our requirements*, the pattern recognition aspect of the technique becomes quite complicated for multiparticle events. Although our experiment is an inclusive measurement, the VMD was designed to be used in exclusive experiments as well. An additional problem with CRI detectors is their technical complexity and expense.

Conventional methods of nuclear charge measurement usually involve measuring the rate of energy loss of a nucleus as it passes through detector material. Scintillator material attached to a PhotoMultiplier Tube (PMT) is the most common technique. However, the saturation of the signal from scintillators at high particle charge causes the scintillator response to deviate from the Z^2 response exhibited for low Z particles, thus reducing the absolute charge resolution of the device for large nuclei.

Recently, we have used a MUltiple Sampling Ionization Chamber (MUSIC) to measure the charge of relativistic heavy ions with a charge resolution of $\sigma_Z = 0.2$ e for fragments of 1.2·A GeV ^{139}La with $26 \leq Z_f \leq 56$(87Ch,88Br).

A method of using Cerenkov radiation to measure the velocity of relativistic charged particles has been suggested by J.V. Jelly(58Je) and used in experiment(81Sc,84Sy). The fact that the intensity of Cerenkov radiation remains proportional to Z^2, even for high charges, suggests the use of Cerenkov radiation for the measurement of fragment charge as well as fragment velocity.

---

* J. Seguinot predicts a possible velocity resolution of $\Delta\beta/\beta \approx 10^{-7}$ at $\gamma = 200$ based on theory. However, no experimental data at this resolution exists.

In order to overcome both the charge resolution and velocity resolution limitations of conventional scintillator-based detector systems, we built the Velocity Measuring Device (VMD) at HISS based on a detector design used for measurement of charge-changing reactions of secondary fragments[84Ol,84Sy,85Du]. The VMD is specifically designed to measure both the charge and the velocity of heavy ions ($Z \geq 6$) at high energies ($E/A \geq 1$ GeV). It's operation is based on the dual principles of Cerenkov radiation and Total Internal Reflection (TIR), and relies on the dispersion of dielectric materials such as glass and fused silica (quartz).

Shown in Figure 2-13 is a picture of the VMD showing the support structure, the cabling for signals and high-voltage, and the two walls of radiators used in our experiment. During operation, the front and back openings of the aluminum support structure seen in Figure 2-13 are covered by light tight windows of copper coated mylar.

Each wall of the VMD consists of 36 radiators and 36 photomultiplier tubes arranged in 4 rows (see Figure 2-14). Rows 1 and 3 are oriented with the PMT for each radiator on the bottom. Rows 2 and 4 have the opposite orientation. The position of the radiators within the 4 rows provides complete coverage of the 0.25×1.0 m aperture with sufficient overlap to eliminate gaps for particles with incident angles within the range of interest. Each radiator is 30 cm long, 0.5 cm thick and tapers from a width of 4.0 cm at the PMT to 3.0 cm at the opposite end (the quartz radiators taper from 4.4 cm to 3.0 cm) in order to facilitate light collection efficiency (see Figure 2-15). All radiators contained in the light-tight box are open to the same volume of air, but show no signs of optical cross talk between radiators.

The upstream wall of radiators is composed of fused SiO and provides the velocity sensitive measurement for the projectile fragment; while the downstream wall is composed of UBK7 glass and measures the charge of the projectile fragment.

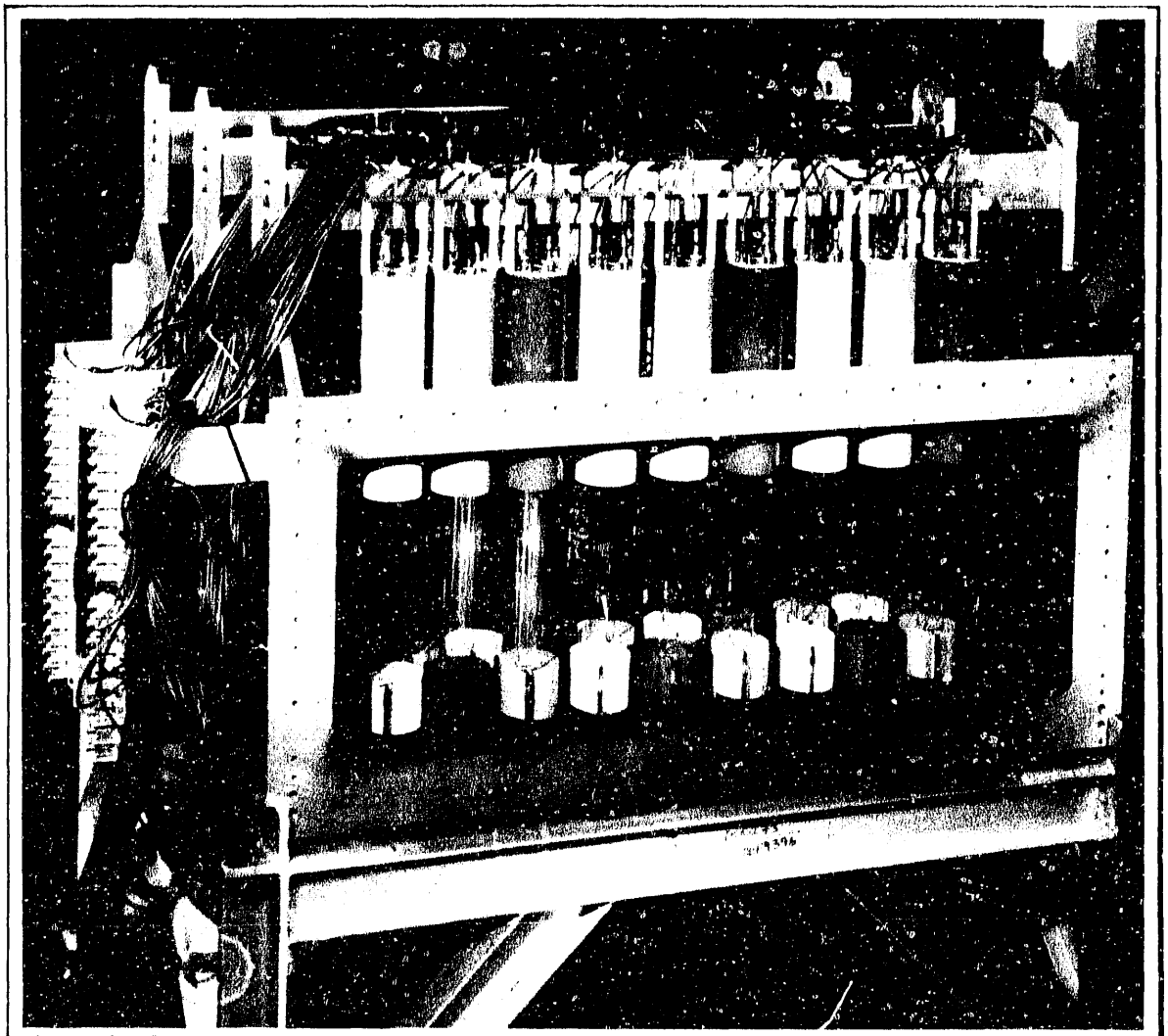

Figure 2-13 BBC 855-4206
Photo of the VMD support structure showing the arrangement of the phototubes and signal and high voltage cables..

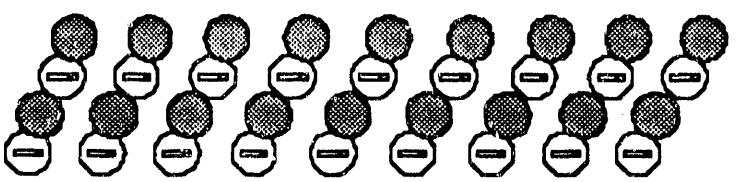

Figure 2-14 a)
Top View of VMD radiators showing the staggered arrangement of radiators in the VMD which provides complete coverage for particles within the angular range of interest.

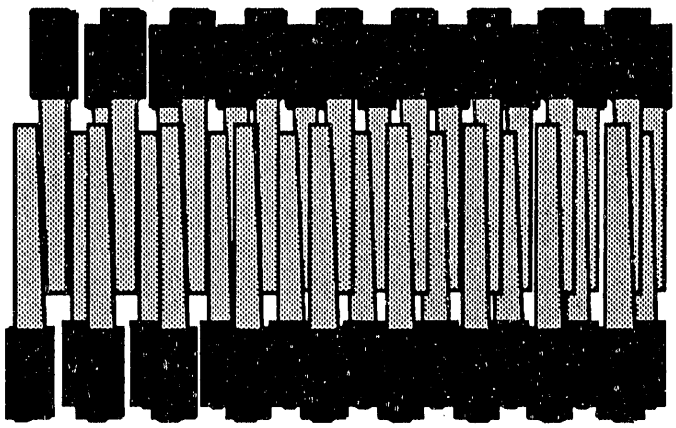

Figure 2-14 b)
Front View of VMD radiators showing the arrangement of radiators in the VMD. (Apparent gaps in the radiator array are an artifact of the artist's rendition.)

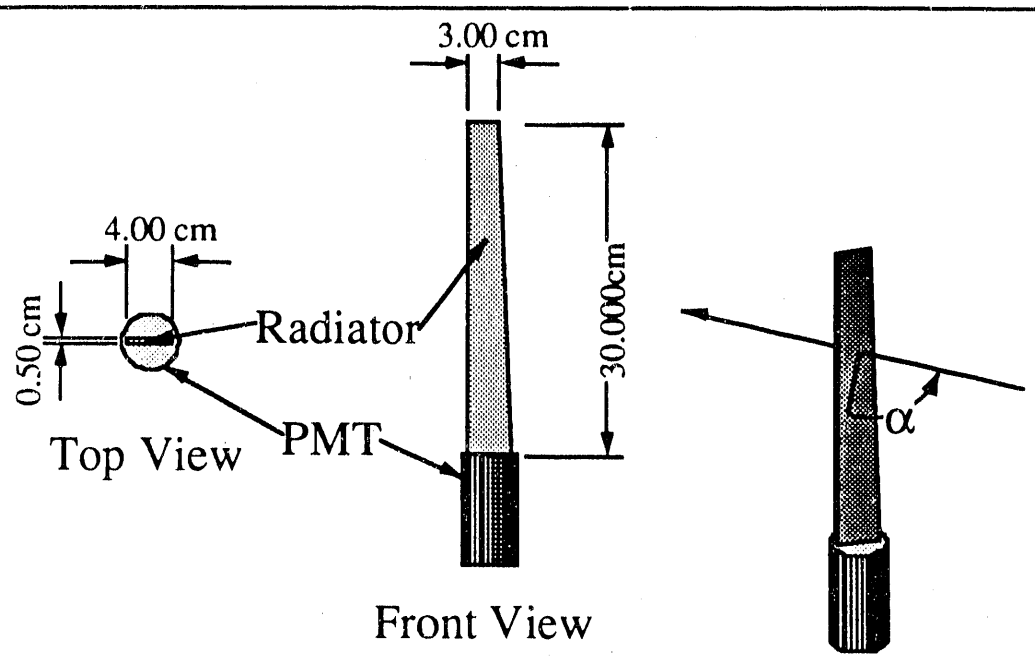

Figure 2-15
Diagram of a single VMD radiator and photomultiplier tube. Each radiator is 30 cm long and 0.5 cm thick. The glass radiators taper in width from 4 cm at the PMT to 3 cm at the opposite end (the quartz radiators taper from 4.4 cm to 3 cm).

Principle of Operation

The basic principle of the VMD is illustrated in Figure 2-16. A charged particle passes through a VMD radiator normal to the large flat surface of the radiator. If the velocity of the particle is greater than the critical velocity for Cerenkov radiation in the material ($\beta \geq \beta_{crit} = 1/n$), the particle will emit Cerenkov light with an opening angle of:

$$\theta_c = \cos^{-1}\left(\frac{1}{\beta \cdot n}\right) \qquad \textbf{Equ. 2.6.4}$$

with an intensity distribution of:

$$\frac{dI}{d\lambda} = I_0 \cdot \left(\frac{Z}{\lambda}\right)^2 \cdot \sin^2(\theta_c) \qquad \textbf{Equ. 2.6.5}$$

The angle at which total internal reflection of light occurs in a dielectric material of refractive index *n* is:

$$\theta_{tir} = \sin^{-1}\left(\frac{1}{n}\right) \qquad \textbf{Equ. 2.6.6}$$

If the velocity of the particle is high enough, the angle of total internal reflection and the opening angle of Cerenkov radiation are matched ($\theta_c \geq \theta_{tir}$) such that the Cerenkov light is trapped within the radiator by TIR and can be detected by a phototube at its end. However, because real dielectric materials have an index of refraction that varies with the wavelength of the incident light ($n = n(\lambda)$), the velocity where $\theta_c = \theta_{tir}$ depends on the radiation wavelength.

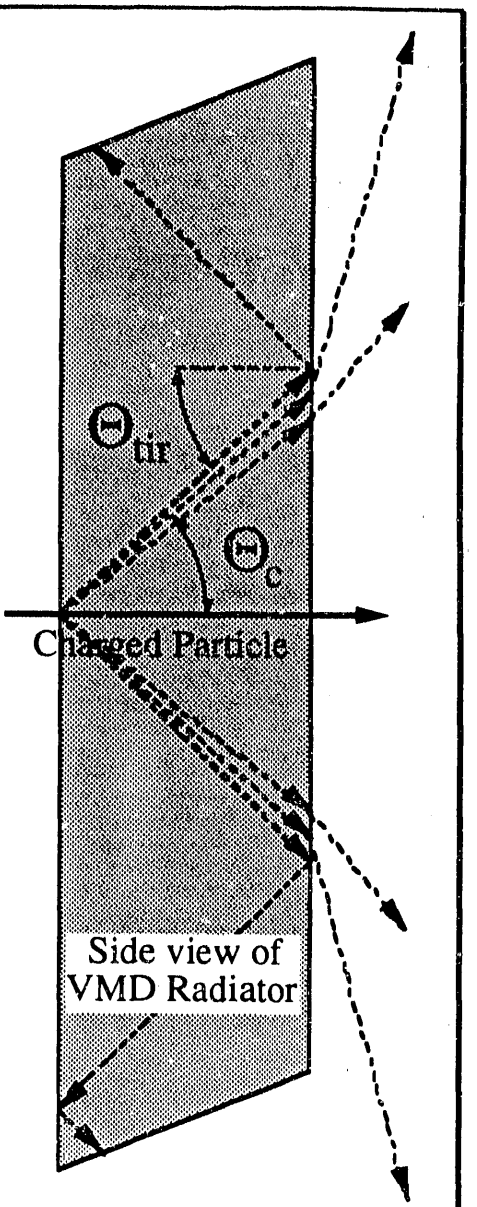

Figure 2-16
Cross sectional view of the production and total internal reflection of Cerenkov radiation in a VMD radiator.

If we define β_s as the velocity at which $\theta_c = \theta_{tir}$ (for $n=\langle n(\lambda)\rangle$), we see that:

$$\beta_s = \frac{1}{\sqrt{n^2 - 1}} \qquad \textbf{Equ. 2.6.7}$$

Because of the dispersion of the dielectric medium, there is a range of β about β_s where some wavelengths of Cerenkov radiation are trapped within the radiator by TIR, and some escape. Furthermore, the proportion of trapped light changes rapidly with changing β and follows the curves shown in Figure 2-17. This steep dependence of the PMT response on particle velocity is the basis for the velocity sensitive operation of the VMD. For radiators made of quartz ($n_q = 1.47$) $\beta_s = 0.93$ which suggests that quartz radiators can be used to measure the velocity of projectile fragments at $E_s = 1.6 \cdot A$ GeV. For UBK7 glass radiators ($n_g = 1.53$) $\beta_s = 0.86$ or, equivalently, $E_s = 0.89 \cdot A$ GeV.

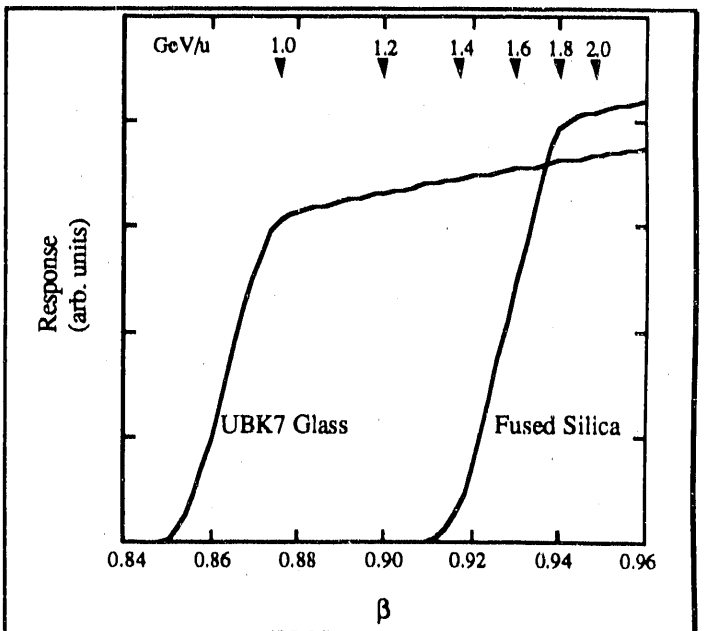

Figure 2-17 *Olson (89Ol)*
Velocity response of the two radiator materials (UBK7 glass, and fused silica) used in the VMD.

Practical Considerations of Operation

Although the final resolution of the VMD was quite good ($\Delta Z_{fwhm} = 0.19$ e, and $\Delta\beta_{fwhm} = 5 \times 10^{-4}$), there are a number of considerations which complicate the operation of detectors using the above described principles.

Because the velocity dependence of the radiator response arises from the precise matching of two angles (θ_c and θ_{tir}), changes in the incident angle (α in Figure 2-15) of charged particles hitting the radiator can wash out any velocity sensitivity. Figure 2-18 shows the effect of particle incident angle on radiator response for different particle velocities.

To ensure that the incident angles of the projectile fragments were all approximately normal to the radiator face, we used a He-Ne laser on a rotating turntable at the center of the HISS dipole magnet gap to adjust both the vertical and horizontal angles of each radiator in the array.

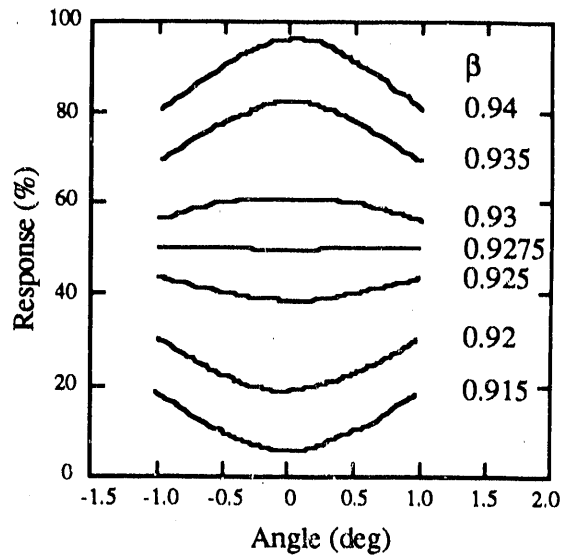

Figure 2-18 *Dufour et al (85Du)* Angular response of the VMD.

Another consideration in using the VMD is the non-negligible thickness of the detector. Each radiator contributes approximately 1.1 g/cm^2 of SiO to the path of a particle being measured. This means that for an ^{40}Ar nucleus a single VMD radiator is approximately a 6.0% interaction target. Because each projectile fragment passes through 2-4 radiators while traversing the VMD, this is an important concern.

In order to minimize contamination of the data by interactions in the radiators we put the VMD at the end of the downstream detection system. Also we were able to use the fragment charge as measured upstream and downstream of the quartz radiators to eliminate interactions in them (see Section 3.3).

Calibration

A final consideration in using the VMD is the calibration of the detector. Because of imperfections in and variations between individual radiators, the calibration of the VMD involves parameterizing each radiator separately; a process which proved to be more difficult than originally anticipated.

Imperfections in the radiators include failure to meet stringent requirements on the precision of the radiator geometry, and/or inhomogeneity in the radiator material. Either of

these factors will cause the radiator response to deviate from the expected, ideal response described above.

VMD-Glass Wall

The second set of radiators in the VMD, composed of UBK7 glass ($n_g = 1.53$), has a velocity dependence well below the energy of the beam used in the experiment ($0.865 = \beta_s << \beta_b = 0.93$; see Figure 2-17). This means that the response of a single radiator should be proportional to the square of the charge of the particle passing through the material and independent of the particle velocity (assuming $\beta_{pf} \approx \beta_b$).

Vertical Position Correction

The PMT response (P_g) to Cerenkov radiation from a charged particle with $\beta \approx 0.93$ passing through an ideal glass radiator depends only on the charge of the particle ($P_g \propto Z^2$). However, the glass radiators used in the VMD have imperfections that alter the response of the PMT to light produced in the radiator from the expected response of theory. Light absorption in the radiator material, and reflection losses during total internal reflection cause position dependence of the pulse height as measured by a PMT at one end of the radiator.

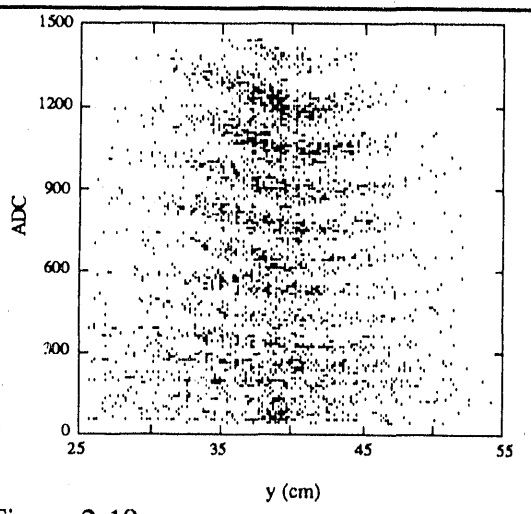

Figure 2-19
ADC channel vs vertical position for glass radiator #G14.

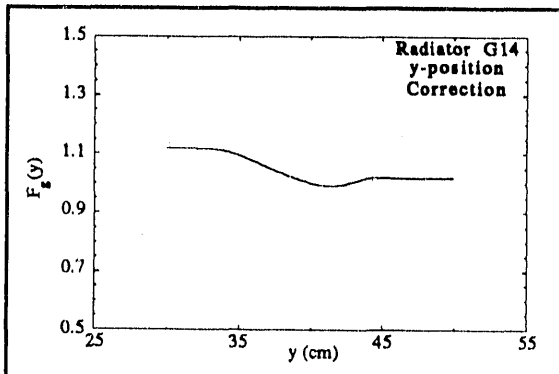

Figure 2-20
Vertical position correction factor for glass radiator #G14.

Figure 2-19 shows the pulse height (P_g) of glass radiator G14 plotted vs. the vertical position of the particle track at the radiator (as projected from the drift chamber). Using this vertical position, we can determine the mean of the P_g distribution as a function of y for a single fragment charge and construct a normalization function $F_g(y)$ (see Figure 2-20).

Dividing the radiator pulse height by the normalization function removes the vertical position dependence of the signal ($P'_g = P_g/F_g(y)$). The charge resolution before and after the $F_g(y)$ correction for radiator G14 is shown in Figure 2-21.

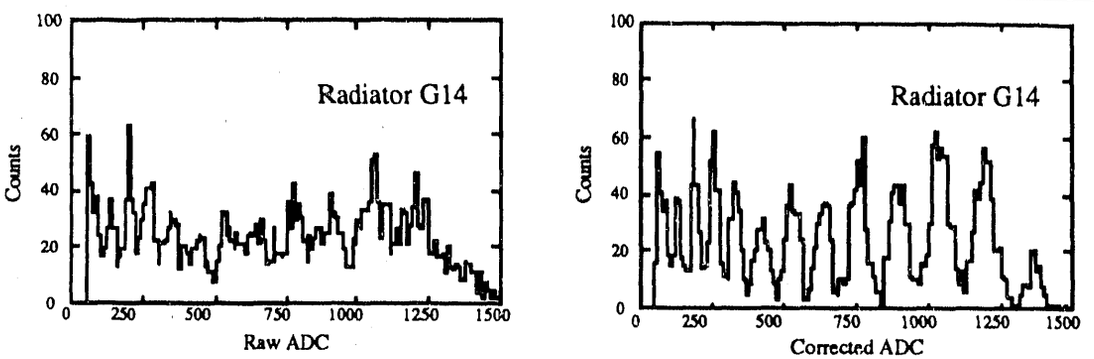

Figure 2-21
Histogram of a) raw and b) y-position corrected ADC channel for glass radiator #G14.

ADC to Z Interpolation

Once we have the position corrected P'_g of Figure 2-21b, we can count down from the beam charge and construct a look up table of P'_g value vs. Z^2 for each glass radiator. Because the position corrected response of all the radiators are proportional to the fragment charge ($P'_g = K \cdot Z^2$), linear interpolation between the points of the look up table provides an excellent calculation of fragment charge.

Once the fragment charge has been calculated, successive comparisons between radiators ensures that the count-down procedure correctly identified the charge (especially in radiators far from the beam position). When an inconsistency between radiators is found, charge values for the radiator deemed unreliable (usually the radiator farther from the beam position) are shifted.

Combining all the radiators into one histogram of projectile fragment charge (Figure 2-22) we see that the charge resolution of the glass wall of the VMD is $\sigma_Z = 0.18$ e for Si (the resolution is a constant $\sigma_Z = 0.194 \pm .006$ e for $Z_f = [5, 18]$).

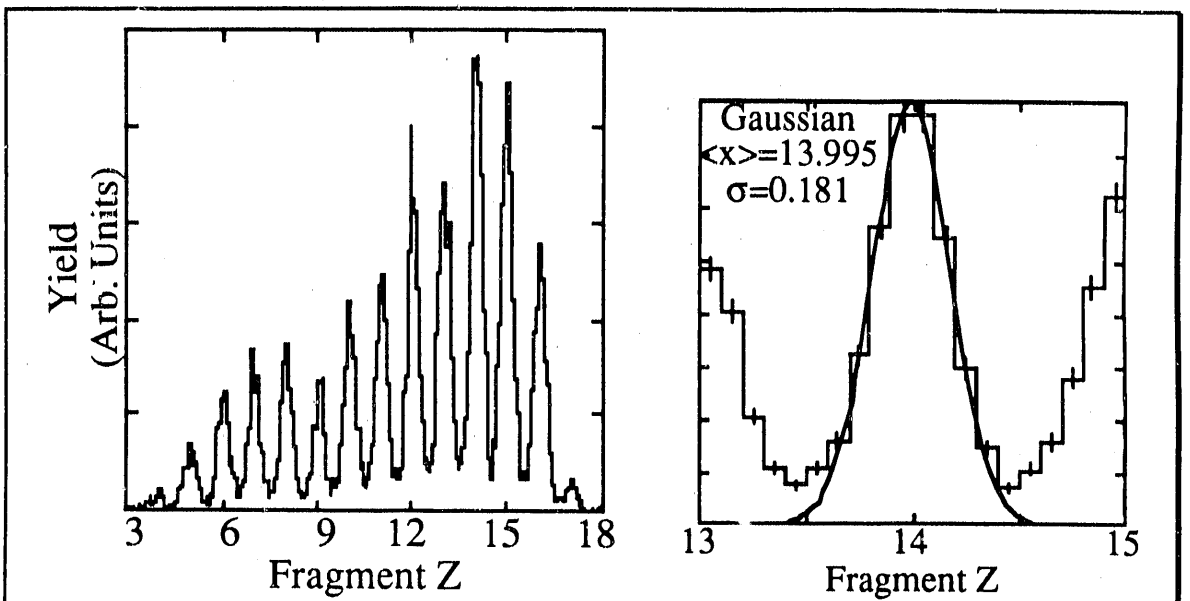

Figure 2-22
a)The charge resolution of all the glass radiators together (after calibration) is of $\sigma_Z \approx 0.2$ e.
b)The width of the charge peak for silicon is $\sigma_Z = 0.18$ e.

VMD-Quartz Wall

The quartz radiators in the VMD were chosen because their refractive index (n_q = 1.47) provides velocity sensitivity of the radiators at an energy of $E_s \approx 1.65 \cdot A$ GeV. Because the intensity of the Cerenkov radiation produced is proportional to Z^2 (see Equation 2.6.5), we expect the response of a quartz VMD radiator to show the same dependence on the charge of the projectile fragment. In addition to this Z^2 dependence, we have seen that the dependence of the PMT response to a fragment of $E_f \approx 1.65 \cdot A$ GeV is linearly proportional to the fragment's velocity (see Figure 2-17). Therefore, the ADC value measured by experiment should be proportional to both the square of the fragment charge and to the fragment velocity ($P_q \propto \beta_f \cdot Z_f^2$).

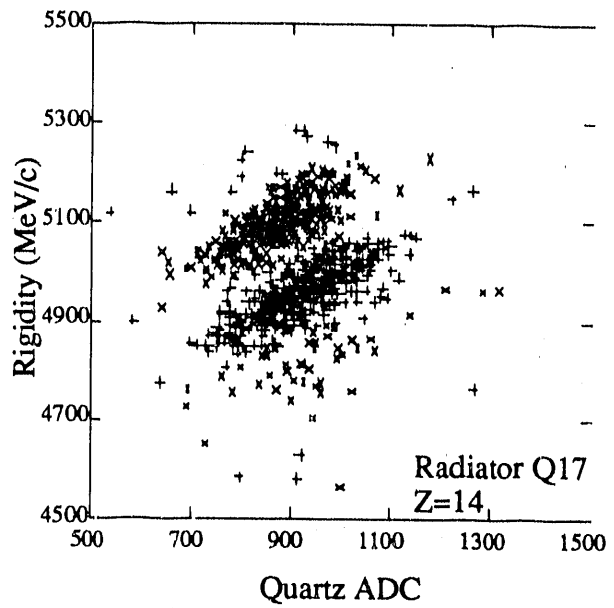

Figure 2-23
Scatter plot of rigidity vs ADC channel for charge 14 particles hitting quartz radiator #Q17. To guide the eye, the even numbered masses are denoted by x's, while the odd numbered masses are denoted by +'s.

When the PMT pulse height of a quartz radiator (P_q) is plotted vs the fragment rigidity (R_f) as measured with the spectrometer and drift chambers for a single element, the different isotopes appear as linear clusters of points with a slope dependent on the rigidity (see Figure 2-23).

To calculate the fragment mass from such a plot, let us first define the variable:

$$A_0 \equiv \left(\frac{Z_f \cdot R_f}{\gamma_b \cdot \beta_b \cdot u}\right) \qquad \textbf{Equ. 2.6.8}$$

where $\gamma_b = 2.76$, $\beta_b = 0.932$, and $u = 931.5$ MeV/c^2. This variable (A_0) is the mass calculated as if the projectile fragment had exactly the same velocity as the beam (β_b). Because projectile fragments have a spread in velocity, the variable A_0 shows a linear dependence on $P'_q = P_q/Z_f^2$ with a slope that scales with A_0 (for a single value of P'_q). Parameterizing this dependence and using a similar count down method to the one used for the charge (see above), we are able to calculate a fragment mass (A_1).

Although the variable A_1 exhibits the mass resolution of the system, one final step is taken in the calculation of the true fragment mass. This step is simply to smoothly transform the A_1 variable to guarantee that the peaks fall on integer values. This requires moving most peaks less than 0.1 u.

Combining all the quartz radiators (Figure 2-24) we see that the mass resolution of the system for ^{30}Si is $\sigma_A = 0.19$ u ($\sigma_A = 0.237 \pm 0.025$ for $A_f = [10, 40]$), which corresponds to a velocity resolution of $\Delta\beta = 2.3 \times 10^{-3}$ with a rigidity resolution of 10^{-3}.

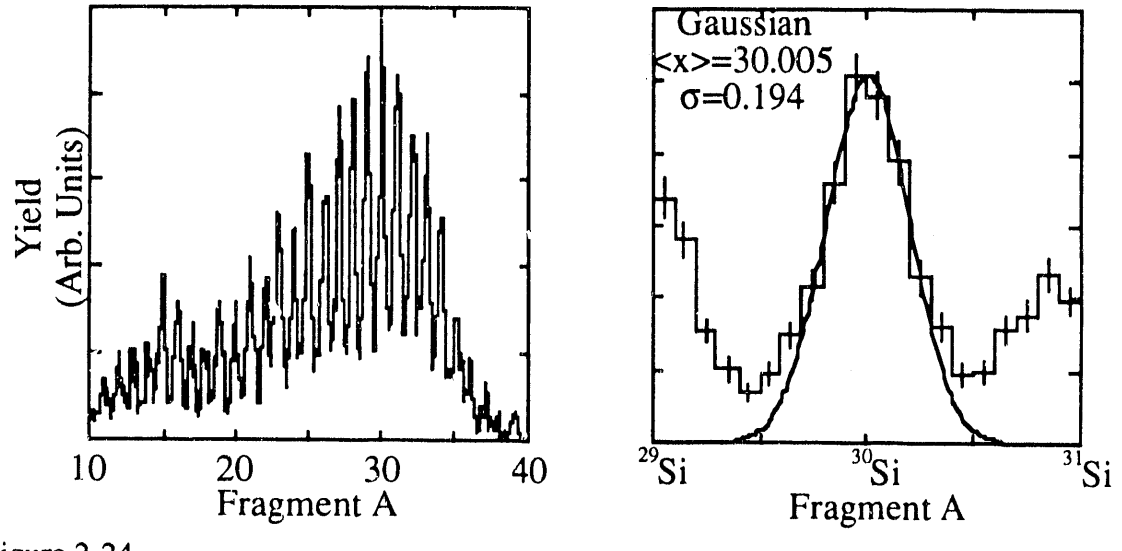

Figure 2-24
a)The mass resolution of the system is $\sigma_A \approx 0.2$ u.
b)The width of the mass peak for ^{30}Si is $\sigma_A = 0.19$ u.

If the charge calculated with the glass VMD radiators is plotted vs the mass calculated using the rigidity and quartz radiators, separate isotopes are clearly distinguishable (see Figure 2-25).

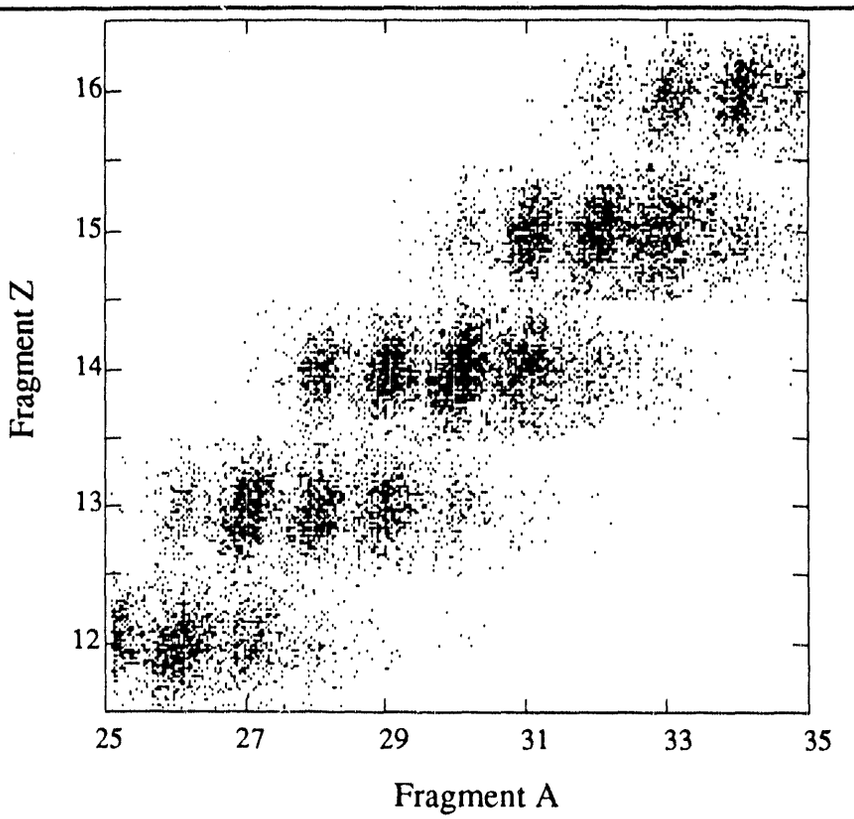

Figure 2-25
Plot of fragment charge vs mass for $12 \leq Z_f \leq 16$ and $25 \leq A_f \leq 35$ showing the separation of individual isotopes.

3. Data Reduction

Our analysis was performed on DEC mainframes and workstations with the VAX architecture. For most of the analysis, we used the computer analysis shell program LULU[(83Cr)]. LULU was originally written in FORTRAN by H.Crawford and P.Lindstrom and has become the de facto standard for data analysis at the HISS facility.

LULU is an analysis shell into which users may insert their own FORTRAN modules. Sets of modules may be grouped together as a unit called an analyzer. Each analyzer is called sequentially by LULU for each event, acting on the raw data stream or on the

output of previous analyzers. LULU provides raw event handling, graphics, statistical analysis, and the capability of saving and restoring raw or processed data at almost any stage of the analysis. LULU also provides the ability to easily apply and change cuts on the entire event, or for individual structures within the event called word groups.

Data reduction consisted of the following steps:

1 Raw Data Decoding
2 Detector Calibration
3 Track Recognition (pDC)
4 Charge Calculation
5 Momentum Reconstruction
6 Mass Calculation
7 Cut Application
8 Background Subtraction
9 Physics Extraction

Each of the above steps is accomplished by calling one LULU analyzer, or a sequence of analyzers (Each analyzer operating on the output of all the previous analyzers.).

Step 1 involves extracting from the data stream the data associated with each detector and decoding the raw data into a form suitable for calibration and for further analysis. The output of this step includes: a) Central wire number and number of wires for each plane of the wire chambers, b) Phototube ID and TDC from the multiplicity array, c) Wire ID, ADC, and TDC from all wire hits in the drift chamber, d) Two ADC values from the S3 beam veto scintillator, and e) Phototube ID and ADC from each radiator which fires in the two walls of the VMD.

In Step 2 we calibrate the detectors and convert the raw data into physical quantities, including: a) position and vector at the target from the upstream MWPCs, b) mid-rapidity multiplicity (cut on TDC value) from the multiplicity array, c) drift distance of each wire hit in the drift chamber, and d) fragment charge from the S3 beam veto scintillator.

Step 3 involves applying a pattern recognition algorithm to the wire hits in the drift chamber to recognize and reconstruct the real particle tracks in the detector and to eliminate noise and spurious hits (see Section 3.1). At this stage, we also match each drift chamber particle track with its associated VMD radiators.

In Step 4, we use the ADC values from the glass wall of the VMD and the projected particle track to calculate the fragment charge (see Section 2.6).

In Step 5, we reconstruct the vector rigidity ($\vec{R} = \vec{p}/Z$) of the particle by a method based on Chebychev polynomials, using the upstream position at the target given by the upstream wire chambers, and the downstream track measured by the drift chamber (see Section 3.2)

Step 6 follows the procedure outlined in Section 2.6 for calculation of the particle mass using the rigidity calculated in Step 5, the charge as calculated in Step 4, and the ADC values from the quartz wall of the VMD.

3.1. Drift Chamber Tracking Algorithm

The tracking algorithm used for the drift chamber data was originally written by T.J.M.Symons, and has been modified by T.Kobayashi. A later version of the same code (modified by D.Olson and W.Christie) is used for pattern recognition in the new 1.5×2.0 m drift chambers. For a detailed treatment of the current tracking algorithm, the reader is referred to W.B.Christie's Ph.D. thesis[90Ch].

Although great care was taken in the construction of the drift chamber, the mechanical placement of the 12 wire planes in the chamber must be measured empirically by iterative runs of the track finding code and comparisons of the calculated track position, and the wire hit drift distance. Once this is accomplished, each wire hit can be assigned two absolute positions within the drift chamber reference frame (two positions because of left-right ambiguity). For our experiment, only those wires registering both a valid ADC value and TDC value were input to the tracking algorithm.

In the first step of the program, only the s-planes (i.e. 0° wires measuring horizontal position) are considered. Using a hard-wired searching order, the tracking software constructs all s-plane track candidates that meet pre-defined values of χ^2, number of planes used in the track, and maximum incident track angle. Once an s-candidate is found that sat-

isfies these criteria, the wires constituting the track are removed from consideration for subsequent tracks. This produces a set of vertical planes through the drift chamber, each plane defined by a position and angle relative to the front plane of the chamber (x and θ_x).

Determining the vertical position of each diagonal wire (from t and u planes) as projected onto the s-candidate plane (and constrained by the physical dimensions of the chamber), the tracking software then executes another two-dimensional line recognition step, associating a vertical position and angle (y and θ_y) relative to the front plane of the chamber with each horizontal s-candidate projection.

Using the (x, θ_x, y, θ_y) for each track candidate, the three-dimensional χ^2 is calculated for each three-dimensional track. After elimination of unsatisfactory track candidates, the final particle tracks are projected to the VMD and matched with glass and quartz radiators present in the event.

3.2. Chebychev Momentum Reconstruction

The three-momentum of the projectile fragment (or beam nucleus) detected downstream in the pDC is reconstructed using software written for use in analysis of HISS experiments by D.L. Olson[86Ol]. The underlying basis for the momentum reconstruction is the following.

For a known magnetic field, the trajectory of a charged particle passing through the field is completely determined once three points on the trajectory (at least one on either side of the field) are known. For our experiment, these three points are the position at the target as measured by the USWCs (x_T, y_T), and the downstream vector as measured by the pDC (x, θ_x, y, θ_y). Since the HISS field is axially symmetric, the three points contain redundant information. In particular, the vertical projection of the particle trajectory through the HISS dipole is uniquely determined by two vertical positions, or one vertical angle. Since we measure the vertical position upstream and downstream of the magnet, as well as the angle

downstream, we are able to use the redundant information to eliminate bad events (NB This is the basis of the ΔY cut of Section 3.3.).

The magnetic field of the HISS dipole has been mapped in 3-dimensions for several current settings using a triaxial Hall probe mounted on a rigid frame driven by step motors. The magnetic field setting used in our experiment was the 16 kGauss field (1225 Amps of current in the HISS superconducting coils).

Given the three points (six coordinates) needed to define the trajectory, any variable associated with the trajectory (e.g. R_x, R_y, R_z, path-length, scattering angle) can be expressed as an expansion in some set of orthogonal functions of the six coordinates. As with most such expansions, the accuracy obtainable is dependent on the number of terms in the expansion.

Because we are limited by computer power, we do not do an event-by-event integration of the particle trajectories through the known (mapped) magnetic field. For the same reason, we want to use a set of orthogonal functions which minimizes the amount of calculation involved in determining the expansion coefficients.

The characteristic of Chebychev polynomials that make them attractive in this respect is that the n coefficients for the n^{th} order expansion can immediately be used as the first n coefficients for the m^{th} order expansion, where $m > n$. Thus, if the accuracy of the n^{th} order Chebychev expansion is insufficient for calculating particle trajectories, we can increase the number of terms in the expansion without recalculating coefficients for the n terms already used.

For a detailed treatment of the general approach outlined here, or of the method particular to HISS experiments, the reader is referred to References 69Le (general) and 86Ol (HISS).

3.3. Background Corrections

Because of the large amount of material in the beam path other than the target (see Table II) background corrections are very important in extracting physical quantities.

Two classes of background corrections can be applied to the data. In the first method, the quality of the data is evaluated on an event-by-event basis by examination and cuts on single-event parameters that are sensitive to background contamination. In the second method, background contamination of the data is removed by the subtraction of normalized data taken with the target removed from the beam line (target out data). In our experiment, we have carried out both types of background corrections to calculate cross sections, and to extract momentum distributions.

Reaction Rates

The interaction rate in the target can be easily calculated from the target in and target out rates. The measured reaction rate for a run is the ratio of the INT and BEAM trigger scalars (NB These scalars are present regardless of the trigger level actually used for a run. See Section 2.2). The reaction rate for target out is $R_{OUT} = 4.1\% \pm 0.01\%$. For the carbon target the target in reaction rate is $R_{IN(C)} = 7.4\% \pm 0.02\%$, which yields a reaction rate in the carbon target of $R_C = 3.4\% \pm 0.01\%$. The same numbers for the KCl target are $R_{IN(KCl)} = 5.2\% \pm 0.01$ and $R_{KCl} = 1.1\% \pm 0.003\%$. These numbers stress again how important the background correction is in this experiment.

Reaction Regions

Considering Figure 2-1, we see that the material in the path of the beam and fragments can be divided into three distinct regions, each of which effects the data in a different way. Our event-by-event background correction cuts are based on the individual signatures of these regions. Region 1 consists of all the material upstream of the target. Region 2 is defined as the material downstream of the target but upstream of trigger scintillator S3.

Region 3 is defined as the remainder of the material up to and including the second wall of the VMD hodoscope.

Region 1: Beam Focus Cut

Beam particles that react in region 1 will produce beam particles (elastic collisions) or fragments (inelastic collisions) incident on the target with an angle determined by the beam focus convoluted with the scattering angle of the reaction. The beam scintillator S2 eliminates most particles with charge $Z < 18$. However, many scattered beam and fragment nuclei that make it past S2 can be rejected because they will be scattered out of the phase space envelope of the beam as measured by the UpStream Wire Chambers (USWCs).

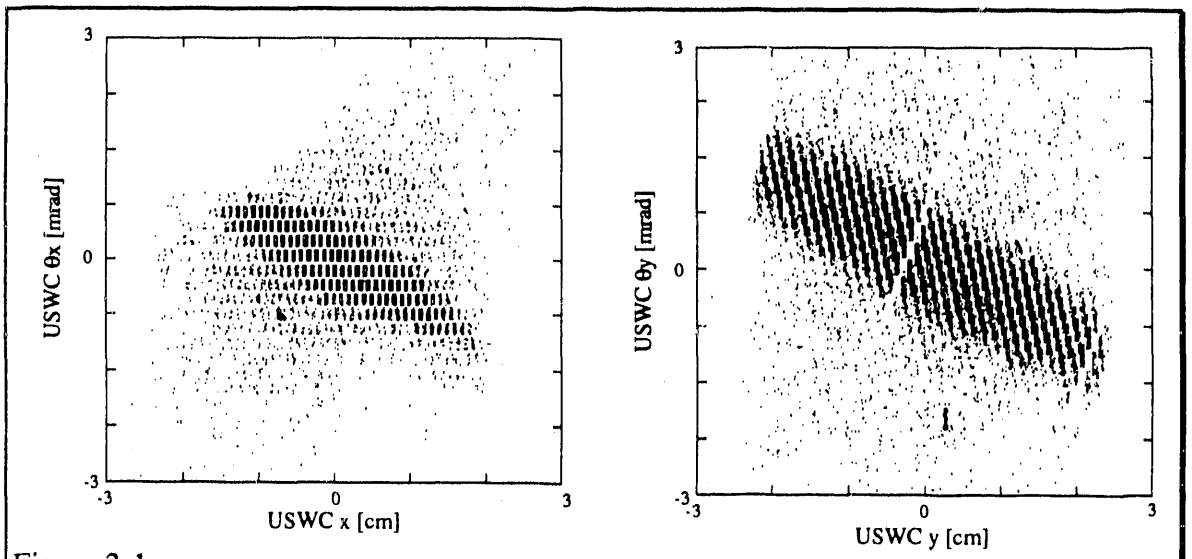

Figure 3-1
Scatter plot of angle vs position at the target as measured by the upstream wire chambers in a) the horizontal ($\hat{x}$) direction, and b) the vertical ($\hat{y}$) direction.

This is illustrated in Figure 3-1 which shows the correlation between beam position and angle in the vertical and horizontal directions. In order to eliminate particles outside of the beam phase space envelope, we first project the x and y components of each beam track to their respective focal planes (x_v, and y_v). We then construct the variable:

$$r_{foc} = \sqrt{\left(\frac{(x_v - x_0)}{\sigma_x}\right)^2 + \left(\frac{(y_v - y_0)}{\sigma_y}\right)^2} \qquad \text{Equ. 3.3.1}$$

where the mean position of the beam and the width of the beam at the virtual focus are (x_0, y_0) and (σ_x, σ_y) respectively. This normalized, positive-definite variable (see Figure 3-2) can be interpreted as the radial distance from the center of the virtual focus of the beam in units of the beam size (We call it a virtual focus here because the focal lengths for the beam in the $\hat{x}$ and $\hat{y}$ directions are different).

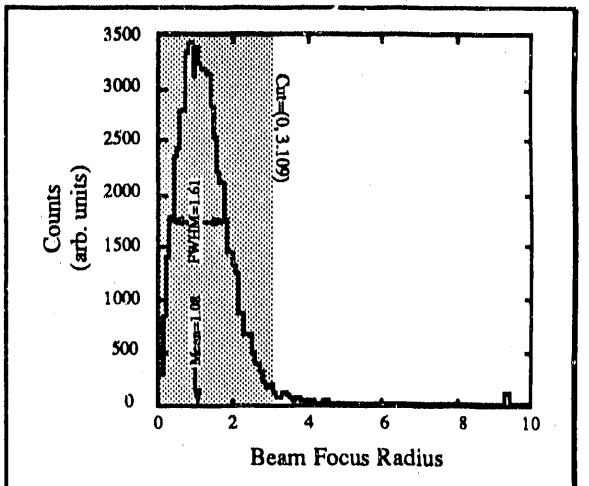

Figure 3-2
Histogram of the r_{foc} variable showing the limits for the software r_{foc} cut.

To cut out particles which clearly lie outside the beam focus, we have required that the beam particle satisfy $r_{foc} = [0, 3.11]$. This eliminates 6.0% of target in events and removes the long flat tail of the r_{foc} distribution. This long flat tail is believed to represent scattering upstream of WC2 and beam halo (particles at the periphery of the beam envelope) that are not eliminated from the trigger by the S2 and V2 trigger scintillators.

Region 2: Target-y Cut

Region 2 is defined as the material downstream of the target, yet upstream of the beam veto scintillator S3. If a nucleus interacts in this region, resulting in a change of the fragment's vector momentum, the assumptions underlying the momentum reconstruction are obviously invalid (i.e. The trajectory of the particle through the magnetic field of the dipole is no longer fully constrained by a position at the target and a vector at the drift chamber.).

However, if a particle traverses this material without interaction, the upstream and downstream trajectories must project to the same vertical position at the target. This can be used to reject many of the interactions which, because they scatter through a finite angle, do not project back to the point that the beam particle hits the target.

The variable we use to tag interactions in Region 2 is:

$$\Delta Y \equiv Y_p - Y_f \qquad \textbf{Equ. 3.3.2}$$

where Y_p and Y_f are the vertical positions at the target of the beam particle (Y_p) as measured by the upstream vectoring detectors (WC1 & WC2) and of the projectile fragment (Y_f) as projected by the downstream vectoring detector (pDC).

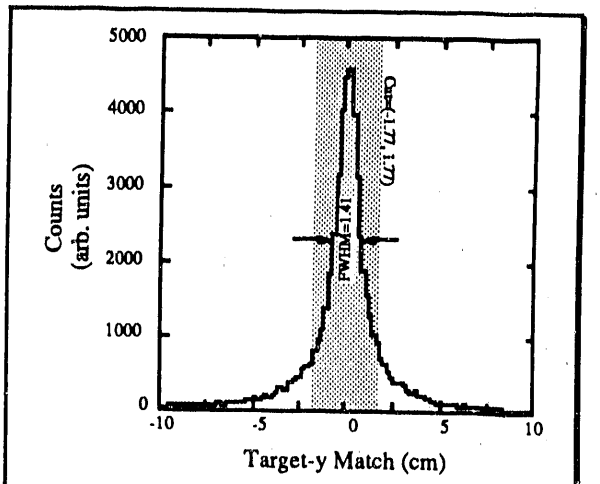

Figure 3-3
Histogram of the difference between the projectile target position and the fragment target position.

The ΔY distribution is a Gaussian ($\Delta(\Delta Y)_{fwhm} = 1.41$ cm) with long tails in both directions (see Figure 3-3). Requiring that valid events have a value of $\Delta Y = [-1.77, 1.77]$ eliminates 30.3% of target in events that pass the r_{foc} cut. This is higher than expected by interactions in the matter between WC2 and the drift chamber because events where either the upstream of downstream track is inaccurately measured will also be eliminated by this cut.

Region 3: Charge Change Cut

The third reaction region extends from the back of the drift chamber through the VMD and contains the largest source of reactions. The combination of the S3 scintillator, approximately 0.75 m of air, and 2-4 planes of the VMD provides a cumulative thickness of 2.4-4.8 g/cm^2 of material with which the fragments can react.

Since the first object (S3) and the last object (VMD-G) encountered in Region 3 measure the charge of the particle independently, a natural signature for detecting reactions in this region is a charge change of the fragment between these two detectors. We define the variable:

$$\Delta Z_3 \equiv Z_{S3} - Z_{VMD} \qquad \textbf{Equ. 3.3.3}$$

where Z_{VMD} and Z_{S3} are the charge measured for a projectile fragment by the glass wall of the VMD and by the beam veto scintillator S3, respectively.

The distribution of ΔZ_3 shows a gaussian-shaped peak ($\overline{\Delta Z_3} = 0.0$ e, $\Delta(\Delta Z_3)_{fwhm} = 2.21$ e), with a low background for negative values, and a large positive tail (see Figure 3-4). Particles which have the same charge in the S3 trigger scintillator, and in the glass wall of the VMD (ie. the gaussian-shaped peak) can be assumed to not have reacted in the material between the two detectors. Those particles which show a charge loss ($\Delta Z > 0$ corresponding to the positive tail) almost certainly have reacted in the intervening matter. Those events where an apparent charge increase has taken place ($\Delta Z < 0$ corresponding to the low negative tail) reflect the limitations of the experiment (ie. misidentification of charge in the S3 scintillator, multiple fragments incident on a single VMD radiator, or fragmentation within the charge measuring VMD radiator).Valid fragment measurements are defined as those satisfying $\Delta Z_3 = [-1.86, 2.78]$. This cut excludes 23.9% of target in events that pass both the r_{foc} and ΔY cuts.

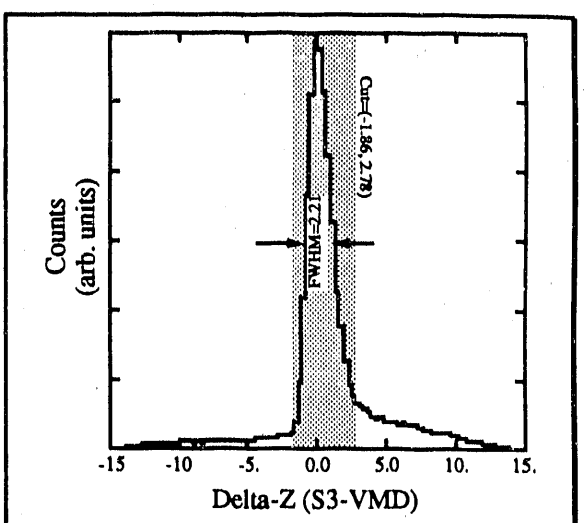

Figure 3-4
Histogram of the difference between fragment charge measured in the VMD and that measured in S3

3.4. Cross Section Calculation

For beam incident on a target of thickness 1 nucleus·cm^{-2}, the production cross section (σ) for fragment $^{A}Z_f$ is defined by the equation:

$$N_f = I_0 \cdot (1 - e^{-\sigma l}) \qquad \textbf{Equ. 3.4.1}$$

where N_f is the total number of particles of species $^{A}Z_f$ produced for a total number of incident beam nuclei I_0, and the units of σ are cm^2. However, because of the nature of experiment, N_f, I_0, and l are seldom measured directly.

Targets

The most directly measurable quantity is the thickness of the target (l). The thicknesses of the targets used in our experiment were:

Target	t* [mg/cm^2]	<A>	l [nuclei·cm^{-2}]
C	500 ± 7.1	12.01	$2.507 \times 10^{22} \pm 1.4\%$
KCl	367 ± 5.3	37.28	$5.928 \times 10^{21} \pm 1.4\%$

where we use the natural abundances of isotopes of C, K, and Cl to calculate <A>.

Spill Scalers

The incident beam intensity used in Equation 3.4.1 (I_0) is calculated from scalars recorded in the data stream. The salient scalars are: 1) S13: Events Accepted (S_{ea}), 2) S14: Event Triggers (S_{et}), 3) S47: Beam Triggers (S_{bt}), and 4) S48: Interaction Triggers (S_{it}). The value of S_{ea} is equal to the scaled number of events written to magnetic tape. S_{et} is the scaled number of events satisfying the current trigger level (either INT or BEAM--see Section 2.2), whether the events are recorded or not. The scalars S_{bt} and S_{it} are the number of events satisfying the BEAM and INT trigger levels, respectively. When operating the system with the BEAM trigger, the S_{et} and S_{bt} scalars are equivalent; when operating with the INT trigger, S_{et} and S_{it} are equivalent. However, both S_{bt} and S_{it} are present in the data stream regardless of the trigger level used.

---

* The uncertainties on these thicknesses assume an accuracy in measuring the target mass of 0.1 g, and an accuracy in measuring the target dimensions of 0.1 cm.

The first two scalars (S_{ea} and S_{et}) allowed us to calculate the dead time (t_d) due to the the time taken by the electronic trigger and the readout time of the data acquisition system. The third scalar (S_{bt}) is the beam intensity on target, but must also be dead time corrected before use in Equation 3.4.1.

The dead time of the system is calculated by:

$$t_d = 1.0 - \frac{S_{ea}}{S_{et}} \qquad \textbf{Equ. 3.4.2}$$

and the dead time corrected intensity (I) is calculated by:

$$I = S_{bt}\cdot(1.0 - t_d) \qquad \textbf{Equ. 3.4.3}$$

The dead time of the system typically was on the order of 50-60%.

It should be noted here that the scalar values recorded in the data stream are very close to the real values used in Equations 3.4.2 and 3.4.3. However, a comparison between the number of events actually recorded on tape (N_{evt}) with the Events Accepted scalar (S_{ea}) showed a small discrepancy. This discrepancy arose from the circumstance of a data run beginning or ending during the spill flat-top (i.e. between the clear and the read of the end of spill scalars). All scalars taken from the data stream were corrected by the factor: $\varepsilon_1 = (N_{evt}/S_{ea})$. However, this correction is quite small ($\approx 0.3\%$).

Cut Corrections

Corrections, either to the intensity or the isotope population, were applied to compensate for the reaction losses described in Section 3.3.

Because the r_{foc} cut is applied to the data before it interacts in the target (i.e. only upstream information is used for this cut) the r_{foc} cut is conceptually equivalent to reducing the intensity of the incident beam. Therefore, applying this cut requires that we multiply the incident intensity (I) by the factor ε_I:

$$\varepsilon_I = \left(\frac{N_i}{N_i + N_o}\right) \qquad \textbf{Equ. 3.4.4}$$

where N_i, and N_o are the number of nuclei inside the r_{foc} cut boundaries, and the number outside, respectively.

The ΔY cut is intended to eliminate interactions with material downstream of the target (predominantly the HISS vacuum window and air upstream of the drift chamber). The number of events failing the ΔY cut relative to the beam intensity is a measurement of the interaction ratio of projectiles with this material. To correct for loss to the population of an isotope due to the ΔY cut, we multiply the isotope population by the factor ε_{P1}:

$$\varepsilon_{P1} = \left(\frac{1}{1-\left(\frac{N_O}{I}\right)} \right) \qquad \textbf{Equ. 3.4.5}$$

where N_O is the number of nuclei outside of the ΔY cut boundaries and I is the dead time corrected beam intensity (after correction by ε_I)* .

The ΔZ_3 cut eliminates primarily interactions in the air between the S3 scintillator and the VMD, and in the quartz wall of the VMD. Population loss resulting from the application of the ΔZ_3 cut is corrected by multiplying the isotope populations by the factor ε_{P2}.

$$\varepsilon_{P2} = \left(\frac{1}{1-\left(\frac{N_O}{N_O + N_i}\right)} \right) \qquad \textbf{Equ. 3.4.6}$$

where N_O and N_i are the number of nuclei outside and inside the ΔZ_3 cut boundaries, respectively.

It should be noted at this point that the application of these data cuts and the subsequent population and intensity corrections do not change the IPCSs for charges $Z_f \geq 11$ by more than the statistical uncertainty. The cut levels were chosen to reflect the width of the distribution of the cut variable involved. To account for uncertainties in the cross sections due to these cuts, we used the change in PCS between different cut levels (see below).

---

* NB.This correction neglects any $A^{1/3}$-like dependence of the reaction cross sections for different fragment species.

Trigger Bias

The S3 trigger scintillator was designed to eliminate triggers of the data acquisition system by beam. However, the threshold for S3 was set such that events triggered by nuclei with charge lower than the beam were also vetoed by the INT trigger. To calculate cross sections for nuclei close to the beam, a trigger bias correction was necessary.

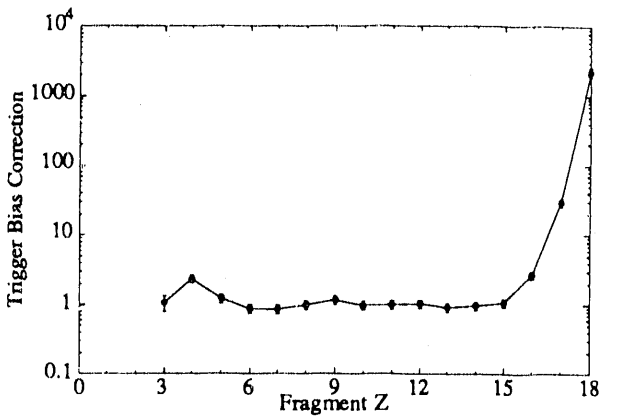

Figure 3-5
Dividing the BEAM Trigger element populations by the INT Trigger populations and normalizing to 1.0 for $Z \leq 15$ gives the Trigger Bias Correction used.

Figure 3-5 shows the ratio of elemental yields for the BEAM and INT triggers. This ratio, defined as:

$$R = \left(\frac{N_B(Z)}{N_I(Z)}\right) \qquad \textbf{Equ. 3.4.7}$$

(where $N_I(Z)$ and $N_B(Z)$ are the populations of fragments of charge Z for the INT and BEAM triggers, respectively) is the trigger bias correction. Since the correction differs from 1.0 only for fragments of charge $Z_f \geq 16$, it is not applied to fragments below Sulfur.

Background Subtraction

Because we know that the data cuts do not eliminate <u>all</u> interactions in the background data (This is confirmed by application of the cuts to a target out run.), we must subtract normalized target out background from our target in data before calculating our cross sections.

Applying the same data cuts to the target out data, we need then normalize the target out isotope populations to the ratio of the corrected beam intensities.

$$N'_f = N_f\left(\frac{I_{TI}}{I_{TO}}\right) \qquad \textbf{Equ. 3.4.8}$$

where N_f and N'_f are the unnormalized and normalized isotopes populations, and where I_{TI} and I_{TO} are the target in and target out beam intensities (NB Both the populations and the intensities are corrected by the cut ε factors discussed above.).

Uncertainties

The uncertainties for our cross sections are effected by three factors. 1) The statistical uncertainties of the data (both target in and target out uncertainties, including the uncertainty from the trigger bias correction, if any). 2) The physical uncertainty in measuring the target thickness. And 3) uncertainty induced by the application of our data cuts. The first two factors are handled by normal propagation of error techniques, but the third effect is less straight forward.

By inspection of the data under a wide range of cut requirements, we have determined the final values of the r_{foc}, ΔY, and ΔZ_3 cuts based on the position of the peak of each cut variable, and on 3 times the standard deviation of that peak (We have adopted the term "3rd level cuts" for this condition.). We have determined empirically that the absolute magnitude of the calculated cross sections for the most populous isotopes do not change dramatically until the cut tightness reaches level 2 or lower. The relative magnitudes are even less sensitive to the cuts applied.

As an estimate of the uncertainty introduced into the calculation by the application of the cross section cuts, we have used the difference between the level-2 and level-4 cuts (i.e. 0.67 and 1.33 times the cut tightness of the level-3 cuts). This uncertainty is then added in quadrature to the uncertainty for the third level cut (due to statistical and target thickness effects).

$$\Delta\sigma = \sqrt{(\Delta\sigma_3)^2 + \left(\frac{\sigma_4 - \sigma_2}{2}\right)^2} \qquad \textbf{Equ. 3.4.9}$$

where σ_i is the i^{th} level calculation of the cross section, and $\Delta\sigma$ is the uncertainty of the cross section.

3.5. Momentum Distribution Extraction

The momentum distributions directly measured in the experiment for projectile fragments arise from nuclear interactions in the target (the physically meaningful component), from interactions and multiple scattering in the background material, and from widening of the distributions due to detector system resolution. To extract the momentum distributions that we can compare with theory, we start with raw momentum distributions (cut as discussed in Section 3.3) in the three momentum dimensions for each isotope for both target in and target out. For this discussion, $\hat{z}$ is designated as the beam direction, $\hat{y}$ is vertical , and $\hat{x}$ is horizontal, forming a right-handed coordinate system.

Background Subtraction

The target out distributions represent the measured distributions of fragments that react outside of the target area, and are present in the target in data with the same magnitude (the amount of background material is the same for both target in and target out). Normalizing by the dead time corrected beam intensities, we subtract the target out distribution from the target in distribution to remove the background component (see Figure 3-6).

Resolution Correction

What remains are p-distributions of reactions within the experimental target. However, these distributions are widened by the effective resolution of the detector system (i.e. Intrinsic detector resolutions, Multiple Coulomb Scattering, etc). We can determine the magnitude of this widening by examining the ^{40}Ar distributions for target in / BEAM Trigger data. The primary beam nuclei detected in the downstream detectors have gone through the same background material and are measured by the same detectors as the projectile fragments. Thus, the momentum distributions of the ^{40}Ar beam are contaminated by the same effects as the distributions of the fragments. However, unlike fragment nuclei, beam nuclei start through the system with effectively a delta-function momentum distribu-

tion ($\Delta p/p < 10^{-3}$). Therefore, any momentum width measured for the beam arises from the widening of this delta-function distribution by elastic interactions in the target and downstream matter, and by the resolution of the detector system and analysis.

To calculate the momentum resolution of the spectrometer system we use the relationship:

$$\frac{\Delta R}{R} = C_1 \cdot R \qquad \textbf{Equ. 4.5.1}$$

where C_1 is a constant and $R = p/Z$. We can use the measured resolution of the beam to calculate C_1 and hence, extrapolate the momentum resolution of smaller fragments.

$$\Delta p_z(Z_f, A_f) = \frac{C_1 \cdot A_f^2}{Z_f} \qquad \textbf{Equ. 4.5.2}$$

Because the momentum distribution measured in the lab for p_z is Lorentz boosted, the width of the distribution must be divided by a factor of $\gamma = 2.757$ to calculate the momentum distribution width in the projectile frame.

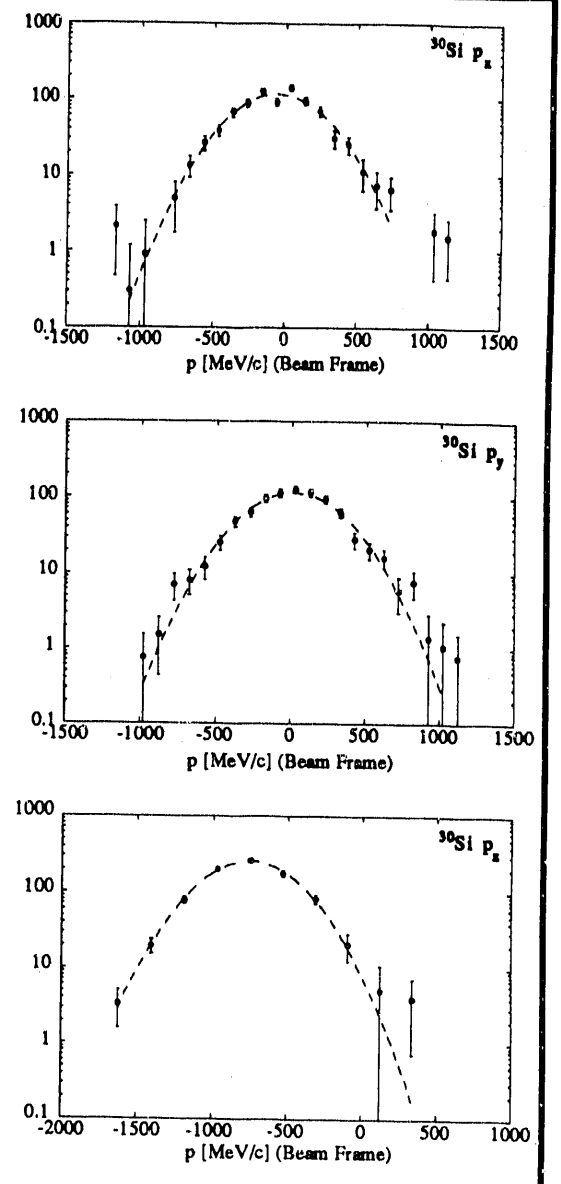

Figure 3-6
The momentum distributions for ^{30}Si are gaussian in all three coordinates.

In the vertical direction ($\hat{y}$ direction), the resolution in momentum is essentially the angular resolution of the downstream vectoring detector (pDC), which is a constant. For small angles:

$$p_y(A) = p_0 \cdot A \cdot \sin(\theta_y) \approx p_0 \cdot A \cdot \theta_y \qquad \textbf{Equ. 4.5.3}$$

$$\Delta p_y(A) = p_0 \cdot A \cdot \Delta\theta_y = C_2 \cdot A \qquad \textbf{Equ. 4.5.4}$$

where p_0 is the longitudinal momentum per nucleon of the detected fragment (a constant within uncertainty).

In the horizontal ($\hat{x}$) direction, the prescription for resolution correction is less clear. Because both the x and z momenta are calculated using the horizontal positions and angle of the vectoring detectors (Since the bending plane of the HISS magnet is horizontal.), the measurements of these two components of the momentum are coupled. However, because p_x is determined by the horizontal scattering angle at the target (as p_y is determined by the vertical scattering angle), we use the same resolution correction for the p_x distributions as used for the p_y distributions (i.e. Equation 4.5.4).

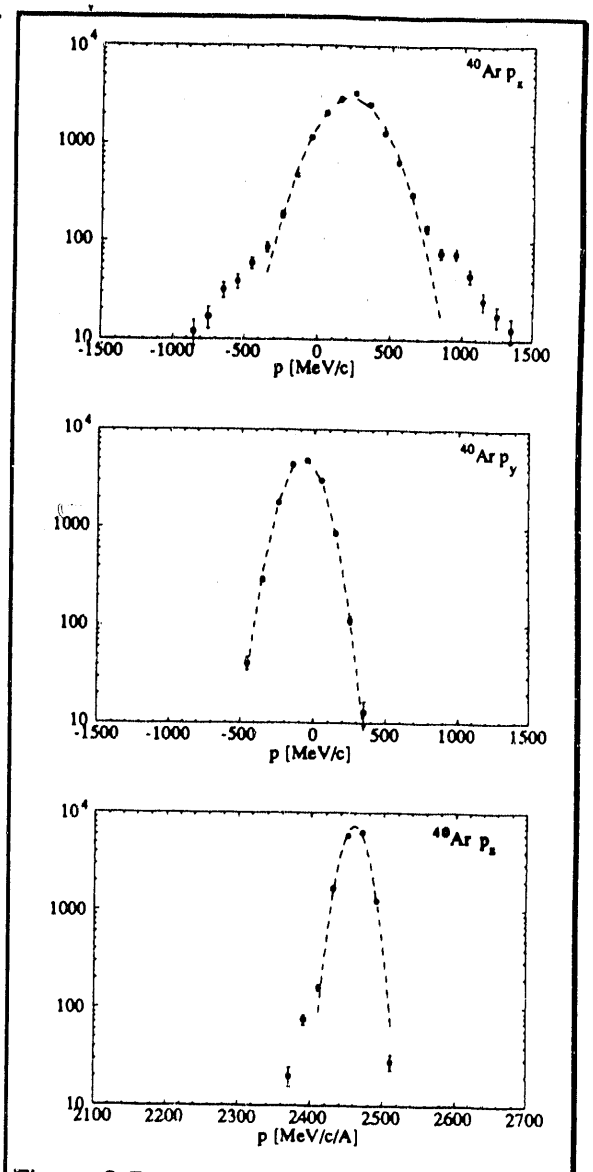

Figure 3-7
The momentum resolution in three dimensions is demonstrated by the widths of the ^{40}Ar momentum distributions.

The measured beam momentum distributions for $^{40}Ar + C$ are gaussian (Although p_x has a wide background, presumably from the p_z contamination.) as expected, and typically constitute a 5-10% correction to the data (see Figure 3-7). Because of the difficulty in fitting low statistic (low cross section) isotopes, we only fit momentum distributions of those isotopes with production cross sections of $\sigma(Z,A) \geq 10$ mb. This resulted in momentum distributions being fitted for 41 isotopes.

Detector Acceptance

One effect that can alter the momentum distributions is the acceptance of the detector system. We have addressed this consideration by two approaches and conclude that the effect appears insignificant.

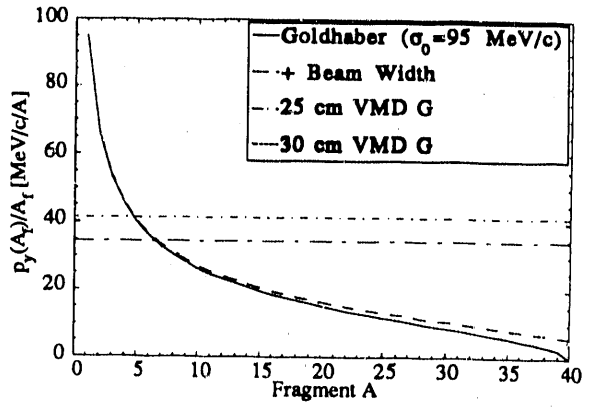

Figure 3-8
The predicted momentum width per nucleon (proportional to opening angle) calculated from the theory of Goldhaber and convoluted with the measured beam momentum width is less than the opening angle described by the glass wall of the VMD (horizontal lines).

First, we have visually inspected the individual momentum distributions for evidence of edge effects or deviations from a gaussian shape. Secondly, for the $\hat{y}$ direction, we have imposed an artificially narrow aperture through software cuts to note the effect on the widths of the fitted gaussians. For the isotopes tested, the vertical aperture cut did not significantly affect the gaussian fit to the p_y distribution for $y_{app} \geq 20$ cm.

The vertical aperture of the system is most tightly constrained by the glass wall of the VMD. The active vertical aperture of the glass wall is 25-30 cm and is ≈ 870 cm from the target. For a fragment of p/A = 2400 MeV/c/A, this translates into a vertical acceptance of 69-82 MeV/c/A. As a rough illustration of the vertical aperture of the system, we can plot the expected vertical opening angle for projectile fragments as calculated by Goldhaber's formula (assuming $\sigma_0 = 95$ MeV/c), convoluted with the beam momentum width and compare with the opening angle of the glass wall of the VMD (see Figure 3-8). (Without accepting the validity of Goldhaber's model, it has been shown to be an accurate predictor of momentum widths for RHI fragmentation.) We see that for fragments of mass $A_f \geq 18$ the vertical acceptance is more than twice as wide as the expected opening angle.

Sampling more than 2 standard deviations of the vertical momentum distributions should allow accurate reconstruction of the total momentum distribution.

4. Experimental Results

4.1. Leading Charge vs. Mid-Rapidity Multiplicity

One simple consequence of the participant-spectator model of relativistic heavy ion interactions is the resultant anti-correlation expected between the mass of either of the two spectator regions and the mass of the participant region. As impact parameter decreases, the amount of overlapping nuclear material increases. Provided the A/Z ratio of the participant matter does not change drastically with impact parameter, the charge of the participant region will also increase with decreasing impact parameter. At the same time, as more of each nucleus can be classified as participant matter, the spectator pre-fragments must decrease in mass and charge.

Using the fragment charge (Z_f) as measured by the VMD for an indication of the pre-fragment size, and using the multiplicity measured by the MA for the participant size, we are able to demonstrate that this general picture is supported in our data.

Figure 4-1 shows two multiplicity distributions. The solid line is the distribution for events where a projectile fragment of $Z_f \geq 12$ was detected downstream in the VMD. The dashed line is the multiplicity distribution for events where the largest projectile fragment had a charge of $Z_f < 12$ as detected in the VMD. What we see is that the distribution for those events with low fragment charge has a pronounced high-multiplicity tail. The distribution from the high-Z events, on the other hand is more strongly peaked at low multiplicity.

An equivalent demonstration of this principle is the plot of Figure 4-2. Here we histogram the leading fragment charge as measured in the VMD for low (< 5) and high (≥ 5) multiplicities in the MA. Although the trigger and drift chamber efficiencies cut off the upper and lower Z regions, we can still clearly see that the low multiplicity events are

associated more strongly with high-Z fragments, and the high multiplicity events with low-Z fragments.

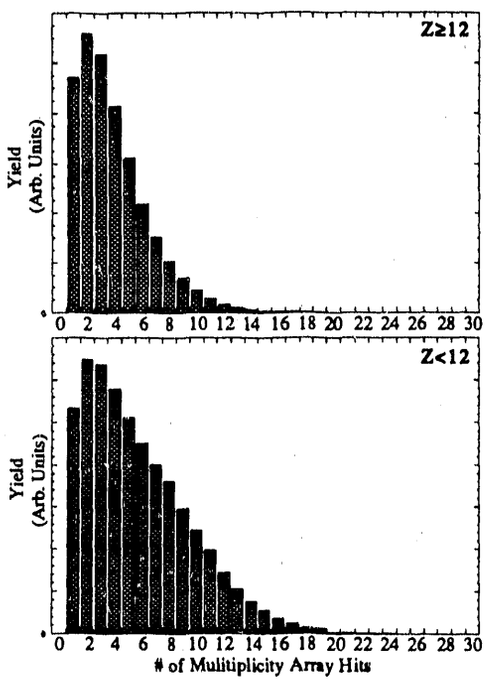

Figure 4-1
Cutting on the leading fragment charge seen in the VMD changes the multiplicity distribution seen in the MA.

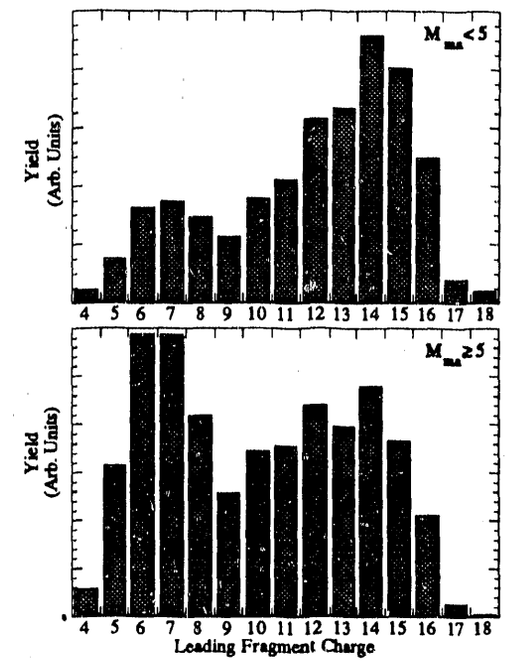

Figure 4-2
Cutting on the multiplicity distribution seen in the MA changes the distribution of leading fragment charge seen in the VMD.

These results strongly support the validity of the participant-spectator model, and also suggest that measuring the leading fragment charge is a good impact parameter measurement. Certainly, it is much easier to measure the charge of the kinematically focused projectile fragments for a reaction rather than the mid-rapidity participants.

4.2. Production Cross Sections

Table III contains the results of our cross section measurements for both targets (C and KCl). A total of 109 isotopes between ^{7}B and ^{40}Cl are listed. Of these, we measured the Isotopic Production Cross Sections for 93 isotopes. Presented in Table III are also the IPCSs for $8 \leq Z_f \leq 16$ as measured by Viyogi et al[79Vi] at 213·A MeV for a C target and

as calculated by Oliveira[78Ol] using the OVERLAID-ALICE evaporation code. The numbers here are the calculations using the Giant Dipole Resonance (GDR) for the initial prefragment charge dispersion, and adding an Final State Interaction (FSI) excitation energy with energy parameter E_{fsi} = 40 MeV. We have performed an Abrasion Ablation calculation using code incorporating the GDR charge dispersion, the Final State Interaction, and an evaporation code typically used for comparison with heavy ion experiments at lower energy.

In Figures 4-6 and 4-7 we compare the IPCSs for $8 \leq Z_f \leq 16$ from our experimental data with the measured cross sections of Viyogi and the Abrasion Ablation calculation of Oliveira. Both the shape and the magnitude of the data are well reproduced by the AA;GDR+FSI calculation. However, the calculation systematically underpredicts the neutron rich tail of the IPCS distribution. Also well reproduced is the position of the peak of the distribution as a function of fragment charge.

The experimental data at 213·A MeV appears similar to our own data, especially for the Z_f = 16 cross sections. However, the peaks of the distributions are not as well matched as are the peaks for the calculation (Note the distributions for P, Al, Na, and Ne.). The absolute magnitude of the distributions for the two experiments should not be compared because there is an uncertainty in the 213·A MeV data of approximately a factor of 2 in the overall normalization. It should be stressed that the comparison of our data with the AA calculation of Oliveira requires no normalization. The comparison made by Viyogi et al used normalization factors between 1 and 2 (see Figure 1-5).

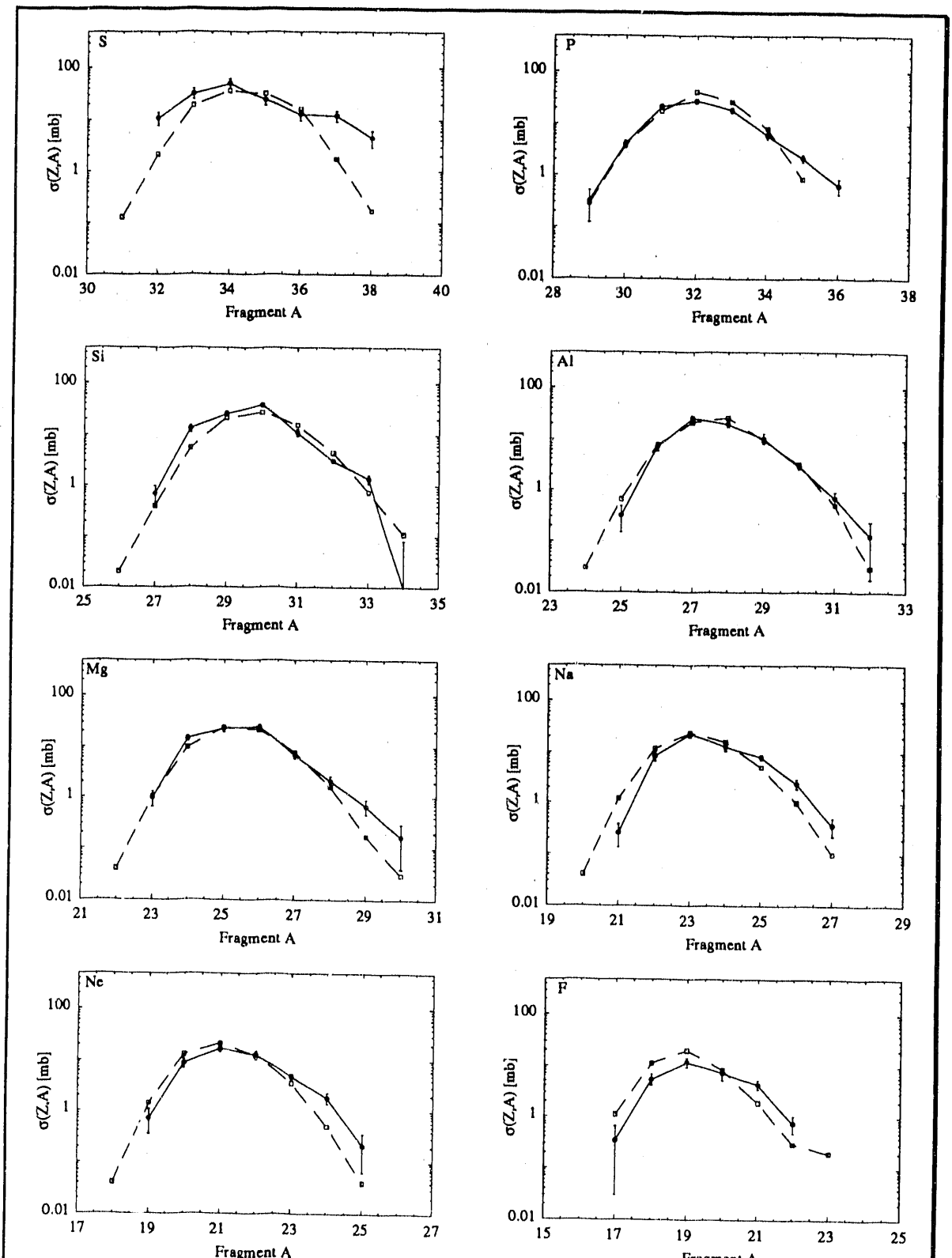

Figure 4-6 a-h (Cont')

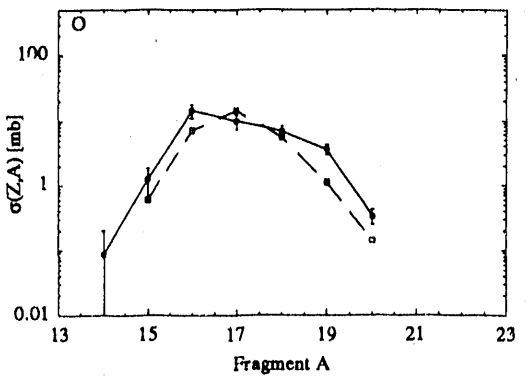

Figure 4-6
The production cross sections for isotopes of Oxygen through Sulfur are shown for the measured system of 1.65·A GeV ^{40}Ar + C (Solid line), and for the Abrasion-Ablation calculation of Oliveira with the GDR assumption plus additional FSI excitation energy (Dashed line).

In general, in comparison with Oliveira's calculation we see: 1) The IPCS distributions are roughly gaussian in shape with a neutron-rich tail and fall off approximately 1 order of magnitude per 2 mass units on the neutron-poor side, and approximately 1 order of magnitude per 2.5-3 mass units on the neutron-rich side. 2) For $10 \leq Z_f \leq 15$, the amplitude of the IPCS distribution is quite well reproduced by the AA;GDR+FSI calculation. 3) In general, the calculation underpredicts the cross sections on the neutron-rich tail of the distribution. And 4) the position of the peaks of the calculation matches the position of the peak of the data.

By inspection of Figure 4-6, we see that the shapes of the IPCS distributions for $8 \leq Z_f \leq 15$ appear Gaussian (neglecting the neutron-rich tail). As an aid to discussion we fit Gaussians to the distributions (ignoring the lack of agreement with the neutron-rich tail). Although the χ^2 of the fits are poor, the fitted gaussians do reproduce the shape of the center of the distributions well enough to allow us to quantitatively discuss the position, width, and magnitude of the distributions.

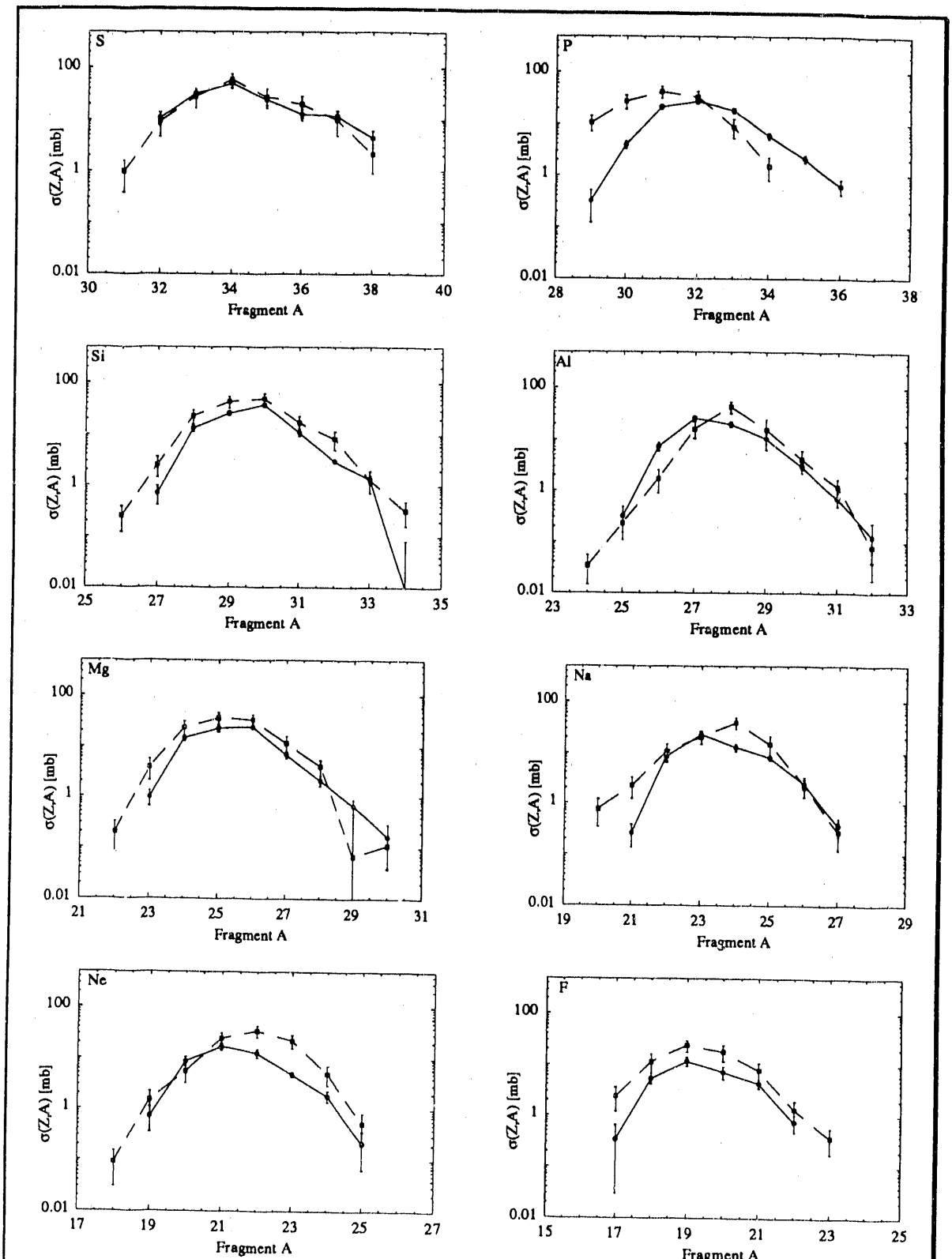

Figure 4-7 a-h (Cont')

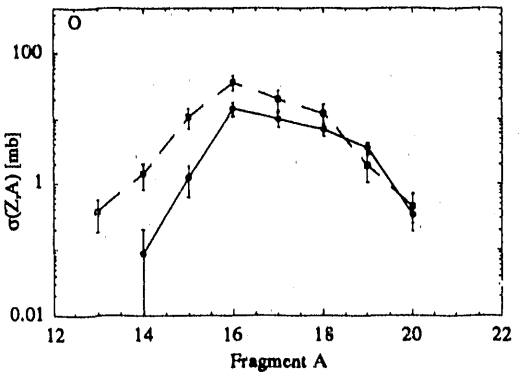

Figure 4-7
The production cross sections for isotopes of Oxygen through Sulfur are shown for the measured systems of 1.65·A GeV ^{40}Ar + C (Solid line), and 213·A MeV ^{40}Ar + C of Reference 79Vi (Dashed line).

If we use the fitted Gaussian ($y = m_1 \cdot \exp\left(-(x-m_2/2 \cdot m_3)^2\right)$ for each element as a reference point, we can normalize the PCS to the amplitude of the gaussian ($\sigma'(Z, A) = \sigma(Z, A)/m_1$), and normalize the fragment mass number to the mean of the gaussian ($A' = A_f - m_2$). When we graph all of these normalized data on one plot for all isotopes between ^{8}B and ^{36}S (Figure 4-8), we see that the shapes of the IPCS distributions are very similar. Further, the weighted mean of the points as a function of x falls to 1 order of magnitude less than the peak at $A' \approx -2.0$ and $A' \approx +2.7$.

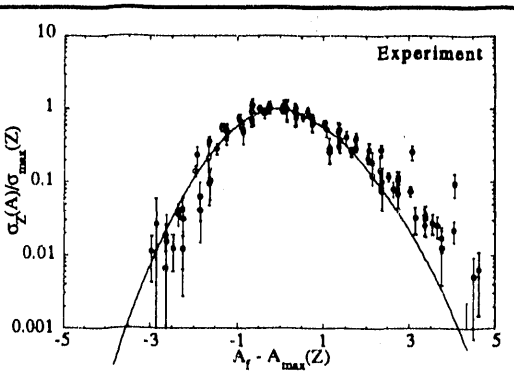

Figure 4-8
Plot of IPCS normalized to the amplitude of a fitted Gaussian vs. A_f relative to the mean of the same Gaussian for experiment. (^{8}B-^{37}Cl). The fit curve for theory (solid line) falls below the data for $A_f - A_{max}(Z) > 1$.

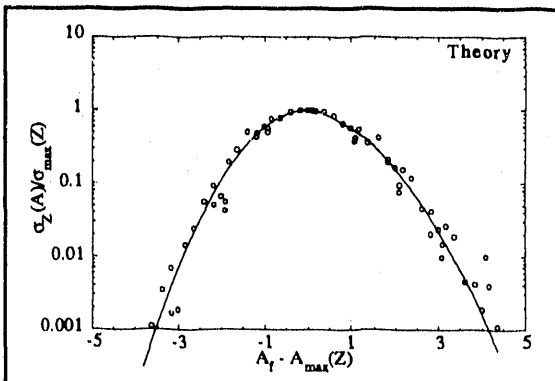

Figure 4-9
Plot of IPCS normalized to the amplitude of a fitted Gaussian vs. A_f relative to the mean of the same Gaussian for theory. (^{15}O-^{38}S). Two Gaussians are fitted to the two sides of the plot for comparison with data.

Applying the same procedure to the calculation of Oliveira, we get Figure 4-9. The neutron rich side of the distribution falls off 1 order of magnitude at $A' \approx 2.1$, thus under-predicting the neutron rich side of the experimental distribution. However, the neutron poor side falls off at approximately the same rate (1 order of magnitude per 2 mass units) as does the data. The solid line in both Figure 4-8 and 4-9 is the best fit Gaussians for the two halves of the points in Figure 4-9.

Summing the IPCSs for each isotope of an element gives us an Elemental Production Cross section (EPS). The calculated magnitude and the dependence on Z_f of the elemental production cross sections agree with the data for $8 \leq Z_f \leq 16$.

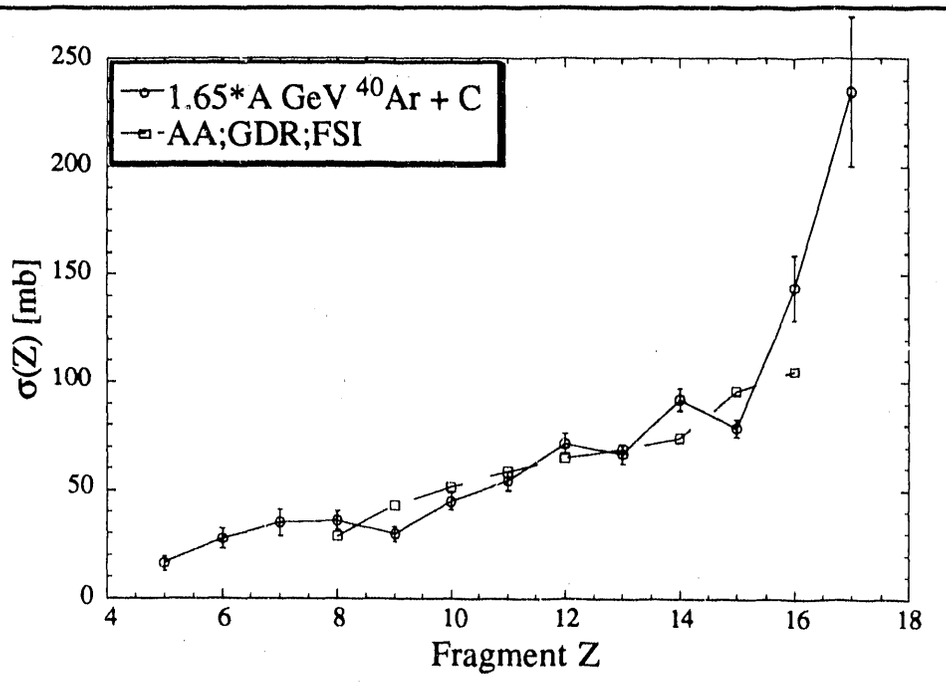

Figure 4-10
Integrating over fragment mass, the Elemental Production Cross Sections for $8 \leq Z_f \leq 16$ exhibit the same slope ($\Delta\sigma/\Delta A$) and magnitude as calculated from the Abrasion-Ablation Model.

We can qualitatively compare the positions of the peaks of the IPCS distributions for both theory and data. The positions of the peaks are linear in Z_f, and roughly follow the valley of β-stability. For each isotope, we determine the valley of β-stability as the isotope

with the largest binding energy per nucleon. Fitting a line through the points for $2 \leq Z \leq 18$ and plotting the distance (in A) between the line and the position of the peak, we get the plot in Figure 4-12. We see that the peak of the IPCS distributions (for both data and theory) parallel the linear fit to the points for the valley of β-stability (A_β), while the peak of the Abrasion pre-fragment parallels the A/Z of the beam.

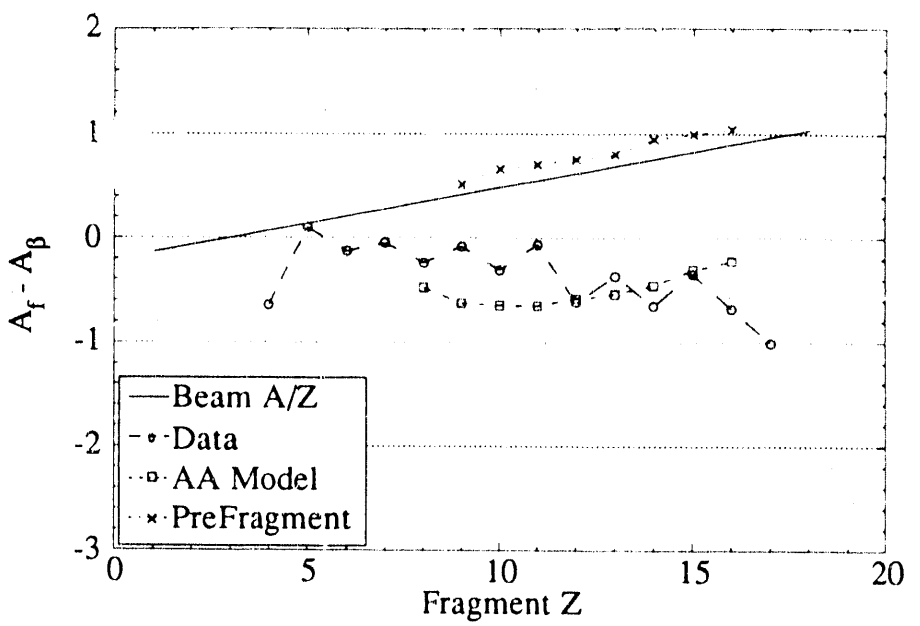

Figure 4-12
The positions of the peak of the IPCS distribution for the Abrasion pre-fragments parallels the line of the beam A/Z ratio. However, the experimental and theoretical final fragments peak on the neutron poor side of the valley of beta stability.

These comparisons suggest that the Abrasion-Ablation Model is a valid representation of the fragmentation process. However, Oliveira calculated ^{40}Ar IPCSs for only one target (C), and did not publish cross sections for fragments outside the range $8 \leq Z_f \leq 16$. Because we have measured cross sections for fragments of charge $5 \leq Z_f \leq 17$ and fragments from reactions with two targets (C and KCl), an Abrasion-Ablation code was needed to test the entire data set against the model. We were unable to locate the original code used by Oliveira. However, we have tested other Abrasion Ablation codes and present here the results of our calculations.

We were able to obtain and test a total of three programs; one abrasion code (FRAGMNT[89Mo2]), and two statistical decay codes (EVA[89Mo2] and GEMINI[89Pe]). The abrasion code uses the analytic functions of Reference 78Mo and calculates the abrasion pre-fragment charge dispersion by either the Giant Dipole Resonance Method or the Hyper-Geometric Method. The output is a collection of the possible abrasion pre-fragments with associated production cross sections and excess surface area excitation energies(Figure 1-6). To this surface excitation energy, we added an FSI excitation energy spectrum (Figure 1-7) with a binomial probability distribution (Equation 1.4.6) and an adjustable scale factor (E_{fsi}).

The resultant collection of abrasion pre-fragments, cross sections, and excitation energies are then input to one of the two evaporation codes which Monte-Carlos the statistical decay of the pre-fragments by emission of light particles (n, p, d, t, ^{3}He, ^{4}He, etc.).

We were unable to reproduce the shapes of the IPCS distributions using the EVA code, even with extensive tuning of internal parameters and excitation energy spectra. The resultant distributions were too narrow, and exhibited discontinuities that are clearly not seen in the data (or in Oliveira's original calculation). However, we have recently succeeded in reproducing the shape and magnitude of the data by using GEMINI.

GEMINI is a statistical model code used at the HILAC for the study of decay of complex nuclei[89Ch]. In the normal mode of operation, GEMINI calculates the decay of an excited nucleus by determining the branching ratios of all possible sequential binary decays from light particle emission, through complex particle emission, up to symmetric division of the nucleus. The input to the calculation is the species (Z, A), excitation energy (E*), and angular momentum (J) of the nucleus (We assumed an angular momentum of 1 $\hbar$ rather than 0 $\hbar$ to avoid any possible computational errors in the program.). The only adjustable parameter internal to the program which we changed is the level density parameter:

$$a = \frac{A}{a_0}\ MeV^{-1} \qquad \textbf{Equ. 4.2.1}$$

where a_0 is the adjustable parameter (typically taken between 8.5 - 15).

Although the output of the code is normally sorted to calculate elemental cross sections, both the charge and mass are output, allowing the calculation of isotopic production cross sections. For our relatively light nuclei ($A \leq 40$), we turned off the fission calculation part of the code, allowing only the emission of light fragments ($Z \leq 2$). Using $a_0 = 12$, and $E_{fsi} = 38.8$ MeV, we calculate the isotopic production cross sections shown in Figures 4-13 (C target) and 4-14 (KCl target).

Inspection of Figures 4-13 and 4-14 show that the Abrasion-Ablation code reproduces the magnitude, shape, and position of the IPCS distributions quite well. Especially impressive is the quality of fit for the neutron-rich tail of the distributions for $Z_f \leq 15$. This tail was the aspect systematically underpredicted by the Oliveira calculation. We have found that the neutron rich tail of the distribution is affected by the choice of the level density parameter a_0. As the parameter a_0 increases, the neutron-rich tail of the distribution becomes more pronounced.

Of special note is the asymmetry of the calculated distribution for Sulphur ($Z_f = 16$). This asymmetry was measured for both targets in our own data, and in Viyogi's 213·A MeV data. The OVERLAID-ALICE calculation predicts a symmetric distribution that does not match the data. However, the absolute magnitude of the S distribution is underpredicted by the model for both targets.

We note that Oliveira explicitly stopped the OVERLAID-ALICE calculation for low mass fragments because the evaporation calculations become unreliable. However, we see reasonably good agreement for fragments as small as Boron.

An particularly interesting IPCS distribution is the distribution for Cl ($\Delta Z = -1$). This distribution is fundamentally different from the distributions we have examined for lower charges.

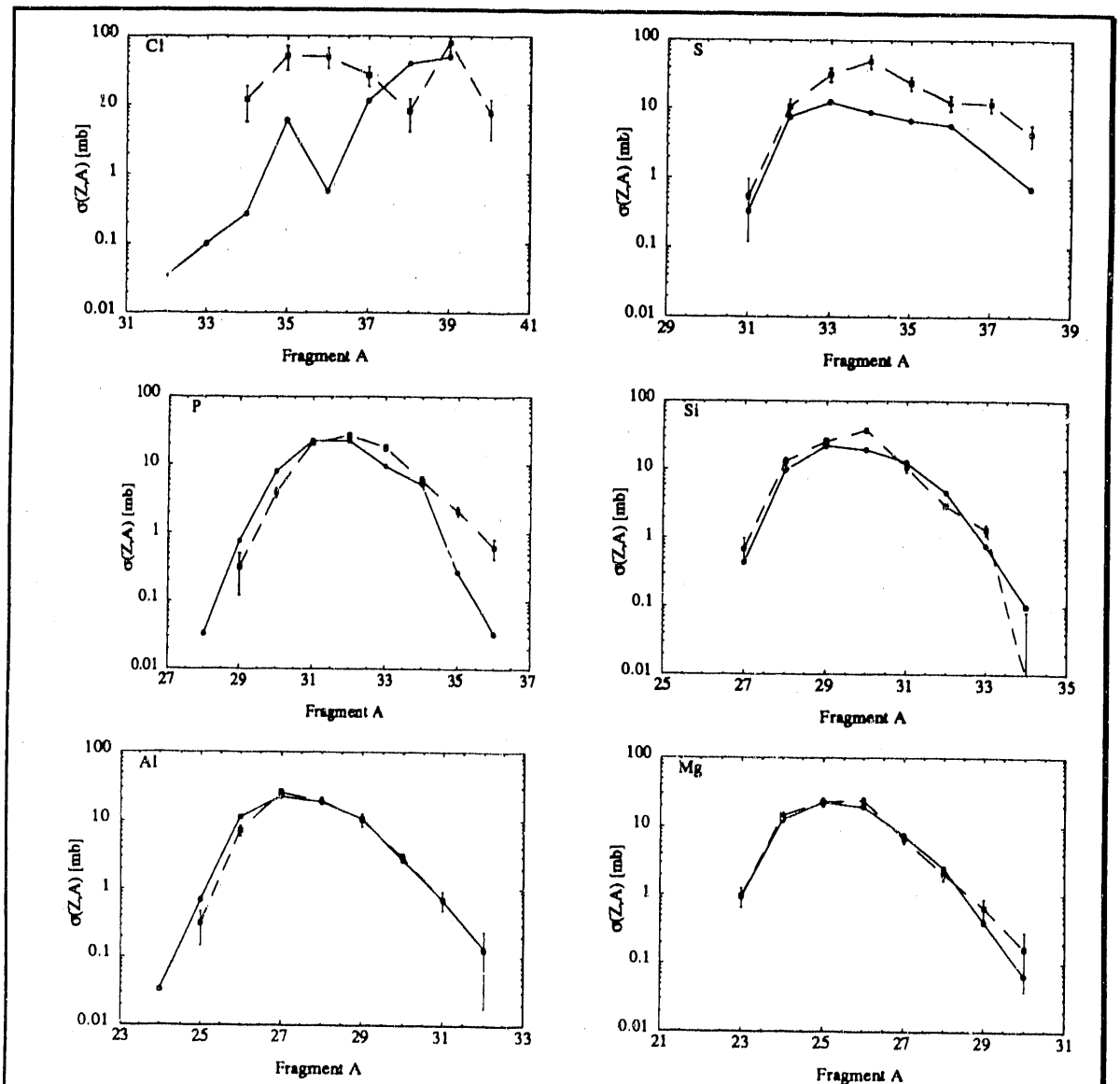

Figure 4-13 a-f (Cont')
Isotopic production cross sections for 1.65·A GeV ^{40}Ar + C, both measured (Solid lines), and calculated by FRAGMNT and GEMINI (Dashed lines).

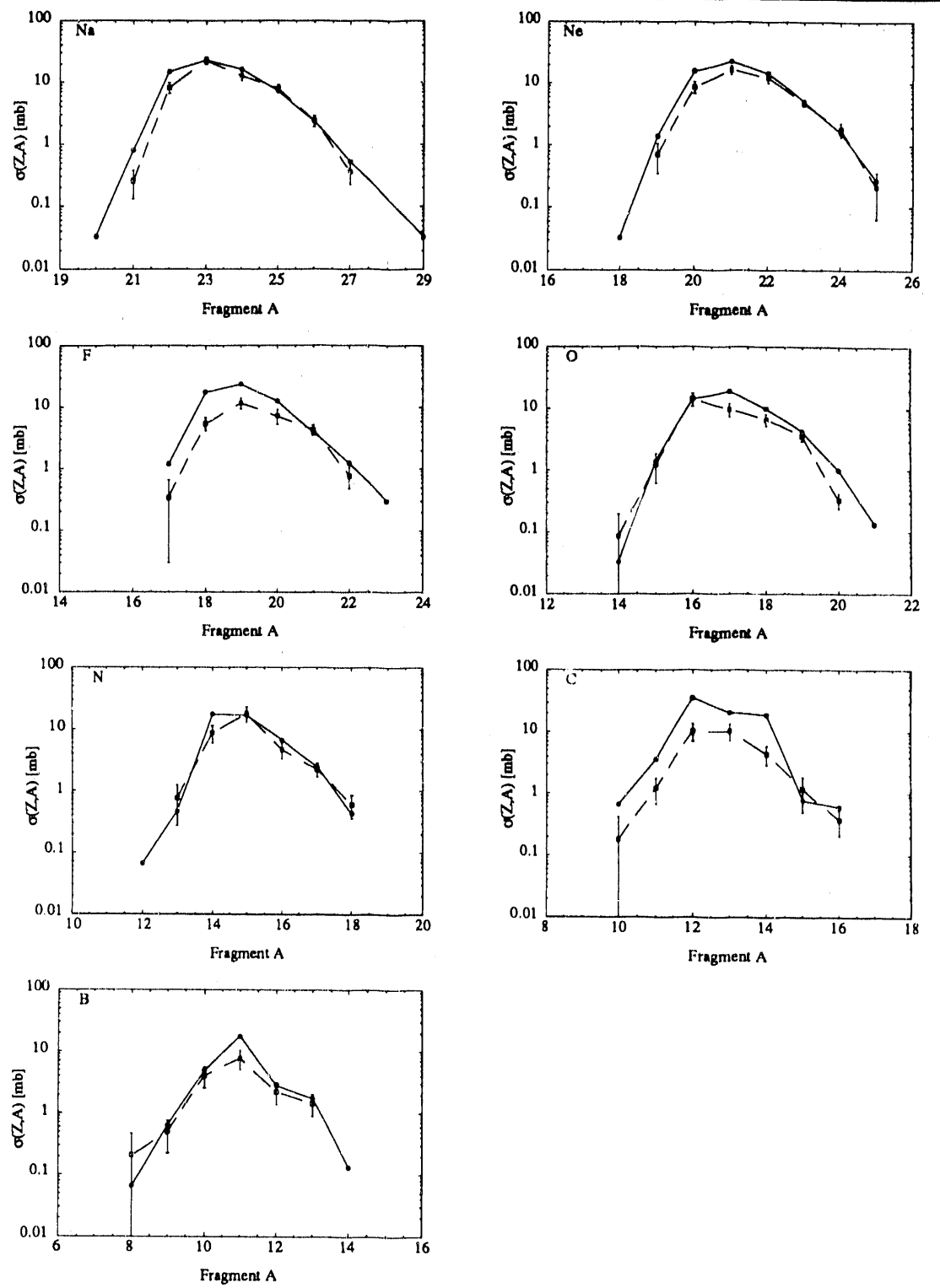

Figure 4-13 g-m
Isotopic production cross sections for 1.65·A GeV ^{40}Ar + C, both measured (Solid lines), and calculated by FRAGMNT and GEMINI (Dashed lines).

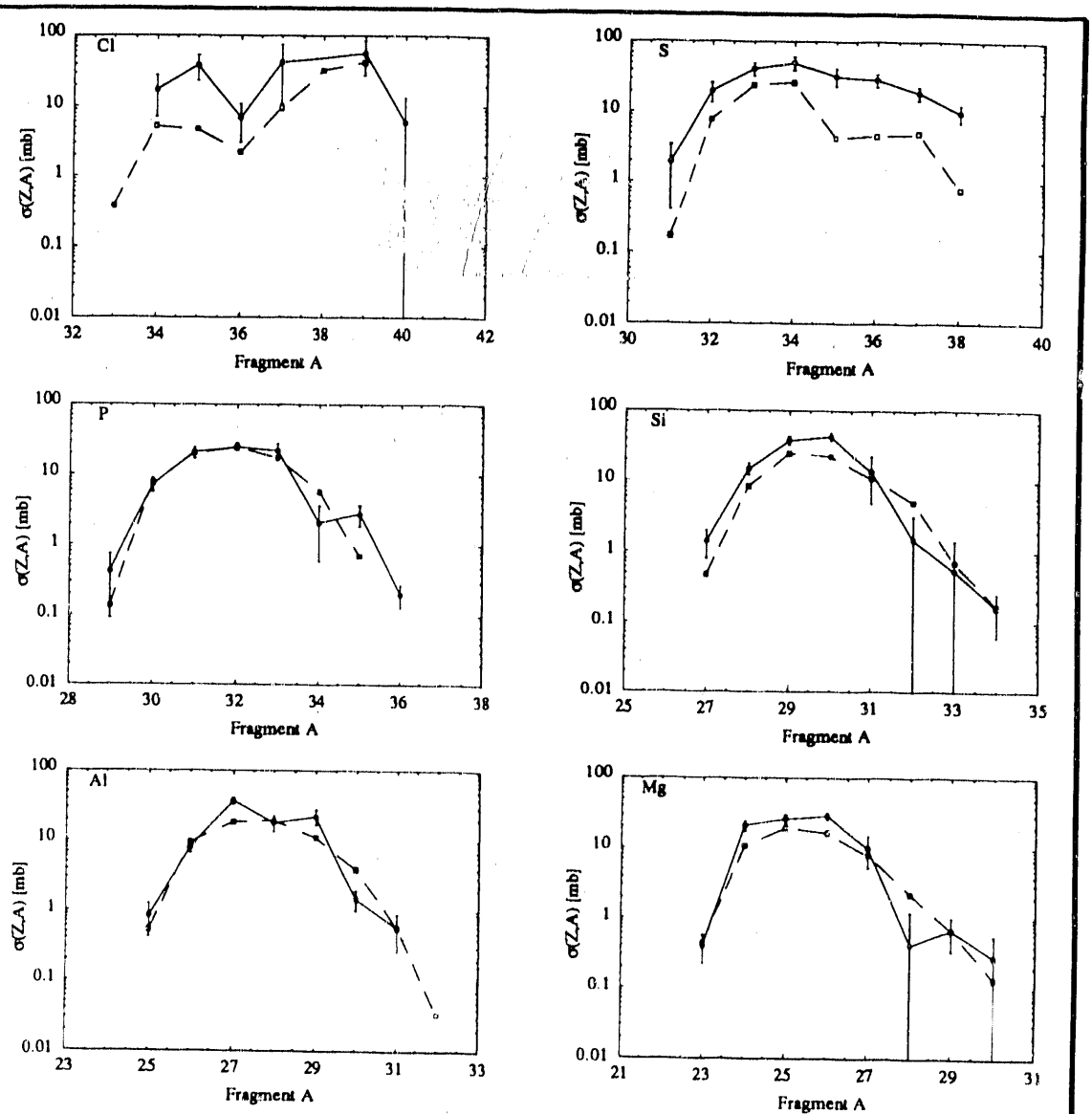

Figure 4-14 a-f (Cont')
Isotopic production cross sections for 1.65·A GeV ^{40}Ar + KCl, both measured (Solid lines), and calculated by FRAGMNT and GEMINI (Dashed lines).

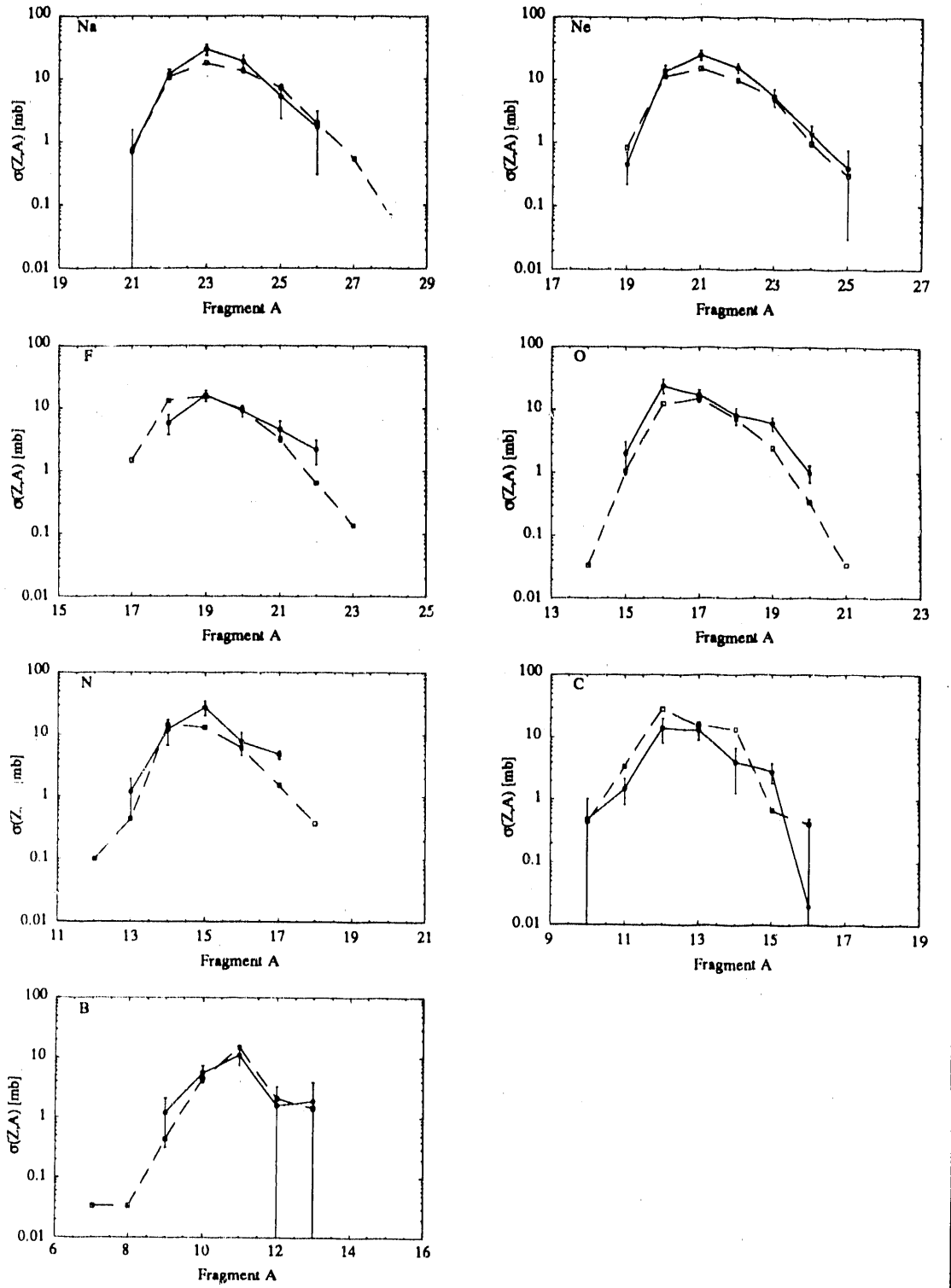

Figure 4-14 g-m
Isotopic production cross sections for 1.65·A GeV ^{40}Ar + KCl, both measured (Solid lines), and calculated by FRAGMNT and GEMINI (Dashed lines).

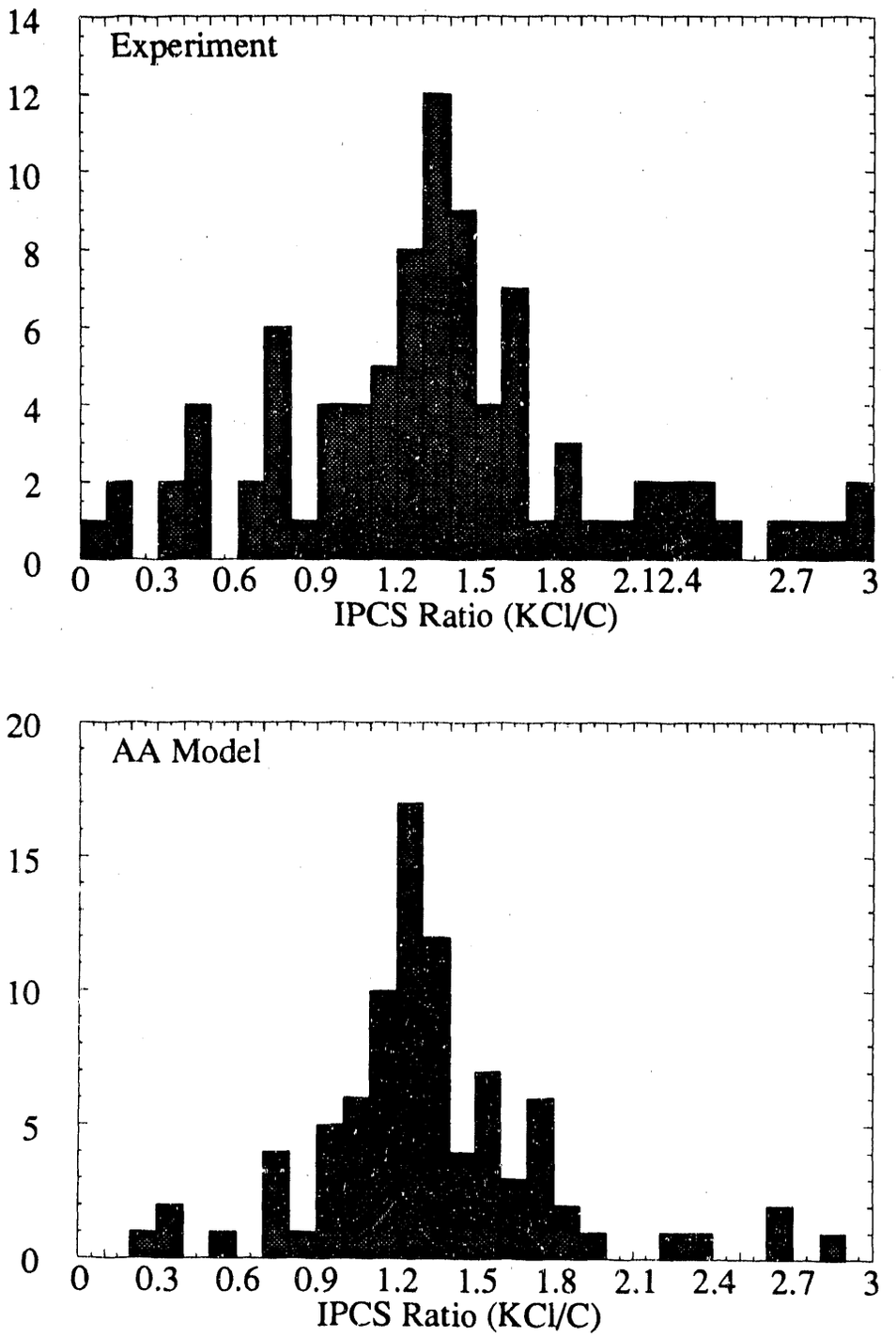

Figure 4-15
Ratio of the IPCSs (KCl target to C target) for each isotope measured (a--Experiment) or calculated (b--GEMINI AA code) for both targets. Ratios above 3.0 are not shown. This excludes 1 point (^{34}Si) for experiment and 5 points for theory.

In fragmentation experiments with relativistic heavy ions, it has been observed that the cross section for producing an isotope (f) from fragmentation of a projectile (p) by target (t) can be parameterized as the product of two factors.:

$$\sigma_{pf}^{t} = \gamma_t \cdot \gamma_{pf} \qquad \textbf{Equ. 4.2.1}$$

where the the first factor (γ_t) depends only on the target used, and the second factor (γ_{pf}) depends only on the projectile used and the fragment detected[79We,83Ol]. This dependence of the IPCS is called Factorization.

The target dependence of the IPCSs is shown in Figure 4-15. If we divide the IPCS for a particular isotope measured with the KCl target by the IPCS for the same isotopes measured with the C target, the concept of Factorization predicts a constant ratio for all isotopes. Figure 4-15 shows the distributions of the ratio of IPCSs for the two targets from experiment (mean of 1.355 and standard deviation of 0.475) and from the GEMINI Abrasion-Ablation calculation (mean of 1.366 and standard deviation of 0.629). The ratio of total interaction cross section for the two targets is:

$$\frac{(40^{1/3} + 37.28^{1/3})^2}{(40^{1/3} + 12^{1/3})^2} = 1.402 \qquad \textbf{Equ. 4.2.2}$$

which is comparable to the observed and theoretical mean ratios (NB. A non-negative value of b_0 in Equation 1.3.2 increases the ratio of Equation 4.2.2.).

Comparison of the measured cross section for ^{39}Cl with the calculated cross section for production of ^{39}Cl as a pre-fragment in the abrasion stage shows that the measured cross section for production of ^{39}Cl from the C target ($\sigma_{exp}(^{39}Cl) = 79.5 \pm 19.5$ mb) is consistent with the 1 proton removal cross section in the first stage of the AA model ($\sigma_{abr}(^{39}Cl) = 69.46$ mb).

From electron scattering experiments, we know that the nucleon density for nuclei looks something like the curve in Figure 4-15. If we define a grazing collision as one in which the maximum (saturated) nucleon densities of the two nuclei never overlap, then we

might very well expect that any interaction which takes place in a grazing collision would inject negligible excitation energy into the spectator nuclei.

Recognizing that the removal of a single proton from the ^{40}Ar nucleus in a collision must take place in such a grazing collision (see Figure 1-4), the correspondence of these two numbers suggests that the process which produces a ^{39}Cl in the final state is, in fact, a one step process such as direct nucleon knock out, rather than a two step process like Abrasion Ablation. This is equivalent to saying that the spectator pre-fragment excitation energy after one-nucleon removal is too low to cause particle emission.

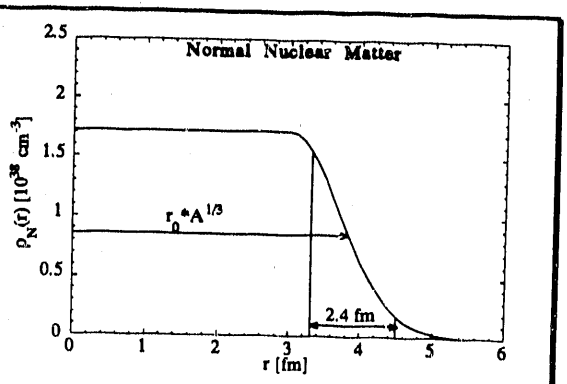

Figure 4-16
The nucleon density of normal nuclei reaches a maximum of $\rho_{max} \approx 1.72 \times 10^{38}$ cm^{-3}, and falls off over a radial distance of $t \approx 2.4$ fm.

The only measured data point which the AA model has no hope of predicting is the ^{40}Cl cross section (since the production of ^{40}Cl can not be explained by the simple removal of nucleons from the ^{40}Ar nucleus).

The production of ^{40}Cl arises from the conversion of a single proton in the ^{40}Ar nucleus to a neutron in a charge-exchange reaction; $^{40}Ar(^{12}C,^{12}N)^{40}Cl$. Charge exchange can explained at lower energies by the exchange of a virtual charged pion between two nuclei. However, the cross section for massless charge exchange at 1.65 GeV is too low to account for the observed ^{40}Cl cross section(88Li).

Another description of charge exchange at these energies has been proposed by P.Lindstrom to explain charge exchange channels seen in a fragmentation experiment with 2.1·A GeV ^{12}C(88Li). The model is this: In a grazing collision between the ^{40}Ar and ^{12}C nuclei, a Δ resonance is excited and knocked out of the ^{40}Ar nucleus. The Δ decays with a half-life on the order of 3 fm, producing a nucleon and pion which are emitted isotropically in the CM frame. Because of the mass difference between the two resultant particles, the

pion carries away the bulk of the kinetic energy from the decay. Hence, there is a reasonable probability that one of the spectator nuclei can recapture the nucleon and still remain stable.

4.3. Momentum Distributions

All three components of momentum are measured for projectile fragments detected in the drift chamber and both walls of the VMD. The three components are p_x (transverse momentum in the bending plane of the HISS dipole), p_y (transverse momentum in the vertical direction), and p_z (longitudinal momentum). The momentum distributions observed (after background subtraction) are Gaussian (see Figure 3-6) with widths that depend on the mass number of the projectile fragment.

The Gaussian fitting of the momentum distributions depends heavily on the statistics of the distribution. Therefore, we do not consider distributions of isotopes with cross sections below 5 mb (47 isotopes for the C target, 51 isotopes for the KCl target). The longitudinal momentum distributions for these isotopes have fitted means in the projectile frame.indicating a momentum loss of $\Delta p_z = -26.1 \pm 3.7$ MeV/c/A for the C target and $\Delta p_z = -24.2 \pm 5.1$ MeV/c/A for the KCl target (Figure 4-18). This is consistent with the magnitude of the momentum downshifts seen by Greiner et al[75Gr] for ^{12}C and ^{16}O fragmentation.

Following the example of Viyogi et al, we plot the value of σ_0 (for isotopes for which σ_0 can be fitted within 10%) as a function of A_f for both targets, and all three momentum components in Figures 4-19 and 4-20. Also included in each plot is the best straight line fit and the $\pm$ 95% confidence levels for the fit. The fit intercept and slope parameters are listed in Table V.

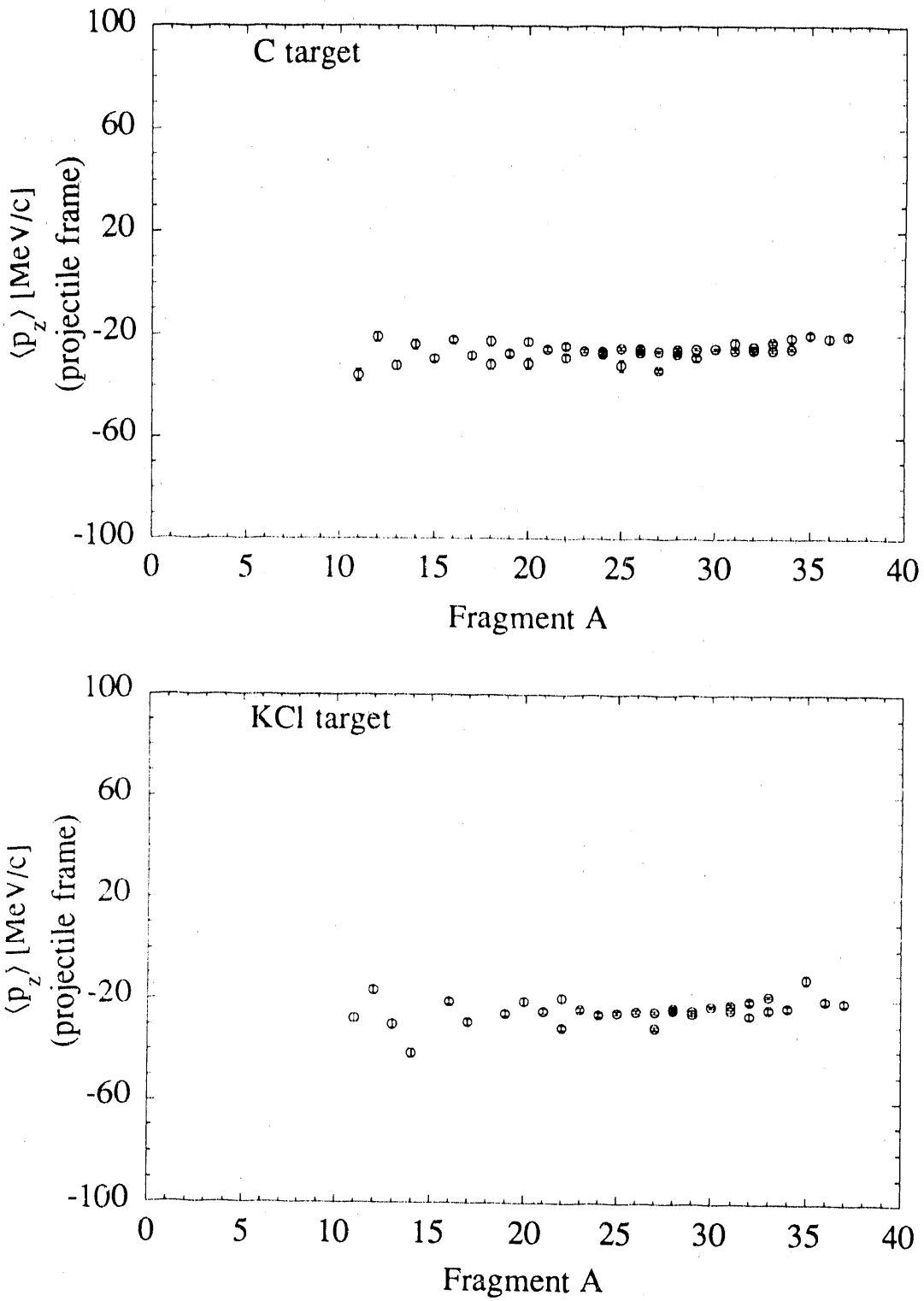

Figure 4-18
Mean of Gaussian longitudinal momentum distributions vs A_f showing a loss of momentum in the beam frame.

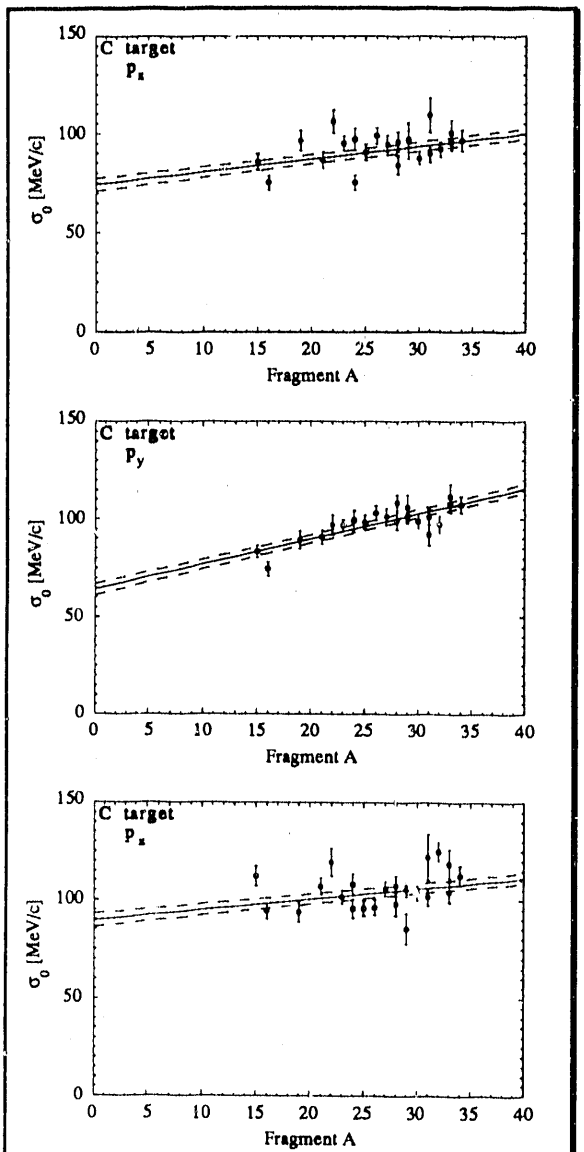

Figure 4-19
Reduced momentum widths plotted vs A_f for the C target.

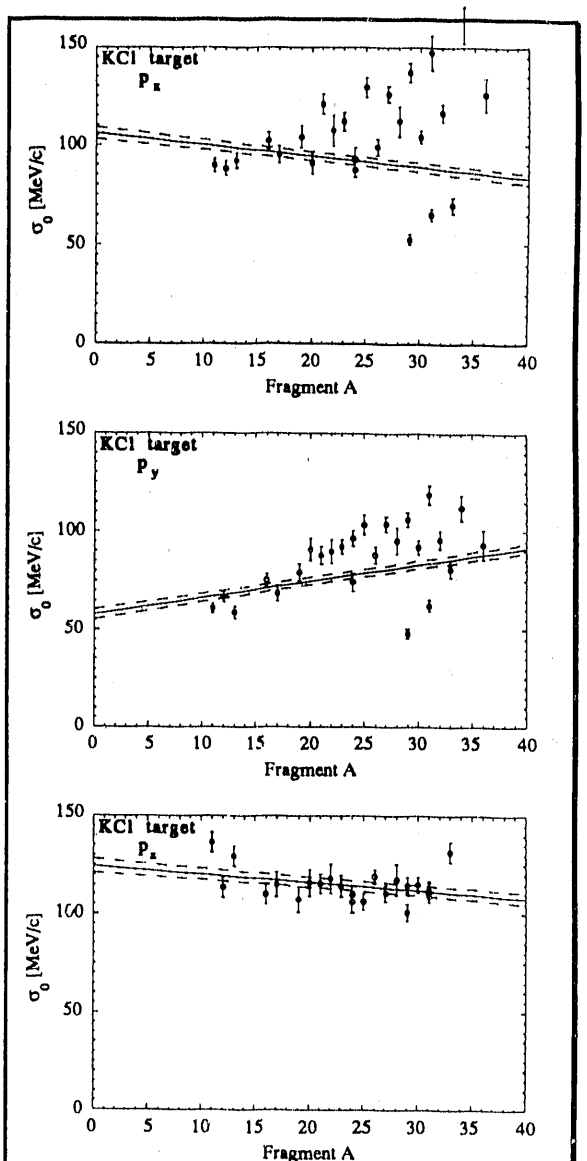

Figure 4-20
Reduced momentum widths plotted vs A_f for the KCl target.

The longitudinal components of momentum (p_z) show no obvious correlation with the mass number of the fragments (although the fitted slopes are not equal to 0 within uncertainty), and the values are consistent with the model of Goldhaber ($p_F = 251 \pm 5$ MeV/c$^{(71Mo)}$). However, the transverse component of momentum out of the bending plane

of the magnet (p_y) shows a clear trend for the C target, and a similar trend for the KCl target. The fit for the KCl target is altered by the appearance of two points (^{31}Si and ^{29}Al) with anomalously small values of σ_0. If these two points are eliminated, the best fit line is $y = 40.2 + 2.03 \cdot x$ (see Figure 4-21). The transverse momentum in the $\hat{x}$ direction does not show the same dependence of σ_0 on A_f, although the two components should physically be the same. However, the p_x data from the KCl target shows enough scatter to wash the trend seen for p_y. The p_x data for the C target does not exhibit the same amount of scatter as the data for the KCl target, however, it should be noted that experimentally, the p_x and p_z measurements are coupled since they are both determined by the x and θ_x measurements from the drift chamber and the x_{us} measurement upstream. This fact suggests that measurements of p_x and p_z will contain more systematic errors than p_y.

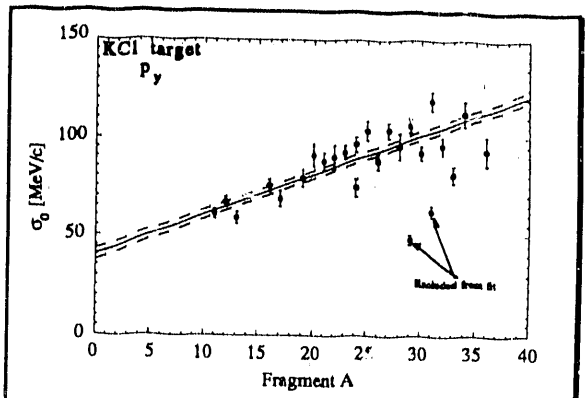

Figure 4-21
Reduced p_y widths for KCl target and fit excluding two points.

In Figures 5-22 and 5-23 we show the same plots of σ_0 vs A_f but with the values of σ_0 predicted by Goldhaber, Lepore and Riddell, Murphy, and Murphy's calculation plus Bertsch's Pauli suppression. The magnitude of σ_0 for the longitudinal direction agrees well with the value predicted by Goldhaber (σ_0 = 112.3 MeV/c from e$^-$ scattering for ^{40}Ca). The value of σ_0 predicted by the theory of Lepore and Riddell is too low to explain the longitudinal momentum widths. The curve calculated from Murphy's phase-space constraint argument is also too low, and does not reproduce the apparent shape of the σ_0 vs. A_f curve for p_z.

Although the magnitude of Murphy's curve is far too small for the p_y widths, the linear dependence of σ_0 on A_f for p_y is similar in shape to Murphy's calculation. The best fit line to Murphy's curve for $\leq A_f \leq 35$ has a slope of 0.85 MeV/c/A, the slope for

$24 \leq A_f \leq 35$ is 2.1 MeV/c/A. This compares favorably with the slopes for $\sigma_0(p_y)$ (1.29 MeV/c/A and 2.03 MeV/c/A). Although the calculation from Murphy's paper was expressly for the longitudinal component of momentum, Murphy postulated that the transverse momentum should exhibit a stronger effect of momentum anti-correlations due to (x, y) spatial correlation of the abrasion process.

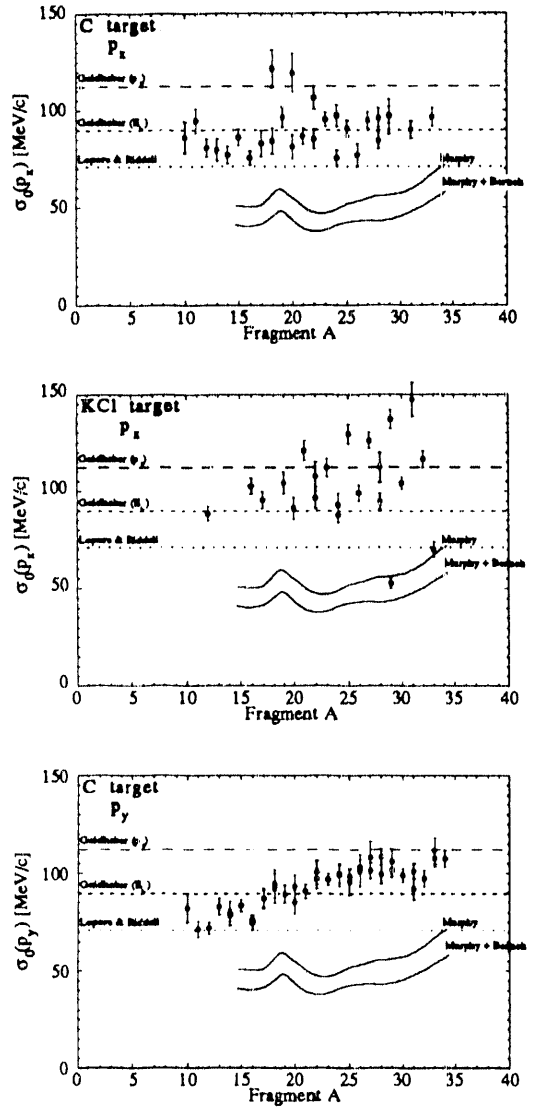

Figure 4-22
Comparison of theory and experiment (C target) for A_f dependence of σ_0.

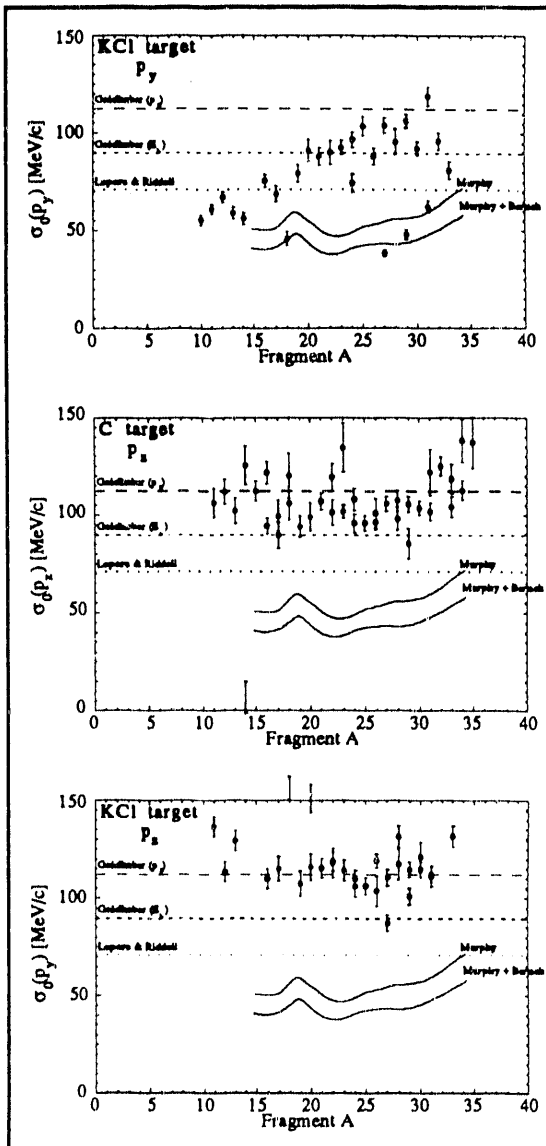

Figure 4-23
Comparison of theory and experiment (KCl target) for A_f dependence of σ_0.

A similar effect was seen by Brady et al (including the present author) for 1.65·A GeV ^{139}La + C(^{88}Br). In that data set the MUltiple Sampling Ionization Chamber (MUSIC) was used to measure the charge and vertical angle of projectile fragments. Making the assumption that the pre-fragment A/Z ratio was the same as that of the initial projectile, the average σ_0 for the data was much larger than expected from Fermi momentum (σ_0(exp) = 169 MeV/c; $\sigma_0(p_F)$ = 112 MeV/c). It was also observed that the value of σ_0 was linearly dependent on the mass of the projectile fragment with a slope of 0.63 MeV/c/A for all elements measured, or 1.1 MeV/c/A if the Z_f = 56 point is eliminated (see Figure 4-24). Although the A/Z ratio of the final fragments for a projectile as heavy as ^{139}La is not the same of that of the beam(^{89}Bi,^{89}Mü), the Goldhaber view of sampling the Fermi momentum distribution dictates the choice of the A/Z ratio of the abrasion pre-fragment, rather than the evaporated final fragment for calculation of σ_0 (see Figure 4-12).

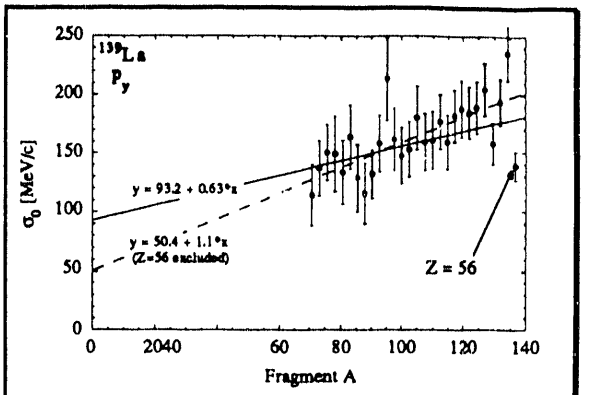

Figure 4-24
Brady et al
Linear dependence of transverse momentum σ_0 for 139La + C at 1.2·A GeV.

Brady et al invoked two effects to address this effect. The first effect was Coulomb repulsion of the projectile fragment by the target. In our experiment this is a very small effect because of the low charges of both the target and projectile. Figure 4-25 shows the modification of σ_0 due to Coulomb repulsion. The three curves are 1) Goldhaber's constant σ_0 = 112.3 MeV/c, 2) Goldhaber's constant σ_0 and Coulomb bounce off assuming that the bounce off depends on

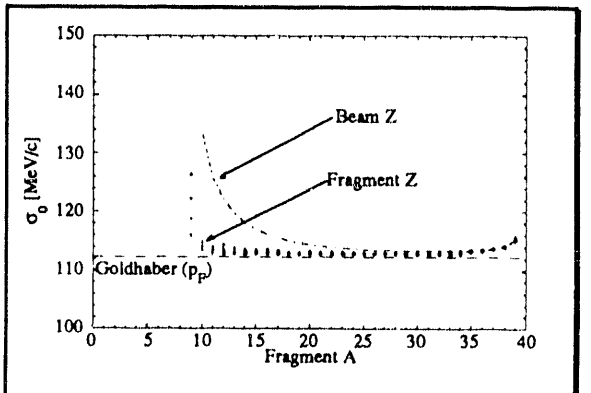

Figure 4-25
Modification to Goldhaber's σ_0 due to Coulomb bounce off.

the beam charge, and 3) Goldhaber's constant σ_0 and Coulomb bounce off assuming that the bounce off depends on the fragment charge. The effect is negligible until the impact parameter is ≈ 0.

The second process mentioned in Brady's paper concerns the scattering of energetic nucleons from the hot participant matter into the cold spectator matter. Brady et al points out that the Final State Interaction of Oliveira et al will deposit momentum as well as excitation energy into the spectator pre-fragments. If the size of the spectator is on the order of the mean free path of the participant nucleons, one might expect that larger spectators would absorb more momentum than smaller spectators (ie. The energetic nucleons are more likely to pass through a small spectator without scattering.). It was calculated that only three or four nucleons are required to be absorbed to account for the observed effect. Unfortunately, this theory does not appear satisfactory to explain the current data. The effect of this Final State Interaction momentum transfer is to widen the transverse momentum distributions relative to the longitudinal. However, we observe the suppression of the transverse distributions relative to the longitudinal. It would be interesting to measure the longitudinal momentum distribution of ^{139}La to determine if the effect measured is indeed a widening as was assumed.

Although there is technical reasons to trust the p_y momentum measurements more than the p_x, it would be reassuring to measure consistent widths in both transverse directions in the same experiment. We feel that it is important to investigate this apparent difference between the longitudinal and transverse momentum widths. Although theories exist that suggest a similar dependence of the reduced momentum width on fragment mass, or that predict a magnitude consistent with the average value observed, there is no theory extant that predicts both the magnitude and A_f dependence of σ_0 seen for the transverse and longitudinal momentum distributions.

5. Conclusion

In conclusion, we have measured inclusive isotopic and elemental production cross sections, and longitudinal and transverse momentum distributions of projectile fragments with charge $5 \leq Z_f \leq 17$ from the fragmentation of 1.65·A GeV ^{40}Ar on targets of C and KCl.

We find that the isotopic production cross sections for projectile fragments ($Z_f \leq 15$) are well described by an Abrasion-Ablation calculation which takes into account the zero point vibrations of the Giant Dipole Resonance and injects an additional FSI excitation energy into the pre-fragment. The IPCSs for elements between $8 \leq Z_f \leq 16$ produced by fragmentation on a C target show behavior similar to the IPCSs from reactions at 213·A MeV; consistent with the assumption of Limiting Fragmentation. The new data shows that the IPCSs scale as the geometric cross section of the system (see Equation 1.3.2). This result tends to support the earlier assertions of Factorization for RHI reactions.

Previously unmeasured production cross sections for $^{40}Ar + X \rightarrow {}^{39}Cl + Y$ (where X is either C or KCl) indicate that one nucleon removal is accomplished in grazing collisions with little or no interpenetration of nucleons from one collision partner into the other. Charge-changing cross sections were also measured in the same experiment ($^{40}Ar + X \rightarrow {}^{40}Cl + Y$) and have production cross sections on the order of 10 mb.

The widths of the longitudinal momentum distributions for the fragments obeyed the same dependence on A_f has had been seen in the distributions for lighter nuclei (1.05·A GeV ^{12}C, 2.1·A GeV ^{12}C, and 2.1·A GeV ^{16}O) and for lower energy (213·A MeV ^{40}Ar). This dependence has been interpreted as reflecting either the Fermi momentum of the original nucleus (in the case of a fast break up) or the temperature of an excited pre-fragment (in the case of slow thermal equilibration and decay). Such interpretation gives a Fermi momentum of $p_F = 244 \pm 11.5$ MeV/c or a source temperature of $kT = 13.1 \pm 0.62$ MeV.

However, the transverse momentum distributions for fragments $Z_f = (10, 35)$ exhibit widths which are narrower than the widths expected from the model used to describe the longitudinal distributions. In fact, if the transverse momentum widths are used to calculate a Fermi Momentum of the initial projectile (or Temperature of the pre-fragment), the value of p_f has a linear dependence on the mass of the final fragment. This behavior is similar to that predicted by consideration of phase space constraints on the final fragment nuclei (with or without additional Pauli suppression)[84Mu] and reminiscent of results of a previous measurement of transverse momentum distributions[88Br]. We conclude that the current theories do not adequately explain the observed phenomenon, and that further investigation of the effect is warranted.

Future Work

The other beams for which data were taken in the experiment will be analyzed to determine if the transverse momentum distribution widths show a dependence on projectile mass. This data set combined with data from the literature will give us transverse momentum widths for ^{40}Ar, ^{56}Fe, ^{91}Nb, and ^{139}La , and longitudinal momentum widths for ^{12}C, ^{16}O, ^{40}Ar, ^{56}Fe, and ^{91}Nb. This should provide enough points to quantify any mass dependence of the momentum distributions.

We are convinced that the internal parameters of the GEMINI evaporation code can be further optimized for our calculations. We used a constant value of a_0 for our calculations. We plan to examine the effect of varying a_0 as a function of A_f, and/or E^*. This should provide a useful tool for the calculation of isotopic production cross sections for projectile fragmentation.

6. Appendices

6.1. References

Ref.	Author	Publication	Year
48BP	H.L.Bradt & B.Peters	Phys.Rev. 74:1828	(1948)
48Fr1	P.Freier et al	Phys.Rev. 74:213	(1948)
48Fr2	P.Freier et al	Phys.Rev. 74:1818	(1948)
49BP	H.L.Bradt & B.Peters	Phys.Rev. 75:1779	(1949)
50BP1	H.L.Bradt & B.Peters	Phys.Rev. 77:54	(1950)
50BP2	H.L.Bradt & B.Peters	Phys.Rev. 80:54	(1950)
52Ka	M.F.Kaplon et al	Phys.Rev. 85:295	(1952)
54Ei	Y.Eisenberg	Phys.Rev. 96:1378	(1954)
55Ch	O.Chamberlain et al	Phys.Rev. 100:947	(1955)
58Je	J.V.Jelly	*Cerenkov Radiation and its applications*, p. 138	(1958)
69Le	C.Lechanoine et al	Nucl.Inst.Meth. 69:122	(1969)
71Lo	E.J.Lofgren	Science 174:1128	(1971)
71Mo	E.J.Moniz et al	Phys.Rev.Lett. 26:445	(1971)
71Wh	M.G.White et al	Science 174:1121	(1971)
72He	H.H.Heckman et al	Phys.Rev.Lett. 28:926	(1972)
73FH	H.Feshback & K.Huang	Phys.Lett. 47B:300	(1973)
73ST1	R.Silberberg & C.H.Tsao	Ap.J.Suppl. 25:315	(1973)
73ST2	R.Silberberg & C.H.Tsao	Ap.J.Suppl. 25:335	(1973)
74Go	A.S.Goldhaber	Phys.Lett. 53B:306	(1974)
74LR	J.V.Lepore & R.J.Riddell Jr.	LBL-3086	(1974)
75Gr	D.E.Greiner et al	Phys.Rev.Lett. 35:152	(1975)
75LT	V.K.Lukyanov & A.I.Titov	Phys.Lett. 57B:10	(1975)
77Ra	J.O.Rasmussen et al	LBL-6580	(1977)
77Sa	F.Sauli	*Principles of Operation of Multiwire Proportional and Drift Chambers*	(1977)
77SY	J.Seguinot & T.Ypsilantis	Nucl.Inst.Meth. 142:377	(1977)
78Mo	D.J.Morrissey et al	Z. Phys. A289:123	(1978)
78Ol	L.F.Oliveira	LBL-8561;Ph.D. Dissertation, UC Berkeley	(1978)
78We	G.D.Westfall et al	LBL-7162	(1978)
79Mo	D.J.Morrissey et al	Phys.Rev.Lett. 43:1139	(1979)
79Ol	L.F.Oliveira et al	Phys.Rev. C19:826	(1979)
79Sy	T.J.M.Symons et al	Phys. Rev. Lett. 42:40	(1979)
79Vi	Y.P.Viyogi et al	Phys. Rev. Lett. 42:33	(1979)
79We	G.D.Westfall et al	Phys.Rev. C19:1309	(1979)
81Ol	D.L.Olson et al	Phys. Rev. C24:1529	(1981)
82Ol	D.L.Olson	Ph.D. Dissertation, UC Davis	(1982?)
83Cr	H.J.Crawford	LBL-16171	(1983)
83Ol	D.L.Olson et al	LBL-15837	(1983)
84Me	M.T.Mercier et al	Phys.Rev.Lett. 52:898	(1984)

85Du	J.P.Dufour et al	Nucl. Inst. Meth. A241:491	(1985)
85Fu	N.Fujiwara et al	Nucl.Inst.Meth. 240:275	(1985)
85Ol	D.L.Olson et al	LBL-18259	(1985)
86Ol	D.L.Olson	HISS Internal Document	(1986)
87Ko	T.Kobayashi et al	Nucl.Inst.Meth. A254:281	(1987)
88BD	G.F.Bertsch & S.Das Gupta	Physics Reports 160:189	(1988)
88Br	F.P.Brady et al	Phys.Rev.Lett. 60:1699	(1988)
88Ki	J.M.Kidd et al	Phys.Rev. C37:2613	(1988)
88Ko	T.Kobayashi et al	Phys. Rev. Lett. 60:2599	(1988)
88Li	P.J.Lindstrom et al	LBL-24580:397	(1988)
88UM	F.Uchiyama & N. Masuda	Phys. Rev. C38:2670	(1988)
89Ch	R.J.Charity et al	LBL-22448	(1989)
89En	J.Engelage et al	Nucl.Inst.Meth. A277:431	(1989)
89Ko	T.Kobayashi et al	Submitted to Nucl. Inst. Meth.???	(1989)
89Mo	D.J.Morrissey	Private Communication	(1989)
89Ol	D.L.Olson	Private Communication	(1989)
89OT	D.L.Olson & C.E.Tull	Private Communication	(1989)
89Pe	G.Peaslee	Private Communication	(1989)
89Sh	A.Shor et al	LBL-27477	(1989)
90Ch	W.B.Christie	Ph.D. Thesis, UC Davis	(1990)

6.2. Tables

Background Mass			
Detector	Composition	Detector Thickness (mg/cm^2)	Cumulative Thickness (g/cm^2)
S1	20 mil Scintillator (CH) 2 × 16 μm Al foils	52 8.6	0.06
US Vacuum Windows	4 × 5 mil Kapton	7.3	0.07
US Air Gaps	≈ 20 cm Air	≈ 24	0.09
USWCs	4 × 2 mil Mylar ($C_5H_4O_2$)	28	0.12
S2	20 mil Scintillator (CH) 2 × 16 μm Al foils	52 8.6	0.18
HISS Vacuum Window	80 mg/cm^2 Mylar ($C_5H_4O_2$) & Kevlar	80	0.26
DS Air Gap	≈ 2 m Air	≈ 240	0.50
pDC	1.1 m P10 (90% Ar + 10% CH_4) 2 × 50 μm Mylar	180 14	0.69
DSWCs	4 × 2 mil Mylar ($C_5H_4O_2$)	28	0.72
S3	3 mm Scintillator (CH)	310	1.03
VMD Q	0.5 - 1.0 cm SiO	1100 - 2200	2.13 - 3.23
VMD G	0.5 - 1.0 cm SiO	1100 - 2200	3.23 - 5.46

Table II: Contributions to the background mass of the detector system.

^{40}Ar Fragmentation Isotopic Production Cross Sections							
	Experiment			Theory			
	1.65·A GeV C	1.65·A GeV KCl	213·A MeV (Viyogi) C	ALICE (Oliviera) C	GEMINI C	GEMINI KCl	GEMINI $\frac{\gamma_t(^{39}K)}{\gamma_t(^{12}C)}$
^{7}B						0.031	
^{8}B	0.210 ± 0.255				0.038	0.031	
^{9}B	0.495 ± 0.270	1.20 ± 0.880			0.364	0.398	1.17
^{10}B	4.05 ± 1.485	5.60 ± 1.80			2.87	3.98	1.48
^{11}B	7.80 ± 2.70	11.0 ± 3.70			10.2	13.6	1.42
^{12}B	2.25 ± 0.855	1.60 ± 1.70			1.65	1.90	1.23
^{13}B	1.455 ± 0.555	1.90 ± 2.00			1.02	1.32	1.38
^{14}B					0.077		
^{10}C	0.180 ± 0.240	0.480 ± 0.550			0.229	0.254	1.11
^{11}C	1.215 ± 0.555	1.50 ± 0.670			1.226	1.99	1.63
^{12}C	10.2 ± 3.30	14.0 ± 6.00			12.2	16.3	1.33
^{13}C	10.0 ± 3.00	13.0 ± 4.20			7.01	8.88	1.27
^{14}C	4.35 ± 1.50	4.00 ± 2.70			6.42	7.76	1.21
^{15}C	1.17 ± 0.675	2.80 ± 0.980			0.264	0.391	1.48
^{16}C	0.375 ± 0.165	0.020 ± 0.480			0.206	0.235	1.14
^{12}N					0.052	0.149	
^{13}N	0.750 ± 0.480	1.20 ± 0.760			0.364	0.648	1.58
^{14}N	8.70 ± 2.70	12.0 ± 5.30			13.8	21.1	1.37
^{15}N	18.0 ± 5.10	27.0 ± 7.00			13.2	19.1	1.28
^{16}N	4.65 ± 1.30	7.70 ± 3.10			5.22	8.87	1.51

Table III: Page 1 (cont')

	1.65·A GeV C	1.65·A GeV KCl	213·A MeV (Viyogi) C	ALICE (Oliviera) C	GEMINI C	GEMINI KCl	GEMINI $\frac{\gamma_t(^{39}K)}{\gamma_t(^{12}C)}$
^{17}N	2.25 ± 0.570	4.80 ± 0.730			1.95	2.24	1.02
^{18}N	0.600 ± 0.240				0.338	0.548	
^{13}O			0.370 ± 0.190				
^{14}O	0.086 ± 0.111		1.40 ± 0.600		0.020	0.051	
^{15}O	1.23 ± 0.615	2.00 ± 1.10	10.6 ± 3.70	0.600	0.826	1.58	1.26
^{16}O	14.2 ± 3.45	24.0 ± 6.10	36.2 ± 9.00	7.10	8.47	18.8	1.45
^{17}O	9.75 ± 2.40	17.0 ± 3.80	20.0 ± 7.00	14.3	11.3	22.7	1.32
^{18}O	6.75 ± 1.44	8.30 ± 2.50	11.9 ± 4.50	5.40	5.96	11.0	1.21
^{19}O	3.60 ± 0.645	6.10 ± 1.40	1.90 ± 0.860	1.10	2.52	3.73	0.97
^{20}O	0.330 ± 0.088	0.990 ± 0.300	0.440 ± 0.250	0.140	0.590	0.511	0.57
^{21}O					0.079	0.0511	
^{17}F	0.345 ± 0.315		2.40 ± 1.20	1.10	0.591	1.28	
^{18}F	5.40 ± 1.32	5.80 ± 2.00	11.4 ± 4.60	11.2	8.70	11.5	1.28
^{19}F	11.7 ± 2.25	16.0 ± 3.30	23.9 ± 6.00	19.9	11.5	13.2	1.10
^{20}F	7.20 ± 1.95	9.10 ± 1.90	17.8 ± 6.20	8.40	6.19	8.26	1.29
^{21}F	4.35 ± 0.810	4.60 ± 1.70	7.80 ± 3.10	1.90	1.97	2.76	1.35
^{22}F	0.765 ± 0.285	2.20 ± 0.930	1.34 ± 0.600	0.300	0.608	0.552	0.88
^{23}F			0.380 ± 0.200	0.200	0.148	0.116	
^{18}Ne			0.090 ± 0.060	0.040	0.024		
^{19}Ne	0.705 ± 0.360	0.460 ± 0.240	1.50 ± 0.700	1.40	1.03	1.20	1.02
^{20}Ne	8.55 ± 1.80	14.0 ± 3.30	5.40 ± 2.20	12.7	11.5	16.2	1.22
^{21}Ne	16.5 ± 2.55	25.0 ± 4.50	24.0 ± 7.20	21.1	16.5	21.8	1.15

Table III: Page 2 (cont')

	1.65·A GeV C	1.65·A GeV KCl	213·A MeV (Viyogi) C	ALICE (Oliviera) C	GEMINI C	GEMINI KCl	GEMINI $\frac{\gamma_t(^{39}K)}{\gamma_t(^{12}C)}$
^{22}Ne	12.3 ± 2.25	16.0 ± 2.70	33.9 ± 8.50	12.1	10.7	14.4	1.17
^{23}Ne	4.80 ± 0.540	5.50 ± 1.70	21.7 ± 6.50	3.50	3.79	7.22	1.65
^{24}Ne	1.80 ± 0.450	1.40 ± 0.510	4.90 ± 2.00	0.50	1.174	1.40	1.03
^{25}Ne	0.210 ± 0.146	0.40 ± 0.370	0.520 ± 0.290	0.040	0.196	0.433	1.92
^{20}Na			0.760 ± 0.420	0.040	0.028		
^{21}Na	0.255 ± 0.123	0.760 ± 0.80	2.20 ± 1.00	1.20	0.668	0.927	1.49
^{22}Na	8.25 ± 1.65	12.0 ± 2.20	10.3 ± 4.00	11.6	12.5	14.3	1.23
^{23}Na	22.5 ± 3.15	30.0 ± 5.90	20.3 ± 6.00	23.8	19.2	23.5	1.32
^{24}Na	12.6 ± 2.10	19.0 ± 4.30	38.9 ± 9.70	15.9	13.4	17.3	1.39
^{25}Na	7.95 ± 1.05	5.20 ± 2.90	14.8 ± 5.90	5.00	6.07	9.31	1.65
^{26}Na	2.40 ± 0.510	1.70 ± 1.40	2.30 ± 1.00	1.00	1.98	2.56	1.39
^{27}Na	0.360 ± 0.135		0.270 ± 0.150	0.10	0.445	0.706	
^{28}Na						0.088	
^{29}Na					0.028		
^{22}Mg			0.20 ± 0.120	0.040			
^{23}Mg	0.960 ± 0.315	0.40 ± 0.180	3.80 ± 1.70	1.00	1.01	0.663	0.79
^{24}Mg	14.2 ± 1.80	21.0 ± 3.50	23.0 ± 8.00	9.50	13.4	16.3	1.48
^{25}Mg	22.5 ± 3.45	26.0 ± 3.90	36.0 ± 9.00	23.6	24.8	29.3	1.43
^{26}Mg	24.0 ± 2.85	29.0 ± 3.20	33.0 ± 8.30	21.4	20.8	24.8	1.45
^{27}Mg	6.75 ± 1.02	10.0 ± 4.70	11.5 ± 4.00	7.70	8.22	12.1	1.78
^{28}Mg	2.10 ± 0.495	0.420 ± 0.80	4.00 ± 1.40	1.60	2.72	3.36	1.50
^{29}Mg	0.660 ± 0.210	0.680 ± 0.340	0.067 ± 0.340	0.170	0.435	1.02	2.84

Table III: Page 3 (cont')

	1.65·A GeV C	1.65·A GeV KCl	213·A MeV (Viyogi) C	ALICE (Oliviera) C	GEMINI C	GEMINI KCl	GEMINI $\frac{\gamma_t(^{39}K)}{\gamma_t(^{12}C)}$
^{30}Mg	0.165 ± 0.126	0.280 ± 0.280	0.110 ± 0.070	0.030	0.072	0.204	3.41
^{24}Al			0.034 ± 0.020	0.030	0.033		
^{25}Al	0.315 ± 0.165	0.860 ± 0.440	0.230 ± 0.120	0.660	0.685	0.747	1.30
^{26}Al	7.20 ± 1.28	8.00 ± 1.30	1.70 ± 0.80	7.70	11.2	13.1	1.40
^{27}Al	25.5 ± 2.85	37.0 ± 4.30	15.8 ± 5.50	21.3	22.2	25.7	1.38
^{28}Al	19.5 ± 2.40	18.0 ± 4.70	42.6 ± 10.7	25.9	18.5	26.6	1.72
^{29}Al	10.4 ± 2.25	22.0 ± 5.30	15.3 ± 9.00	9.60	10.6	15.5	1.74
^{30}Al	3.00 ± 0.405	1.50 ± 0.490	4.10 ± 1.90	3.20	2.64	5.46	2.47
^{31}Al	0.705 ± 0.210	0.580 ± 0.320	1.20 ± 0.50	0.510	0.685	0.794	1.38
^{32}Al	0.129 ± 0.111		0.080 ± 0.040	0.030	0.131	0.047	
^{26}Si			0.250 ± 0.130	0.020			
^{27}Si	0.690 ± 0.285	1.40 ± 0.60	2.50 ± 1.10	0.40	0.570	0.730	1.84
^{28}Si	13.0 ± 1.95	15.0 ± 2.80	22.4 ± 6.70	5.40	12.7	13.1	1.48
^{29}Si	25.5 ± 3.00	38.0 ± 5.20	42.5 ± 10.6	21.2	29.0	38.2	1.89
^{30}Si	37.5 ± 3.15	43.0 ± 5.20	49.5 ± 12.4	26.8	25.7	35.1	1.96
^{31}Si	11.0 ± 1.80	14.0 ± 9.00	16.8 ± 5.90	15.1	16.8	17.2	1.48
^{32}Si	3.00 ± 0.240	1.50 ± 1.80	8.20 ± 3.20	4.30	6.13	7.87	1.84
^{33}Si	1.32 ± 0.240	0.540 ± 0.890	1.30 ± 0.60	0.730	1.01	1.09	1.56
^{34}Si	0.01 ± 0.07	0.160 ± 0.097	0.320 ± 0.160	0.110	0.131	0.261	2.84
^{28}P					0.038		
^{29}P	0.315 ± 0.195	0.420 ± 0.330	10.4 ± 3.50	0.280	0.876	0.142	0.30
^{30}P	3.90 ± 0.630	7.40 ± 1.70	27.0 ± 8.10	3.70	9.14	8.26	1.66

Table III: Page 4 (cont')

	1.65·A GeV C	1.65·A GeV KCl	213·A MeV (Viyogi) C	ALICE (Oliviera) C	GEMINI C	GEMINI KCl	GEMINI $\frac{\gamma_t(^{39}K)}{\gamma_t(^{12}C)}$
^{31}P	21.0 ± 2.10	21.0 ± 3.80	41.5 ± 10.4	17.0	25.7	21.4	1.52
^{32}P	27.0 ± 2.70	25.0 ± 3.00	33.0 ± 9.00	40.3	25.9	26.1	1.85
^{33}P	18.0 ± 1.80	22.0 ± 5.70	8.70 ± 3.50	26.1	11.0	18.2	3.02
^{34}P	5.85 ± 0.825	2.10 ± 1.50	1.50 ± 0.70	7.80	5.79	6.13	1.94
^{35}P	2.10 ± 0.330	2.80 ± 0.930		0.820	0.305	0.744	4.48
^{36}P	0.615 ± 0.195	0.20 ± 0.071			0.038		
^{31}S	0.540 ± 0.420	1.90 ± 1.50	0.980 ± 0.60	0.130	1.13	0.468	
^{32}S	10.6 ± 3.00	20.0 ± 6.30	9.00 ± 4.50	2.10	25.8	22.0	1.76
^{33}S	31.5 ± 7.05	41.0 ± 8.50	27.5 ± 11.0	18.7	42.4	67.0	3.25
^{34}S	49.5 ± 10.8	50.0 ± 11.0	58.0 ± 17.4	35.4	30.0	73.0	5.00
^{35}S	24.0 ± 5.40	32.0 ± 8.60	27.3 ± 11.0	31.3	23.0	11.8	1.05
^{36}S	12.4 ± 3.00	29.0 ± 6.00	19.3 ± 8.70	15.7	19.4	12.6	1.34
^{37}S	11.7 ± 2.70	19.0 ± 4.10	9.80 ± 5.00	1.70		13.8	
^{38}S	4.35 ± 1.50	9.90 ± 2.70	2.10 ± 1.20	0.170	2.37	2.15	1.87
^{32}Cl					0.072		
^{33}Cl					0.216	0.642	
^{34}Cl	12.0 ± 6.45	17.0 ± 10.0			0.576	8.98	32.85
^{35}Cl	51.0 ± 19.5	38.0 ± 15.0			12.9	8.11	1.33
^{36}Cl	49.5 ± 16.5	6.80 ± 3.80			1.22	3.73	6.43
^{37}Cl	27.0 ± 8.85	42.0 ± 31.0			24.8	16.3	1.38
^{38}Cl	8.10 ± 4.05				86.3	56.1	
^{39}Cl	79.5 ± 19.5	56.0 ± 29.0			108.	71.9	1.40

Table III: Page 5 (cont')

	1.65·A GeV C	1.65·A GeV KCl	213·A MeV (Viyogi) C	ALICE (Oliviera) C	GEMINI C	GEMINI KCl	GEMINI $\frac{\gamma_t(^{39}K)}{\gamma_t(^{12}C)}$
^{40}C:	7.50 ± 4.35	5.90 ± 7.20					

Table III: Columns 2-4 are measured isotopic production cross sections for fragmentation of ^{40}Ar + C and ^{40}Ar + KCl at 1.65·A GeV (this experiment) and for ^{40}Ar + C at 213·A MeV (Reference 79Vi). Columns 5-7 are calculated isotopic production cross sections for fragmentation of ^{40}Ar + C using OVERLAID-ALICE (Oliveira) and for ^{40}Ar + ^{12}C and ^{40}Ar + ^{39}K using GEMINI. Column 8 is the target dependence of ^{40}Ar + ^{39}K relative to ^{40}Ar + ^{12}C as calculated using GEMINI.

Reduced Momentum Widths from Projectile Fragmentation					
Reference	Projectile	Beam Energy [GeV/A]	$\langle\sigma_0\rangle$ Experiment [MeV/c]	$5^{-2}\cdot p_F$ e⁻ Scattering [MeV/c]	$\sqrt{m_n \cdot E_b}$ Mass Meas. [MeV/c]
Greiner et al(75Gr)	^{12}C	1.05	77.8 ± 2.7	98.8	84.7
	^{12}C	2.1	81.4 ± 2.2	98.8	84.7
	^{16}O	2.1	82.7 ± 1.3	102.9	86.3
Viyogi et al(79Vi)	^{40}Ar	0.2	94 ± 5	112.3 ± 2.2*	89.5
Brady et al(88Br)	^{139}La	1.2	169 ± 12	112	88.5
This Experiment					
C target p_x	^{40}Ar	1.65	90.8 ± 7.9	112.3 ± 2.2*	89.5
C target p_y	^{40}Ar	1.65	97.0 ± 8.7	112.3 ± 2.2*	89.5
C target p_z	^{40}Ar	1.65	103.8 ± 8.1	112.3 ± 2.2*	89.5
KCl target p_x	^{40}Ar	1.65	92.6 ± 23.	112.3 ± 2.2*	89.5
KCl target p_y	^{40}Ar	1.65	76.5 ± 19.	112.3 ± 2.2*	89.5
KCl target p_z	^{40}Ar	1.65	114.5 ± 8.1	112.3 ± 2.2*	89.5

Table IV: List of projectile fragmentation experiments where at least one component of fragment momentum was measured. The reduced momentum widths (σ_0) are calculated from the mean value of momentum widths measured. The values of Fermi momentum (p_F) and binding energy (E_b) are used to predict expected values of σ_0 according to the formulae of Goldhaber(74Go).

Target		σ_0 [MeV/c]	$\sigma_0(A_f)$ at $A_f = 0$ [MeV/c]	$\Delta\sigma_0(A_f)/\Delta A_f$ [MeV/c/A]	χ^2 (per d.o.f.)
C	p_x	90.8 ± 7.9	74.2 ± .94	0.65 ± .036	2.86
C	p_y	97.0 ± 8.7	64.1 ± .86	1.29 ± .033	1.54
C	p_z	103.8 ± 8.1	89.6 ± 1.0	0.54 ± .038	2.91
KCl	p_x	92.6 ± 23.	106.2 ± .88	-0.58 ± .036	32.6
KCl	p_y	76.5 ± 19.	57.9 ± .77	0.84 ± .033	26.7
KCl	p_z	114.5 ± 8.1	124.5 ± 1.0	-0.42 ± .041	2.75

Table V: List of line fits for σ_0 wrt. A_f for 3 coordinates and 2 targets.

* From p_F of ^{40}Ca.

END

DATE FILMED

03 / 11 / 91